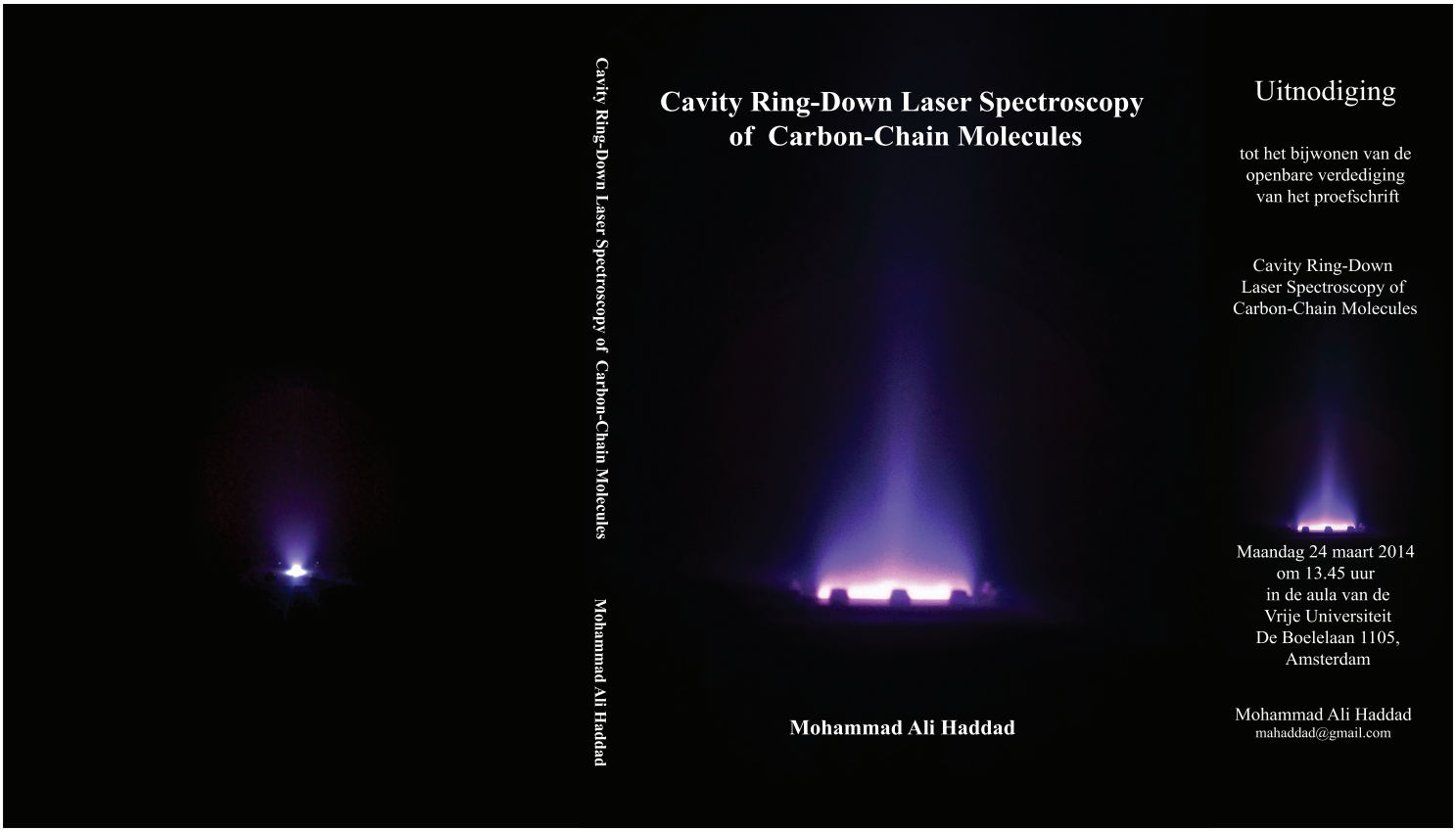

Cavity Ring-Down Laser Spectroscopy of Carbon-Chain Molecules

Mohammad Ali Haddad

Cavity Ring-Down Laser Spectroscopy of Carbon-Chain Molecules

Mohammad Ali Haddad

Uitnodiging

tot het bijwonen van de
openbare verdediging
van het proefschrift

Cavity Ring-Down
Laser Spectroscopy of
Carbon-Chain Molecules

Maandag 24 maart 2014
om 13.45 uur
in de aula van de
Vrije Universiteit
De Boelelaan 1105,
Amsterdam

Mohammad Ali Haddad
mahaddad@gmail.com

Cavity Ring-Down Laser Spectroscopy of Carbon-Chain Molecules

VRIJE UNIVERSITEIT

Cavity Ring-Down Laser Spectroscopy of Carbon-Chain Molecules

ACADEMISCH PROEFSCHRIFT

ter verkrijging van de graad Doctor aan
de Vrije Universiteit Amsterdam,
op gezag van de rector magnificus
prof. dr. F.A. van der Duyn Schouten,
in het openbaar te verdedigen
ten overstaan van de promotiecommissie
van de Faculteit der Exacte Wetenschappen
op maandag 24 maart 2014 om 13.45 uur
in de aula van de universiteit,
De Boelelaan 1105

door

Mohammad Ali Haddad

geboren te Teheran, Iran

promotoren:	prof. dr. W. M. G. Ubachs
	prof. dr. H. V. J. Linnartz
copromotor:	dr. D. Zhao

for my wife and family

توانا بود هر که دانا بود ز دانش دل پیر برنا بود

Ta'vānā Bo'vad Har'ke Dānā Bo' vad
Ze Dānesh De'le Pír Bor'nā Bo'vad

Capable is he who is wise,
Happiness from wisdom will arise.

Hakīm Abul-Qāsim Firdawsī Tūsī
(940 - 1020 C.E., Tus, Iran)

This thesis was approved by the members of the reviewing committee:

Dr. R. Engeln (Eindhoven University of Technology, Netherlands)
Prof. Dr. T. F. Giesen (University of Kassel, Germany)
Prof. Dr. L. Kaper (University of Amsterdam and Vrije Universiteit Amsterdam, Netherlands)
Prof. Dr. J. Oomens (Radboud University Nijmegen, Netherlands)
Dr. A. Petrignani, (Leiden University, Netherlands)

The work described in this thesis was carried out in the Institute for Lasers, Life and Biophotonics and the Department of Physics and Astronomy at VU University Amsterdam.
And was supported by the Ministry of Science, Research and Technology of Iran and Department of Physics and Astronomy at VU University Amsterdam.

The cover depicts a typical supersonically expanding hydrocarbon plasma generated by slit (*front-cover*) and pinhole (*back-cover*) discharge nozzles.

ISBN: 978-94-6259-090-8
Printed by: Ipskamp Drukkers.

Contents

Chapter 1: Introduction **1**
1.1 Diffuse interstellar bands 2
1.2 Thesis outline and summary 4

Chapter 2: Experimental overview **7**
2.1 Pulsed-CRD absorption technique 8
2.2 Laser system and wavelength calibration 10
2.3 Generation of (hydro)-carbon chain transient radicals . . . 11
2.4 Vacuum chamber and optical cavity 14
2.5 Data Acquisition 15

Chapter 3: Spin-orbit splitting and lifetime broadening in the $\widetilde{A}^2\Delta$ electronic state of *l*-C_5H **17**
3.1 Introduction 18
3.2 Experimental 18
3.3 Results 19
3.4 Discussion 25
3.5 Conclusion 25

Chapter 4: Structure determination of the nonlinear hydrocarbon chains $C_9H_3$and $C_{11}H_3$ by deuterium labeling **29**
4.1 Introduction 30
4.2 Experimental and theoretical methods 30
4.3 Results and analysis 32
4.3.1 Experimental spectra 32
4.3.2 Structure determination of C_9H_3 32
4.3.3 Structure determination of $C_{11}H_3$ 36
4.4 Discussion 37
4.5 Conclusion 40

Chapter 5: Rotationally resolved $\widetilde{A}^3\Sigma_u^- - \widetilde{X}^3\Sigma_g^-$ electronic transition of HC_7D and DC_7D **41**
5.1 Introduction 42
5.2 Experimental 42
5.3 Results and discussion 43
5.3.1 HC_7D 43
5.3.2 DC_7D 45
5.4 Conclusion 49

Chapter 6: Rotationally resolved spectra of the 4051 Å comet band of C_3 for all six ^{12}C and ^{13}C isotopologues **51**
6.1 Introduction 52
6.2 Experimental 53
6.3 Results and Discussion 55
6.3.1 $^{12}C_3$ 55
6.3.2 $^{13}C_3$ 61
6.3.3 ^{13}C mono- and di-substituted C_3-isotopologues . . . 65
6.4 Conclusion 70

Chapter 7: The $^2\Pi - \widetilde{X}^2\Pi$ electronic spectra of long carbon-chain $^{(13)}C_{2n}H/D$ molecules for $(n = 4 - 6)$ **73**
7.1 Introduction 74
7.2 Experimental 75
7.3 Results 75
7.3.1 C_8H, C_8D, $^{13}C_8H$, and $^{13}C_8D$ 75
7.3.2 $C_{10}H$, $C_{10}D$, $^{13}C_{10}H$ and $^{13}C_{10}D$ 79
7.3.3 $C_{12}H$, $C_{12}D$ 82
7.4 Discussion and Conclusions 85
7.5 Acknowledgments 87

Bibliography **89**

List of Publications **99**

Samenvatting **101**

Acknowledgements **103**

CHAPTER 1

Introduction

Atoms and molecules absorb specific frequencies of electromagnetic radiation according to their energy level structure that is governed by quantum mechanics. Spectroscopy is the tool to study the absorption and emission features characteristic for each individual species. The unique spectra in the ultraviolet (UV), visible (VIS) and infrared (IR) range cannot only be used to determine the atomic and molecular level structures, but also for the unambiguous identification of chemical species in various combustion environments as well as in outer space. The spectroscopic study of matter in space is an important tool for establishing the chemical composition of the highly dilute medium in between and around stars, which is known as the interstellar medium (ISM). The ISM is filled mainly with the lightest elements - hydrogen and helium - while less than a percent comprises heavier elements such as C, N, O, S, etc.

Up to now, some 180 molecules have been detected in the interstellar medium or in circumstellar shells [1; 2], ranging in complexity from molecular hydrogen (H_2) to the largest identified species, the C_{70} fullerene. In addition, a large number of isotopologues including D,^{13}C,^{18}O and ^{15}N have been detected [3–6]. The element carbon, with its ability to build covalent bonds in a wide variety of chemical reactions, is abundantly present. Some simple carbon-containing molecules, such as CN, CH, and CH^+ were detected already in the first half of the 20^{th} century, by transitions in the optical range [7–10]. In fact

Herzberg determined a value of the rotational temperature of the CN molecule at 2.3 K, within error margins equivalent to the temperature of the cosmic background radiation, in an epoch that the concept of the Big Bang was not yet conceived [11].

Many of the observed species have been identified via pure rotational emission lines that are largely found in the radio astronomical wavelength domain. These species possess a permanent dipole moment and among these are long unsaturated carbon chain radicals, cat- and ions, as well as stable and relatively complex organic compounds, such as dimethylether or ethylenglycol. Also a few non-polar species, such as the pure carbon molecules, C_2 [12] and C_3 [13; 14] have been detected, using UV-VIS or IR spectroscopy. Solid carbon components such as amorphous carbon, ices, diamond, coal, soot and graphite have been detected as species occurring in the ISM [15–17]. A large class of organic compounds present in space are the polycyclic aromatic hydrocarbons (PAHs). These are observed in emission in the near and mid-infrared corresponding to the typical C-C and C-H vibrational modes that get excited upon absorption of an energetic UV photon. With the recent detection of C_{60} and C_{70} also fullerenes are now formal compounds of the ISM [2]. The abundance of organic materials in space environments has been reviewed in Ref. [18].

1.1 Diffuse interstellar bands

The majority of the identified species have been observed in dense and dark interstellar clouds. In diffuse and translucent clouds, in which temperatures are higher and radiation fields more intense, only a handful of species has been unambiguously identified. In spite of the fact that significant progress has been achieved in understanding the chemistry of the interstellar medium, the chemical and astrophysical models cannot explain the several hundred unidentified absorption features known as "*diffuse interstellar bands*" or DIBs. DIBs are absorption features, which have been observed along many lines of sight toward reddened background stars in the Milky Way and even toward other galaxies.

The origin of these phenomena, observed in the near UV, VIS and near IR ranges (covering 400 to 1000 nm) constitutes the oldest unsolved puzzle of astronomical spectroscopy. The DIBs were observed in the early 20^{th} century by Mary Lea Heger. She reported two stationary features at 5780 and 5797 Å towards binary systems [19]. Later, systemic studies performed by Merrill, confirmed that the absorption bands were not affected by Doppler shifts associated with the radial velocities of the background sources, and proved that they should be of interstellar origin [20–22]. In the past 90 years, the elusive DIBs have attracted the attention of many astronomers and spectroscopists. A large numbers of DIBs (i.e., some 600 features so far) have been observed and characterized for band positions, and band profiles, including intensities

and widths. [23]. Very recently also DIBs at longer wavelengths in the near infrared were observed [24].

DIBs are usually observed as features with a linewidth much broader than that of stellar atomic line transitions. This is the reason they are referred to as diffuse. In view of their apparent widths they have been ascribed to molecular bands originating from electronic transitions in polyatomic molecules or small solid particles that are distributed in the interstellar medium [7; 22; 25]. Because the DIBs exhibit largely varying widths and intensities, that generally do not correlate, it is generally accepted that the carrier of the DIBs must be more than one species, or even more than one class of species.

The carriers of the DIBs are assumed to originate from molecules containing the most abundant elements in the ISM such as H, C, O and N [26–32]. Several hypotheses for DIB-carriers have been proposed, such as H_2 [33; 34], solid particles [35], free radicals [36], fullerene-like molecules [37–41], polycyclic aromatic hydrocarbons (PAHs) [42; 43], and carbon chains [44]. Two classes of molecules have been investigated in much detail over the last years: polycyclic aromatic hydrocarbons and their cations and carbon chain molecules of various kinds [44–46].

PAHs have been proposed as potential DIB-carriers in the mid-1980s [42; 47]. These species are considered to be abundant molecules in the interstellar medium [48], as they are considered to be largely photo-stable. Several PAHs and the corresponding cations such as naphthalene ($C_{10}H_8$) [49; 50], pyrene ($C_{16}H_{10}$) [51], coronene ($C_{24}H_{14}$), dehydrogenated cations of coronene ($C_{24}H_x^+$ where $x \in \{12, 10, 8, 6, 4, 2, 0\}$) [52] and ovalene ($C_{32}H_{14}$) [53] have been studied to search for DIB matches. However, the spectroscopic results observed so far have not produced convincing coincidences with known DIBs. The observational and laboratory studies on PAHs have been reviewed in Refs. [16; 54].

Carbon chain molecules have received interest since Douglas, in 1977, suggested that DIB features "*are caused by the absorption of polyatomic molecules and that the line width is the result of radiationless internal conversion between stable states*". He proposed that "*the absorbing species are long chain carbon molecules, C_n where n may lie in the range (5-15)*" [46]. Later on, unsaturated hydrocarbon chains - as distinct from pure carbon chains - were also proposed as possible DIB-carriers [55], as some of these molecules show electronic transitions with unresolved and broad rotational structures, similar to the broad and asymmetric profiles of the DIBs. In addition, the detection of many linear carbon-based chain molecules through radio astronomy in dense clouds strengthened the belief that electronic transitions of such species may be involved in the diffuse medium as well.

In the past two decades many laboratory investigations of the gas-phase spectra of neutral and ionic linear carbon-chains such as C_n ($n = 4-5$), hydrogenated derivatives (e.g., C_nH, $n = 3-12$), polyacetylene cations $HC_{2n}H^+$ and carbon anions (C_n^-) were performed [56]. Over the years several species were proposed as potential DIB carriers. Comparison of the laboratory spectrum of C_7^- in the gas phase with astrophysical data indicated that the measured

spectra of the origin and a large set of vibronic bands coincided with some DIBs within a ±2 Å limit [57]. The hypothesis that C_7^- is a carrier of DIBs had, however, to be withdrawn on the basis of subsequent high-quality astronomical data [58]. Spectroscopic investigations provided evidence that bare carbon chains such as C_5, C_6, ... C_{15}, as well as their cations and anions or their derivatives containing H or N are not responsible for the stronger DIBs features [59]. The cases for other carbon-based molecules such as l-C_3H_2, $HC_{2n}H^+$, C_{60}^+ and carbon rings of the size up to a hundred of atoms have been discussed in Refs. [59–61].

1.2 Thesis outline and summary

A variety of laser-based spectroscopic techniques have been used to record optical transitions of carbon-based molecules [62]. The general methodology for recording high-resolution gas-phase spectra of such species is to first record an absorption spectrum via matrix isolation spectroscopy. With the matrix data available, the gas-phase spectra of the neutrals and ionic radicals can be measured by a number of methods, such as cavity ring-down spectroscopy (CRD), resonant two-color two-photon ionization (R2C2PI), laser-induced fluorescence (LIF), trapped-ion photo fragmentation, and photo-detachment spectroscopy. The gas phase data provided by these techniques, specifically the methods based on recording direct absorption spectra, can be compared with observational data, for instance the DIBs profiles. As a second goal of high-resolution spectroscopic studies, geometrical and electronic structures of carbon-based molecules can be characterized.

In this thesis, laser spectroscopy of (hydro)-carbon-chain radicals of astrophysical interest is reported. Sensitive pulsed cavity ring-down techniques, combined with molecule formation in an expanding plasma, enable to record high-resolution absorption gas phase spectra of electronic transitions of a series of carbon chain radicals as well as their D- and ^{13}C- substituted isotopologues. A systematic study of the spectra - recorded at low temperatures in the range of several kelvins - allows us to characterize the spectroscopic constants in ground an excited electronic states, and this also provides information on molecular structure. This thesis is structured as follows:

In chapter 3, optical absorption in the $\widetilde{A}^2\Delta - \widetilde{X}^2\Pi$ electronic origin band of the linear -hydro-carbon-chain radicals C_5H and C_5D has been reinvestigated. Cavity ring-down spectroscopy and two types of plasma nozzles, in a slit and a pinhole configuration, have been used. The data analysis yields a value for the spin-orbit splitting in the upper electronic $^2\Delta$ state of $l-C_5H$. A contour analysis of the unresolved band profiles makes it possible to an estimate for the $\widetilde{A}^2\Delta$ state lifetime of 1.6 ± 0.3 ps.

In chapter 4, it is shown that deuterium labeling of nonlinear hydrocarbon chains is a useful approach to characterize molecular structure. This method has been applied for two trihydrogenated carbon chain radicals, C_9H_3 and

$C_{11}H_3$, by recording optical transitions of both species and their (partially) deuterated equivalents in the 19000 cm^{-1} region using cavity ring-down spectroscopy and plasma expansions constituting C/H, C/D, and C/H/D nonlinear chains. The number of observed bands, the quantitative determination of isotopic shifts, and supporting calculations show that the observed C_9H_3 and $C_{11}H_3$ spectra originate from $HC_4(CH)C_4H$ and $HC_4[C(C_2H)]C_4H$ species with $C_{2\nu}$ symmetry.

Chapter 5 presents rotationally resolved $\widetilde{A}^3\Sigma_u^- - \widetilde{X}^3\Sigma_g^-$ gas phase absorption spectra of partially and fully deuterated linear HC_7D and DC_7D radicals. These carbon chain radicals are generated in a supersonically expanding planar plasma, discharging a diluted gas mixture of acetylene and D-enriched acetylene in helium and argon. The spectral analysis of the recorded spectra yields accurate ground and excited state rotational parameters as well as origin band positions of HC_7D and DC_7D.

In chapter 6, a study of the $\widetilde{A}^1\Pi_u - \widetilde{X}^1\Sigma_g^+$ $000 - 000$ electronic band of tricarbon molecule (C_3) and its ^{13}C-substituted isotopologues is presented. Rotationally resolved absorption spectra of this origin band for all six isotopologues using cavity ring-down spectroscopy in a supersonically expanding planar plasma are observed. The band of $^{12}C_3$ is re-investigated, focusing on an experimental clarification of the rotational line intensities, and an extended Hamiltonian is presented to study a perturbation analysis of the $\widetilde{A}^1\Pi_u$ 000 upper state. For the five partially and fully ^{13}C substituted C_3 isotopologues spectra are presented and analyzed, resulting in a set of molecular constants characterizing the $\widetilde{A}^1\Pi$ 000 upper electronic state and the ground state molecular constants for two of the ^{13}C di-substituted isotopic species.

In chapter 7, we present for the first time $^2\Pi - \widetilde{X}^2\Pi$ electronic origin band spectra of long chain hydro-carbon radicals and their ^{13}C-fully substituted isotopologues ($^{13}C_8H$, $^{13}C_8D$, $^{13}C_{10}H$ and $^{13}C_{10}D$), as well as spectra with better S/N ratio for $C_{2n}H/D$, (n= $4 - 6$) species. A systematic study of the band profiles for different rotational temperatures provides information on estimate excited state rotational constants and to derive values for the upper state lifetimes.

CHAPTER 2

Experimental overview

The experimental setup used, is a generic pulsed cavity ring-down spectroscopic experiment for the detection of short-lived species in a plasma discharge, similar to the one described in Ref. [63]. The technical details for the production of various radicals are presented in the following chapters of this thesis. Here, we give an overview of the spectroscopic method and some general details of the experiment.

2.1 Pulsed-CRD absorption technique

Absorption spectroscopy measures the attenuation of intensity of incident electromagnetic radiation passing through sample. The decrease of radiation intensity can be described quantitatively by the Lambert-Beer law:

$$I^l_{(\nu)} = I^0_{(\nu)}\, e^{-\sigma(\nu)nl} \tag{2.1}$$

where $I^0_{(\nu)}$ is the intensity of an incident beam at frequency ν, $I^l_{(\nu)}$ is the intensity measured after passing a distance l through the absorbing medium, n is the number density of the absorbing species, and $\sigma(\nu)$ is the frequency-dependent absorption cross section. The product $\sigma(\nu)n$ equals the absorption coefficient $\alpha(\nu)$ which can be rewritten from Eq. (2.1):

$$\alpha(\nu) = \frac{1}{l} \ln(\frac{I^0_{(\nu)}}{I^l_{(\nu)}}) \tag{2.2}$$

This equation can be simplified by using the first-order Taylor expansion of the Lambert-Beer law with assuming $\alpha(\nu) \ll 1$ to :

$$\alpha(\nu) = \frac{I^0_{(\nu)} - I^l_{(\nu)}}{I^0_{(\nu)} l} \tag{2.3}$$

From this relation, it is evident that the amount of detectable absorption, i.e. measurement of $\alpha(\nu)$, depends on the detectable amount of intensity changes in the incident beam. An increase of the absorption path length l will improve the measurement sensitivity. Small variations in the incident beam intensity cannot be detected easily because of fluctuations of the light source, which appear as noise. Meanwhile, providing long absorption path lengths are usually not easily achievable, in practice for short-lived radical species.

Cavity ring-down spectroscopy (CRDS) is a spectroscopic method measuring direct absorption with improved sensitivity. Extremely long absorbing path lengths through a sample are accomplished using two highly reflective cavity mirrors. The first paper on the CRD technique was published in 1988 [64]. Later, this technique has been developed in various directions such as: Continuous Wave CRD (CW-CRD) [65; 66], Cavity Enhanced Absorption Spectroscopy (CEAS) [67], Phase Shift CRD (PS-CRD) [68], Polarization Dependent CRD (PD-CRD) [69], Evanescent Wave CRD (EW-CRD) [70; 71], Fourier Transform CRD (FT-CRD) [72]. Generic Pulsed CRD (P-CRD) [73] is the most commonly used technique, and it is the method used in our investigations. In the pulsed cavity ring-down method, a laser pulse of intensity I_{laser} is coupled into a high-finesse cavity of length L, consisting of two high-quality mirrors, with reflectivities on the order of $R = 99.9\%$ or 99.99%, and transmittance $T = 1-R$ (see Fig. 2.1). At the entrance mirror only a small part, 0.1 to 0.01% of the incident light, will enter the cavity, and the leakage from the cavity is around

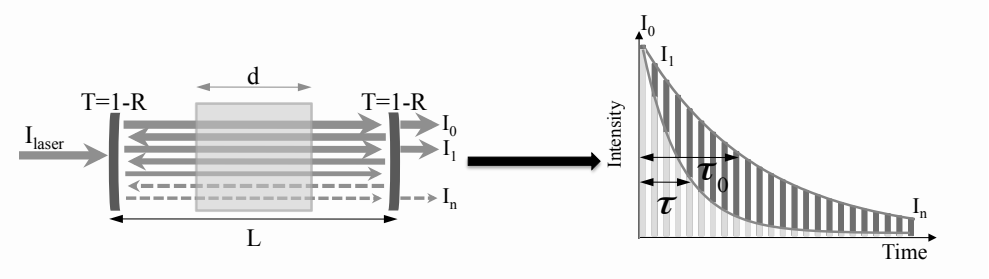

Figure 2.1 – Basic principle of cavity ring down spectroscopy.

0.1 to 0.01% per round-trip. The intensity of the first pulse leaking out of the cavity is $I_0 = T^2 I_{laser}$ and after n round-trips, its intensity is decreased to:

$$I_n = I_0 R^{2(n)} = I_0 e^{2(n)\ln(R)}. \tag{2.4}$$

The exponential decay of the intensity exiting the cavity can be expressed as a function of t:

$$I_{(t)} = I_0 e^{-(\frac{c}{L}|\ln(R)|)t} = I_0 e^{-(\frac{t}{\tau_0})} \tag{2.5}$$

where $I_{(t)}$ is the measured intensity at time t. The decay constant τ_0 in Eq. (2.5) is called the "ring-down time", which is directly related to the reflectivity R of the mirrors. With the approximation of $\ln(R) = -(1-R)$, the decay rate of τ_0 is given by:

$$\tau_0 = \frac{L}{c(1-R)} \tag{2.6}$$

Upon placing an absorber medium between the mirrors, the resulting intensity decays faster due to absorption in the sample. This results to smaller value of ring-down time as:

$$\tau = \frac{L}{c(1-R+\alpha(\nu)d+\beta_{scatt})} \tag{2.7}$$

where $\alpha(\nu)$ is the absorption coefficient of the absorber, β_{scatt} represents the scatter losses, and d is the effective pass length through the sample. In the case that the extra losses are only due to absorption, combining Eq. (2.6) and Eq. (2.7) gives:

$$\alpha(\nu)\frac{d}{L} = \frac{1}{c\tau} - \frac{1}{c\tau_0} = \frac{\tau_0 - \tau}{c\tau_0\tau} \tag{2.8}$$

where τ and τ_0 are the ring-down times in the presence and absence of an absorbing sample inside the cavity. From this and assuming $\tau \approx \tau_0$, the minimum detectable absorption in CRD is given by:

$$\left[\alpha(\nu)\frac{d}{L}\right]_{min} = \frac{1}{c\tau_0^2}\Delta\tau_{min} = \frac{(1-R)}{L}\left[\frac{\Delta\tau}{\tau_0}\right]_{min} \tag{2.9}$$

Using a tunable laser source the decay time can be recorded as a function of laser wavelength to record an absorption spectrum. Typically, the ring-down

times of CRD setups are in the order of nanoseconds for small cavities to micro- or even milliseconds for long cavities. For instance, for a typical cavity of length 50 cm, built from mirrors with $R = 99.995\%$, the ring-down time is around 30 μs. Eq. (2.9) implies that the CRD sensitivity can be increased by minimizing $\frac{\Delta\tau}{\tau_0}$.

It should be noted that there are no two mirrors with the same values of reflectivity. Hence, R in the above equations corresponds to the geometric average $\sqrt{R_1 R_2}$ of the reflectivities R_1 and R_2 of the mirrors. Furthermore, Eqs. (2.1) and (2.5) both exhibit a mono-exponential decay, and this is the basis for relating the ring-down time τ directly to the absorption quantity. Hence, a mono-exponential fit of Eq. (2.5) results in a correct estimation of $\alpha(\nu)$. In case that the CRD transient is not truly mono-exponential, a mono-exponential fit leads to an underestimation of the ring-down time and consequently to an incorrect value of $\alpha(\nu)$.

The CRD technique has two main advantages. The first is that the fluctuations of the light source, the most significant source of error in most conventional direct absorption methods, are removed in the CRD method. The measurement of the decay rate as a "ring-down time" is independent of the amount of light initially injected into the cavity. Another advantage of the CRD method is that effective path lengths are greatly enhanced, even to the level of a few kilometers for highly reflective mirrors, which makes this technique very sensitive and comparable with other sensitive detection methods such as laser-induced fluorescence (LIF), resonance enhanced multi-photon ionization (REMPI), and photo-acoustic spectroscopy (PAS). More details about CRD spectroscopy can be found in Refs. [73–77].

2.2 Laser system and wavelength calibration

A commercial tunable pulsed dye laser (Cobra-Stretch Sirah dye laser) pumped by the second or third harmonic output of a Nd:YAG laser (Spectra-Physics GCR-3) is used in our experiments for pulsed-CRD spectroscopy. The laser offers tunable light in the range of the UV to the near IR. The bandwidth of the laser beam is estimated to be around 0.07 cm^{-1} and can be improved to better than 0.035 cm^{-1} by aligning the grating of the laser resonator in a 2^{nd} order configuration. Precise alignment of the Sirah dye laser is required to maintain its narrow-band operation and reduce the fraction of amplified spontaneous emission (ASE) in the laser output. In some experiments the second harmonic output of the dye laser, produced in a DKDP or BBO crystal, has been used. The angular positions of the crystals, for phase-matching of the conversion process, are optimized by a feed-back loop using a tracking box, keeping the intensity of the frequency-doubled output at an optimum level. More details can be found in Ref. [78].

The observed non-linearity observed in the frequency scanning of the laser is compensated by simultaneously recording etalon fringes. For this, the etalon

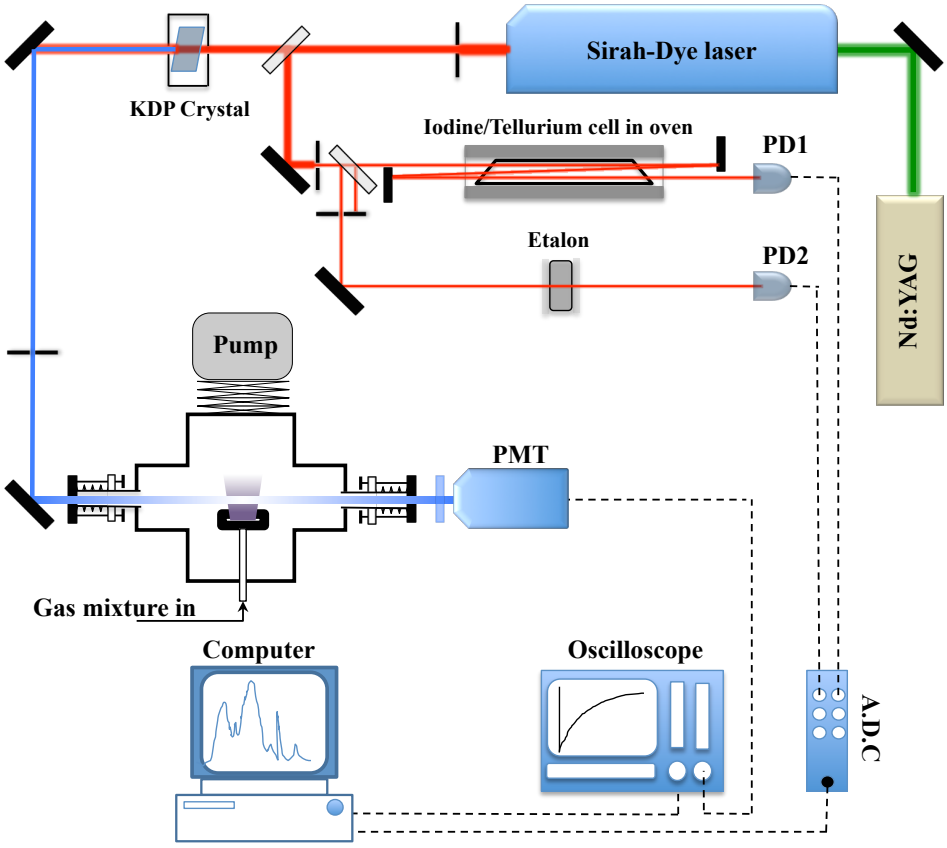

Figure 2.2 – Schematic diagram of the experimental setup.

peak positions are measured and linearized using fitting and linearization procedures with the aid of the PGopher software [79]. The resulting linearized etalon data are used for a relative calibration of the recorded spectra.

For absolute frequency calibration, simultaneously recorded absorption spectra of Iodine or Tellurium vapor are used. In the range of frequencies, where Iodine or Tellurium only have weak absorption lines, the absolute calibration is achieved by using spectral lines from species produced in the plasma, lines of C_2, CH, or metastable Argon. More details on relative and absolute calibration methods are described in the chapters of this thesis.

2.3 Generation of (hydro)-carbon chain transient radicals

The spectroscopy of transient carbon-containing radicals is possible through the generation of such species in electric discharges. Varieties of small radicals have been investigated by probing with electromagnetic radiation inside discharge cells, where rotational, vibrational and translational temperatures of

the radicals often are quite high [11; 80–83]. The recorded spectra, obtained by this method, are typically complex and exhibit transitions from high rotational or vibrational states, and suffer considerably from Doppler broadening at the high prevailing translational temperatures.

In supersonic free expansions of gases, molecules are expanded adiabatically from a high pressure region into a low pressure region of a vacuum chamber through a nozzle. This leads to a decrease in translational, vibrational and rotational temperatures of the sample. In the collimated parts of the molecular beams produced in this way, the Doppler broadening is significantly reduced [84]. Spectra obtained from molecular supersonic expansions have been reviewed in Refs. [84; 85]. To generate supersonically cooled molecules two types of nozzle have been used: (1) axially symmetric nozzles (circular or pinhole nozzles) and (2) planar or slit nozzles. The gas dynamics of expanding nozzle flows has been studied theoretically and experimentally in Refs. [86; 87]. The combination of a supersonic expansion and an electric discharge offers an elegant method to generate transient molecular species, radicals and ions, and the molecules of astronomical interests at low temperatures [88]. In this method, the desired radicals are generated in plasma discharge nozzles, which are connected to the reservoirs containing high-pressure precursor gases. These plasma sources have been applied to study small transients [89], cluster ions [90], as well as long carbon chains [91] and polycyclic aromatic hydrocarbons (PAHs) and their cations [50; 92–94].

Fig. 2.3 shows the pinhole and slit plasma nozzles used in our experiments to produce transient species of astrophysical interest. The source bodies consist of several plates (cathodes, insulator and anodes) in multi-layer geometries. The transient species are formed mainly in the plasma generated between the anode and cathode plate. The detailed structures of pinhole and slit nozzles are described in Ref. [88] and [95]. Strongly diluted gas mixtures (typically less than 1%) of C_2H_2, $^{13}C_2H_2$ and C_2D_2 in He/Ar, discharged in a pulsed plasma, yield a variety of hydro-carbon chains and their isotopologues downstream in the expansion. It has been found that a stable (pulsed) plasma can be obtained by optimizing parameters such as the amplitude and the temporal width of the discharge voltage, as well as the nozzle backing pressure and the duration of the gas pulse. These parameters can be experimentally optimized for the production of each species.

There are several advantages of using a slit plasma nozzle in comparison with a pinhole nozzle. Firstly, the transverse velocity components of the radicals parallel to the slit are smaller, resulting in a smaller Doppler line width. At the same time, the longer absorption path-length along the exit channel of the slit nozzle increases the optical density. Furthermore, in the slit nozzle, the densities of the species in the plasma downstream decrease more slowly with distance from the orifice ($\approx 1/R$) than for a pinhole nozzle ($\approx 1/R^2$). Thus the slit expansion exhibits more cooling collisions, resulting in an equilibration of vibrational, rotational and translational temperatures of

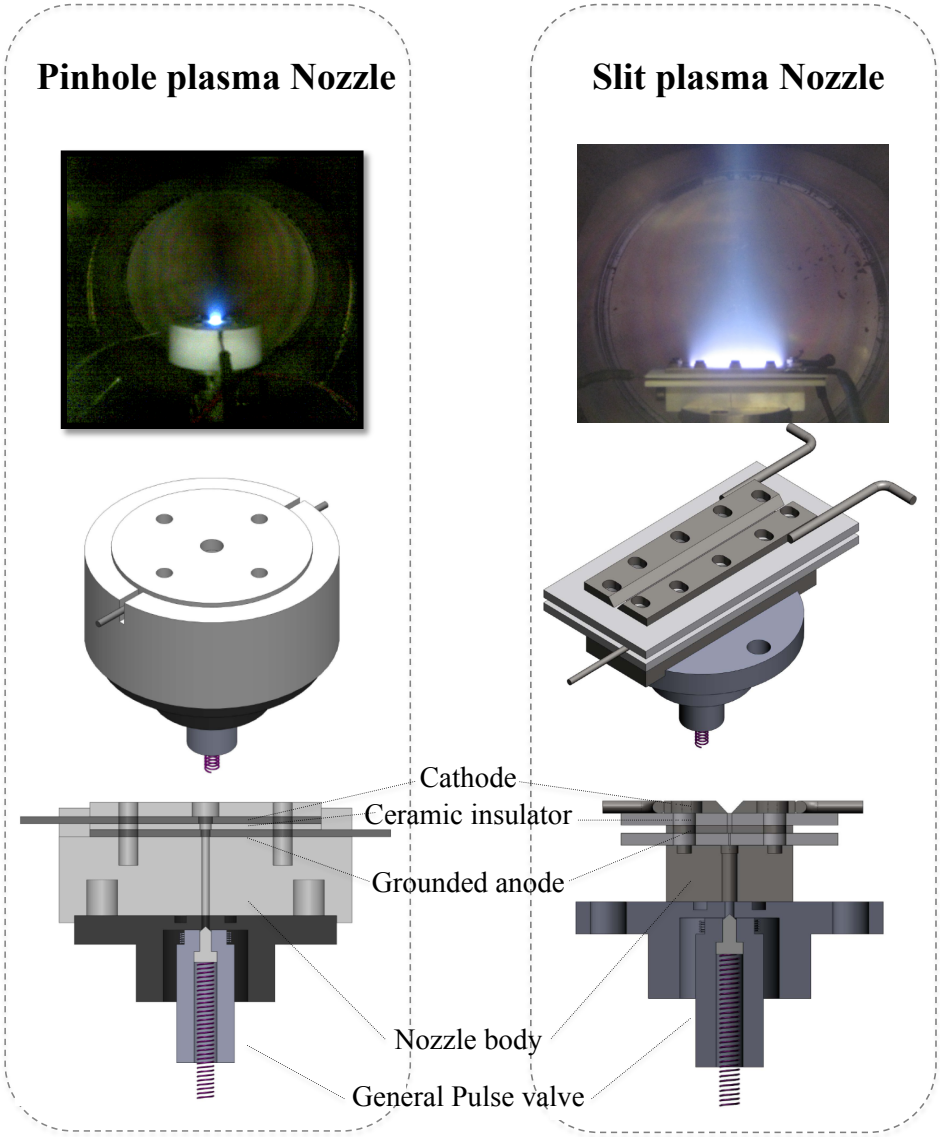

Figure 2.3 – Plasma nozzle sources. These sources are mounted to a pulsed valve system that runs typically at 8 Hz and provide a gas pulse that is discharged by applying a negative high voltage pulse (~ -1000 V) to the cathode plate, striking upstream towards the grounded anode plate. These two plates are isolated by ceramic insulators in both plasma sources. A gas pulse ($\sim$ 1 ms), with a typical backing pressure of $\sim$ 10 bar, is supersonically expanded into a vacuum chamber through a pulsed valve (General Valve, Series 9, 2 mm orifice) that is mounted on top a 30 mm$\times$0.3 μm multi-layer slit discharge nozzle or a pinhole nozzle with the plates of the diameter of the central holes of increasing: anode/insulator/cathode/insulator = 1.0, 1.5, 1.8 and 3.5 mm.

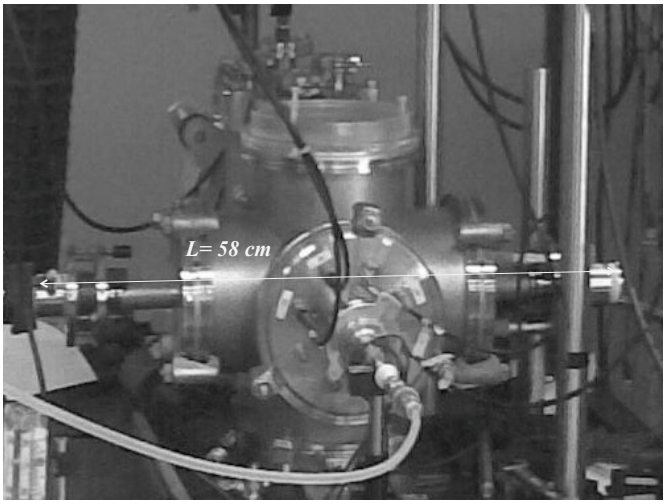

Figure 2.4 – Photograph of the vacuum chamber and optical cavity.

species. These properties make the slit plasma nozzle preferable for recording high resolution spectra.

A major disadvantage of such plasma sources is that they cannot generate radicals selectively, i.e., the technique is not mass-selective. In other words, a large number of species are formed simultaneously with the desired carbon chains in the plasma, including small radicals such as $C_2$and CH, that cover a wide wavelength range. Therefore, spectra of larger carbon chains are often blended by absorption features from small radicals. However, high resolution spectroscopy quite often allows to discriminate for specific species, moreover isotopic substitution experiments can help in identifying specific absorption bands.

2.4 Vacuum chamber and optical cavity

The vacuum chamber and optical cavity used in our experiments are shown schematically in Fig. 2.2, and in the photograph in Fig. 2.4. The vacuum chamber consists of a stainless-steel double cross-piece evacuated by a roots blower (Laybold-Heraeus) system with a total pumping capacity of 1000 m^3/h. The minimum pressure attainable in the chamber is $\sim 8.0 \times 10^{-3}$ mbar. The stability of the plasma can be seen viewed from the plasma emission radiation visible through a window installed on top of the chamber. The pressure in the chamber while running the plasma is typically $\sim 3 \times 10^{-2}$ mbar for the pinhole nozzle and $\sim 5 \times 10^{-2}$ mbar for the slit nozzle.

The high finesse optical cavity is mounted onto the chamber by attaching two highly reflective mirrors (typically, Research Electro Optics Inc or Leyertec) facing each other. The mirrors are mounted on two finely adjustable stages involving three high-precision threaded screws for aligning the cavity. To

protect the mirrors against dust and soot particles produced in the plasma, a stream of nitrogen is injected along the mirrors forming effective "nitrogen curtains". The typical pressure of the chamber with nitrogen flow turned on, is $\sim 2 \times 10^{-2}$ mbar in the absence of a gas pulse. Two tilted quartz windows are fixed on the back side of the mirror holders to seal the chamber.

2.5 Data Acquisition

The light leaking out of the cavity is detected with a photomultiplier Tube (PMT) which is connected to a digital oscilloscope (LeCroy, 350 MHz, 8-bit resolution). A typically recorded trace of the decay transient consists of 4000-5000 points, which is transferred to a computer for real-time computation and storage of the decay time. The exponential fitting of ring-down decay signals is achieved by the algorithm described in Ref. [96]. The other data such as the Iodine and Tellurium absorption reference spectra and the transmitted etalon fringe patterns are simultaneously recorded via photodiodes. The experiment and data acquisition are controlled by a LabView program (National Instruments).

CHAPTER 3

Spin-orbit splitting and lifetime broadening in the $\widetilde{A}^2\Delta$ electronic state of l-C_5H

Optical absorption bands at ∼18772 and ∼18807 cm^{-1}, previously assigned to $\widetilde{A}^2\Delta - \widetilde{X}^2\Pi$ electronic origin band transitions of the linear carbon-chain radicals C_5H and C_5D, respectively, have been reinvestigated. The spectra have been recorded in direct absorption applying cavity ring-down spectroscopy to a supersonically expanding acetylene/helium plasma. The improved spectra allow deducing a l-C_5H upper state spin-orbit coupling constant $A' = -0.7(3)$ cm^{-1} and a $\widetilde{A}^2\Delta$ lifetime of (1.6 ± 0.3) ps.

3.1 Introduction

Highly unsaturated carbon-chain radicals of the form C_nH have been identified in dark interstellar clouds through comparison of radio-astronomical observations with spectra obtained from microwave laboratory experiments [97; 98]. Among these species, the linear carbon chain radical l-C_5H has been observed around the carbon-rich star IRC+10216 and towards TMC-1 [99; 100]. A linear geometry has been calculated as its most stable isomer [101], and the ground state has been predicted to be a regular $^2\Pi$ state [102]. Dedicated laboratory work on microwave spectra has resulted in a set of accurate ground state parameters for both C_5H and C_5D [103; 104]. Electronic transition band systems of C_5H and C_5D have been reported in a mass-selective REMPI-TOF study in which spectral features at ∼18791 and 18824 cm^{-1} were assigned as origin band transitions from the electronic ground state to an electronically excited $^2\Delta$ state, respectively. This assignment was backed-up by *ab initio* predictions [105]. An $11\sigma \longrightarrow 3\pi$ electron excitation from a $\widetilde{X}^2\Pi$ ground state can result in excited $^2\Sigma^+$, $^2\Sigma^-$, and $^2\Delta$ states, and theoretical work shows that for C_5H the $^2\Delta$ state is the lowest among these states [106].

In this study, improved spectra are presented for the $\widetilde{A}^2\Delta - \widetilde{X}^2\Pi$ electronic origin band transitions of l-C_5H and l-C_5D, using a different technique based on cavity ring-down spectroscopy. The wavelength calibration is improved compared to previous work [105]. The spin-orbit splitting in the upper electronic $^2\Delta$ state of l-C_5H is determined. A contour analysis of the unresolved band profiles allows an estimate for the $\widetilde{A}^2\Delta$ state lifetime.

3.2 Experimental

Pulsed cavity ring-down (CRD) spectroscopy is used to record direct absorption spectra of C_5H and C_5D through a supersonically expanding hydrocarbon plasma. The expansion crosses the central axis of a high finesse optical cavity. This cavity consists of two highly reflective planoconcave mirrors (Research Electro-Optics, reflectivity ∼99.998% at 532 nm) positioned 58 cm apart and mounted on high precision alignment tools that are located on opposite sites of a high vacuum chamber. The latter is evacuated by a roots blower system with 1200 m^3/h pumping capacity. Tunable light in the 532 nm region is obtained from a Nd:YAG (355 nm) pumped dye laser (Sirah, Cobra-Stretch) that is focused into the cavity and light leaking out of the cavity is detected by a photo-multiplier visualizing separate ring-down events. Typical ring down events are of the order of 60 μs. The dye laser has a bandwidth of ∼0.07 cm^{-1} and this can be further improved to ∼0.035 cm^{-1} using the second order diffraction of the Littrow grating in the oscillator [107; 108]. An absolute frequency calibration is achieved with a precision better than 0.02 cm^{-1} by simultaneously recording an I_2 reference spectrum. The system runs at 10 Hz

and an accurate triggering scheme is used to temporally overlap the plasma pulse and the ringdown event.

Two different plasma sources are used. The design and operation of a pinhole plasma source has been documented in Ref. [109]. As a precursor gas for C_5H (or C_5D) a mixture of 0.4% C_2H_2/He (or 0.3% C_2D_2/He) is expanded with a backing pressure of ∼7 bar through an orifice ($\phi \approx 1.2$ mm). The gas mixture is discharged by applying a ∼300 μs long high voltage pulse (-1 kV/100 mA) during of ∼1 ms. Typical pressure in the vacuum chamber amounts to ∼0.01 mbar during plasma operation. The best achievable spectral resolution is limited to ∼0.12 cm^{-1} because of residual Doppler broadening in the pinhole jet expansion. The distance of the pinhole nozzle orifice to the optical cavity axis is set to 2 mm for C_5H (and C_5D) spectra recording, yielding an approximate rotational temperature of $T_{rot} \approx 30$ K.

An improvement in spectral resolution is possible, using a 3 cm×200 μm slit discharge nozzle. This system has been used in many studies and details are available from Ref. [63]. The resulting planar plasma provides a nearly "Doppler-free" environment and the linewidth is expected to be limited by the laser bandwidth. In addition, the effective absorption path length is longer. A diluted gas mixture of 1% C_2H_2/He is used and discharged at ∼10 bar backing pressure by applying a ∼400 μs long high voltage pulse (-750 V/100 mA) during a ∼1 ms gas pulse. In this case the typical pressure in the chamber is ∼0.04 mbar during slit jet operation. As the gas consumption in the slit nozzle geometry is substantial, only experiments for C_2H_2/He plasma expansions are performed.

The experiment is not mass selective and different transient molecules are formed simultaneously in the plasma jet. Consequently, besides the C_5H/C_5D spectra additional and (partially) overlapping transitions from other species are recorded. An unambiguous identification, however, is possible following the data recorded in the mass-selective REMPI-TOF experiment [105].

3.3 Results

Overview spectra for the $\widetilde{A}^2\Delta - \widetilde{X}^2\Pi$ electronic transition, as obtained using the pinhole discharge nozzle, are shown in the upper traces of Fig. 3.1 for C_5H (Fig. 3.1(a)) and C_5D (Fig. 3.1(b)). The C_5D spectrum is ∼35 cm^{-1} blue-shifted with respect to the C_5H spectrum. In each spectrum a stronger and a weaker band are clearly visible, despite of a partial spectral overlap with narrow features. To reduce the spectral congestion, a Doppler-free spectrum has been recorded for C_5H using the slit discharge nozzle. The resulting spectrum is shown in Fig. 3.2(a) for a laser bandwidth of ∼0.07 cm^{-1}. Fig. 3.2(b) shows the spectrum in the same frequency range but recorded for a much lower backing pressure of ∼2 bar. The latter conditions do not favor C_5H formation and only spectral features of small hydrocarbon compounds, such as C_2, C_3, CH, *etc.* are found. It is obvious that without these overlapping transitions the broad

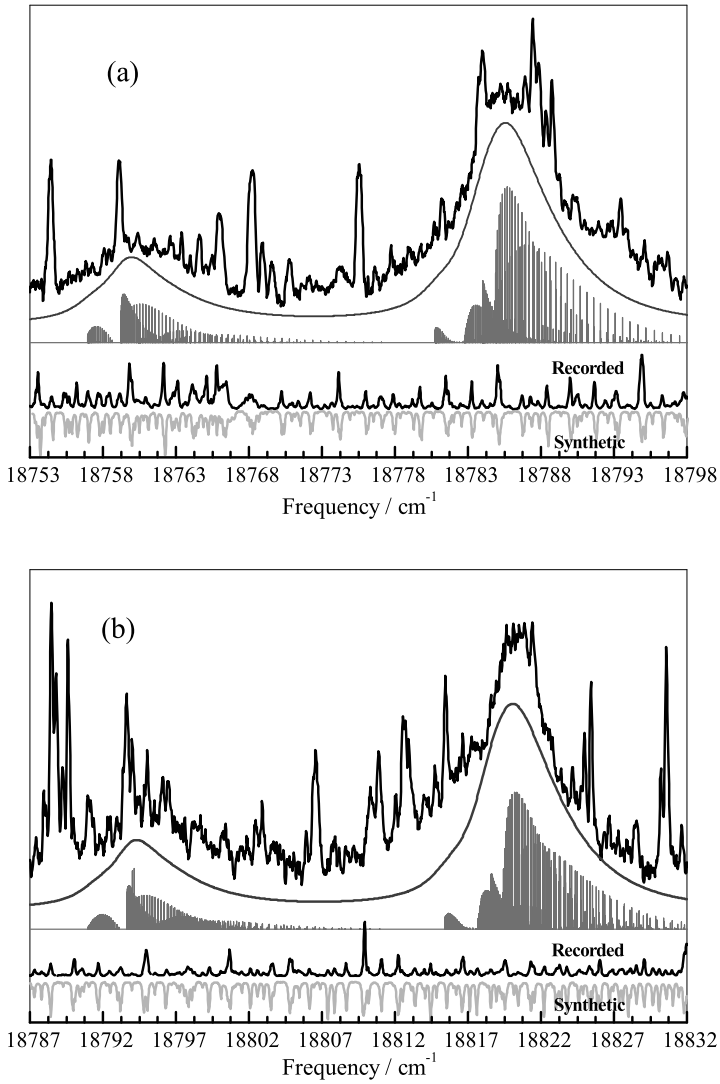

Figure 3.1 – $\widetilde{A}^2\Delta - \widetilde{X}^2\Pi$ origin band spectra for (a) C_5H and (b)C_5D. The upper traces in both panels show the cavity ring-down recordings using a pinhole nozzle. The sharp features in the observed spectra are due to overlapping absorptions of small radicals. The middle traces are the simulated spectra for a Lorentzian line width of $\Gamma = 3.3$ cm^{-1} and a Gaussian line width of 0.12 cm^{-1} assuming a rotational temperature of 30 K. The stick diagrams are simulations for a $\widetilde{A}^2\Delta - \widetilde{X}^2\Pi$ transition using the molecular parameters listed in Table 3.1. The simultaneously recorded I_2 reference spectra are also shown in the lower traces of both panels and matched to the synthetic I_2 spectrum for absolute frequency calibration.

profiles in Fig. 3.2(b) are identical to the mass-selective spectra recorded in the REMPI-TOF work (see the inset Figure 1 of Ref. [105]).

The $\widetilde{A}^2\Delta - \widetilde{X}^2\Pi$ transition of C_5H consists of two relatively broad and unresolved components. The stronger feature is at ∼18785.5(2) cm^{-1} and

the weaker at ∼18760.4(2) cm^{-1}. For a regular $\widetilde{X}^2\Pi$ ground state with an A'' value of ∼23.64 cm^{-1} [103], and for the low rovibronic temperatures in the plasma jet expansion, the lower $^2\Pi_{1/2}$ component is expected to be more populated than the higher $^2\Pi_{3/2}$ component. Actually, the relative intensity ratio is a measure for the cooling efficiency in the expansion. Consequently, the bands at 18785.5 and 18760.4 cm^{-1} can be assigned as the $\widetilde{A}^2\Delta_{3/2} - \widetilde{X}^2\Pi_{1/2}$ and $\widetilde{A}^2\Delta_{5/2} - \widetilde{X}^2\Pi_{3/2}$ components, respectively. The effective splitting of the maxima (Δ_{SO}) of the two bands amounts to ∼25.1 cm^{-1}, and is just a little larger than the A''-value. It reflects the net difference in spin-orbit splitting in ground and electronically excited state; Δ_{SO}=$|A'\Lambda' - A''\Lambda''|$, where $\Lambda = 0, 1$, and 2 depend on the Σ, Π, and Δ character of the electronic state, respectively, *i.e.* for a $^2\Delta - ^2\Pi$ transition here, $\Delta_{SO} = |2A' - A''|$. The transition starting from the $^2\Pi_{1/2}$ component is located at higher energy than the one starting from the $^2\Pi_{3/2}$ component. As the ground state is regular this means that the excited state must be inverted with the $\Delta_{5/2}$ level below the $\Delta_{3/2}$ level.

In Fig. 3.3 schematic energy level diagram is shown, summarizing these findings and explicitly including the spin-orbit splitting of both the $^2\Pi$ ground and $^2\Delta$ electronically excited state. This yields an estimated value of $A' \approx -0.7$ cm^{-1}. This A' value has not been derived in Ref. [105] where the assignment of the band system to a $\widetilde{A}^2\Delta$ was based on the outcome of *ab initio* predictions. The present non-zero spin-orbit value in the upper state provides additional experimental evidence for the correct assignment of the observed spectrum to an excited $^2\Delta$ state, as the $^2\Sigma^{+/-}$ states should not exhibit any spin-orbit splitting.

It should be noted that for such a weak spin-orbit coupling, the $^2\Delta$ excited state of C_5H is not a typical electronic state characterized by Hund's case (a), because of spin-uncoupling [110]. In this specific case, rovibronic transitions corresponding to $\widetilde{A}^2\Delta_{5/2} - \widetilde{X}^2\Pi_{1/2}$ and $\widetilde{A}^2\Delta_{3/2} - \widetilde{X}^2\Pi_{3/2}$ are also allowed, but they will be much weaker with respect to the $\widetilde{A}^2\Delta_{3/2} - \widetilde{X}^2\Pi_{1/2}$ and $\widetilde{A}^2\Delta_{5/2} - \widetilde{X}^2\Pi_{3/2}$ bands, and are not resolved here. These weak transitions have been taken into account in the simulated stick diagrams shown in Fig. 3.1 and Fig. 3.2.

The extracted values for the individual band positions are listed in Table 3.1. The resulting origin band value is given as well. In Ref. [105] only the maximum values for the stronger spin-orbit components are listed; 18791 cm^{-1} for C_5H and 18824 cm^{-1} for C_5D. These values are found to deviate from the values reported here: 18785.5 and 18820.6 cm^{-1}, respectively. It is unclear where this discrepancy comes. The present work relies on an absolute laser frequency calibration by simultaneously recording I_2 reference spectra (see Fig. 3.1 where the synthetic I_2 spectrum is shown as well) that are accurate within 0.02 cm^{-1}. A likely explanation is that the wavelengths and wavenumbers in Ref. [105] are given in air and have not been corrected for vacuum.

The observed bands are unresolved, even though the rotational constant B'' of C_5H is ∼0.08 cm^{-1}, and a $\sim 2B$ rotational progression therefore should

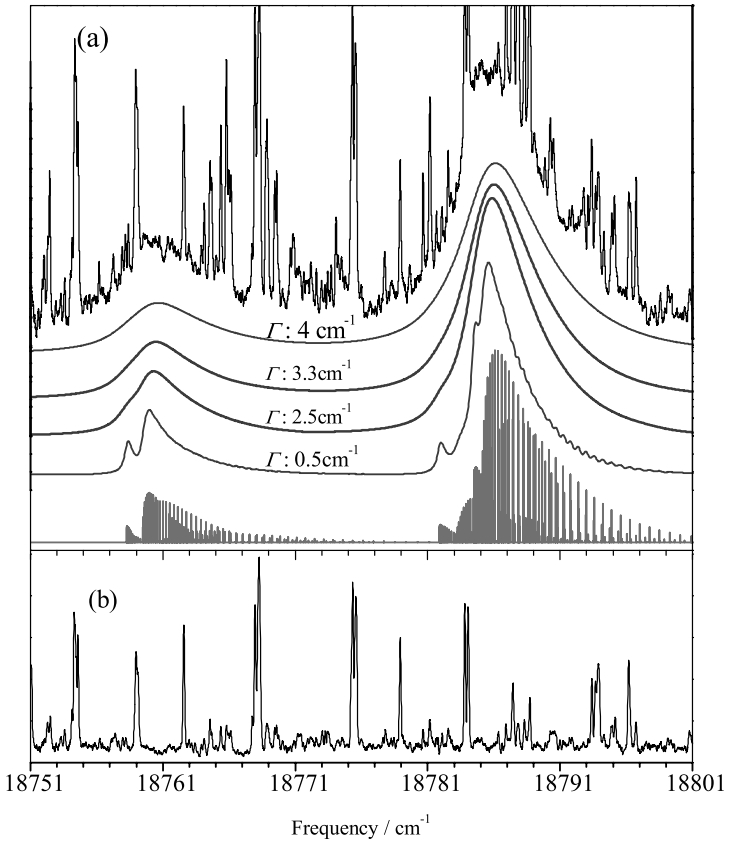

Figure 3.2 – (a) Recorded spectrum of the $\widetilde{A}^2\Delta - \widetilde{X}^2\Pi$ origin bands in C_5H using the slit discharge nozzle (upper trace) with a backing pressure of ∼10 bar. Simulated spectra for different Lorentzian line width values (Γ=0.5, 2.5, 3.3, and 4.0 cm^{-1}) are shown in the middle trace. The stick diagram for a $\widetilde{A}^2\Delta - \widetilde{X}^2\Pi$ transition is shown in the lower trace. (b) Recorded absorption spectrum of the $\widetilde{A}^2\Delta - \widetilde{X}^2\Pi$ origin bands in C_5H using the slit discharge nozzle with a backing pressure of ∼2 bar. In both panels a laser bandwidth of 0.07 cm^{-1} is used.

be easily resolvable within the experimental settings. This is illustrated by the artificial spectrum, shown as stick diagrams in Fig. 3.1 and Fig. 3.2, and simulated for a temperature of ∼30 K using PGopher [79]. The logical explanation for this observation is that the broadening is intrinsic and that the transitions to the $\widetilde{A}^2\Delta$ upper state must be lifetime broadened. This will be discussed later. Nevertheless, it is still possible to obtain information on the rotational constants for the excited state.

Empirical rotational contour fits of the observed spectra are performed using a standard Hamiltonian for a $^2\Delta - ^2\Pi$ transition. The ground state constants (B'', A'') are fixed to the available accurate values [103], while the excited state parameters (B', A', and the band origin ν_{00}), as well as the Lorentzian linewidth (Γ), can be varied to reproduce the experimental spectra. The best spectrally

fitted contour for the C_5H band shown in Fig. 3.2 is found for $A' \approx -0.7$ cm^{-1}, and a $B'/B'' \approx 1.06$ and (a Lorentzian linewidth) $\Gamma \approx 3.3$ cm^{-1}. This B'/B'' ratio is unexpected. For the other linear hydrocarbon chains whose electronic spectra can be rotationally resolved, it was found that the overall chain length slightly increases upon electronic excitation, resulting in a typical B'/B'' ratio smaller than 1 [107–109; 111–113]. The derived $B'/B'' > 1$ value means that the length of C_5H decreases upon electronic excitation. To confirm this finding, the stronger C_5H spin-orbit component at ∼18785.5 cm^{-1} has been recorded using the slit discharge nozzle at the best possible laser bandwidth of ∼0.035 cm^{-1}.

The resulting spectrum is shown in the upper trace of Fig. 3.4. As the band is featureless, special care has been taken to exclude the risk that the band profile is overfit. Instead the reliability of the spectral fitting is verified by varying the B'/B'' ratio from 0.9 to 1.1. This shifts the resulting value for the band origin (ν_{00}) from 18771.8 cm^{-1} to 18772.4 cm^{-1} but it does not influence the derived $A' = -0.7(3)$ cm^{-1} value. Simulated band contours are shown in the lower traces of Fig. 3.4 for $B'/B'' = 1.06$, 1.00, and 0.94. The observed band profile is indeed best fitted for a $B'/B'' \approx 1.06 \pm 0.04$ ratio. This confirms that in this specific case the effective length of the chain seems to shrink and a possible (but not conclusive) explanation could be that the

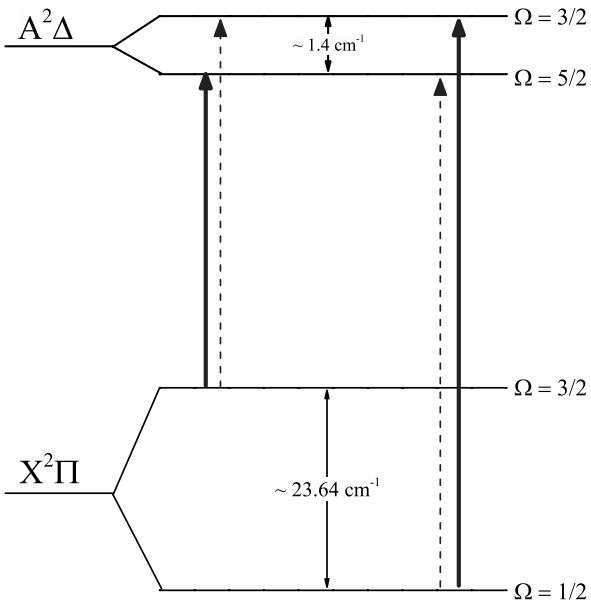

Figure 3.3 – Schematic energy level diagram for the $\widetilde{X}^2\Pi$ and $\widetilde{A}^2\Delta$ electronic states of C_5H. Solid-line arrows indicate the observed $\widetilde{A}^2\Delta_{3/2} - \widetilde{X}^2\Pi_{1/2}$ and $\widetilde{A}^2\Delta_{5/2} - \widetilde{X}^2\Pi_{3/2}$ bands. The dashed arrows represent the intrinsically weak (and not observed) $\widetilde{A}^2\Delta_{5/2} - \widetilde{X}^2\Pi_{1/2}$ and $\widetilde{A}^2\Delta_{3/2} - \widetilde{X}^2\Pi_{3/2}$ transitions.

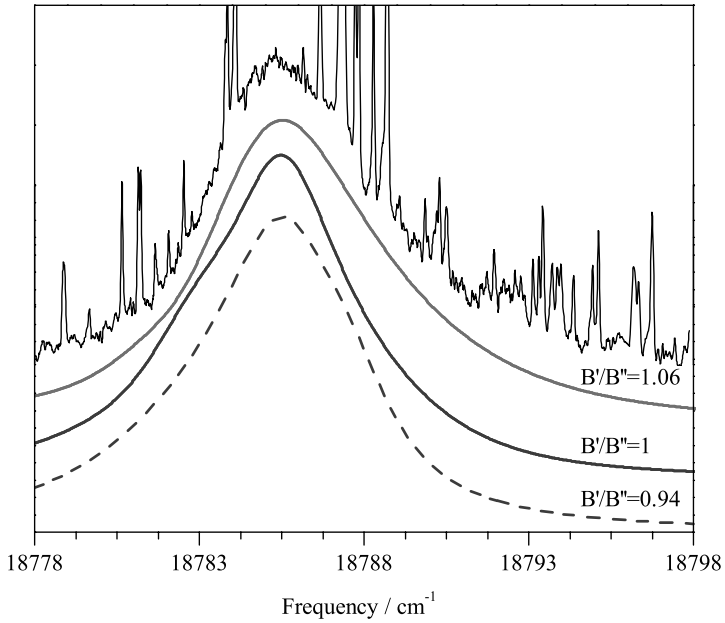

Figure 3.4 – A 0.035 cm^{-1} recording of the $\widetilde{A}^2\Delta_{5/2} - \widetilde{X}^2\Pi_{3/2}$ spin-orbit component of C_5H (upper trace). The lower traces show simulated spectra for three different B'/B'' ratios.

potential surface of the $\widetilde{A}^2\Delta_{3/2}$ state of l-C_5H chain has an energy minimum in a non-linear geometry due to Renner-Teller effect, as found for l-C_3H [114].

As stated above, the unresolved bands are indicative for an intrinsic lifetime broadening. In the spectral simulation, a Gaussian linewidth of ∼0.12 cm^{-1} is used. To reproduce the experimental spectrum shown in Fig. 3.2, the Lorentzian linewidth has to be determined. Simulated band contours for values of Γ = 0.5, 2.5, 3.3, and 4 cm^{-1} are shown in Fig. 3.2. Even though this is only an approximate way of determining the Lorentzian width, the observed profile is clearly best simulated for a value of $\Gamma = 3.3 \pm 0.5$ cm^{-1} (for $T_{rot} \approx 26$ K). This value for the Lorentzian line broadening parameter corresponds to a lifetime of (1.6 ± 0.3) ps for the upper $^2\Delta$ state of C_5H. Many of the conclusions derived above for C_5H also apply to C_5D. The rotational and spin-orbit coupling constants for the $\widetilde{X}^2\Pi$ ground states of l-C_5H have been reported in Ref. [104]. The band positions of the $\widetilde{A}^2\Delta_{3/2} - \widetilde{X}^2\Pi_{1/2}$ and $\widetilde{A}^2\Delta_{5/2} - \widetilde{X}^2\Pi_{3/2}$ transitions are found at ∼18820.6 and ∼18794.7 cm^{-1}, respectively, and the resulting effective spin-orbit splitting (Δ_{SO}) amounts to ∼25.9 cm^{-1}. An empirical contour fit is applied to the observed C_5D spectrum, fixing the available ground state parameters in Ref. [104] and using the same values for B'/B'' ratio and Lorentzian width Γ that are derived for C_5H above. From this analysis, the value for the spin-orbit coupling constant A' is found to be between 0 and -1.0 cm^{-1}. The substantial overlap of narrow features

with the weak $\widetilde{A}^2\Delta_{5/2} - \widetilde{X}^2\Pi_{3/2}$ component does not allow a more accurate determination of this value. All relevant values are summarized in Table 3.1.

3.4 Discussion

The magnitude of the deduced spin-orbit coupling constants A' in the $\widetilde{A}^2\Delta$ state of C_5H is much smaller than that in its $\widetilde{X}^2\Pi$ ground state. Similar behavior has also been observed for CH ($A'' \approx 28.05$ cm^{-1}, $A' \approx -1.0$ cm^{-1}) [115–117] and C_3H ($A'' \approx 14.2$ cm^{-1}, $A' \approx 0$) [114; 118] radicals. It is noted that the three hydrocarbons $C_{2n+1}H$ ($n = 0 - 2$) have similar electronic configuration in their $\widetilde{X}^2\Pi$ ($...\sigma^2\pi^1$) and $\widetilde{A}^2\Delta$ ($...\sigma^1\pi^2$) states, where the $\widetilde{A}^2\Delta$ state of C_3H splits into two A^2A' and B^2A'' states because of very strong Renner-Teller effect [114; 119–122]. The comparable spin-orbit coupling constant between CH and C_5H indicates that the spin-orbit coupling in $\widetilde{X}^2\Pi$ and $\widetilde{A}^2\Delta$ states of C_5H may originate from the one-electron spin-orbit coupling in atomic $2p_\pi$ orbitals of C(^{3}P, $2s^22p^2$) and C(^{3}D^o, $2s2p^3$), respectively.

Further, previous work shows that, because of very strong Renner-Teller effect [114; 118–122], the effective spin-orbit coupling constants of C_3H have become much smaller than those of CH, particularly in the $\widetilde{A}^2\Delta$ state of C_3H the spin-orbit coupling have been completely quenched. Here, the result that both spin-orbit coupling constants in $\widetilde{X}^2\Pi$ and $\widetilde{A}^2\Delta$ states of C_5H are slightly smaller than those for CH, respectively, may hint at significant Renner-Teller effects in both states of C_5H, but the Renner-Teller effect for C_5H should be weaker than that for l-C_3H.

The short lifetime of the excited state of C_5H, ∼1.6 ps, must be due to a fast radiationless process, most likely a strong intramolecular interaction, as all possible dissociation or isomerization products of l-C_5H lie energetically higher than the $\widetilde{A}^2\Delta$ state [101]. It is expected that l-C_5H in its $\widetilde{X}^2\Pi$ ground state also exhibits a substantial Renner-Teller effect. Theoretical calculations have predicted a large splitting (∼100 cm^{-1}) for the lowest bending vibrational mode ν_9 owing to strong Renner-Teller interaction in the ground state of l-C_5H [101]. Highly excited vibronic levels with Δ symmetry in the $\widetilde{X}^2\Pi$ ground state therefore are expected to be close to the $\widetilde{A}^2\Delta$ state and eventually to strongly interact with the $\widetilde{A}^2\Delta$ electronic state via vibronic couplings. Such couplings offer a possible relaxation channel responsible for the observed short lifetimes in the excited states of the l-$C_{2n+1}H$ homologous series. A more detailed picture of the exact nature of the internal conversion process is not available at this stage.

3.5 Conclusion

An improved interpretation of recalibrated $\widetilde{A}^2\Delta - \widetilde{X}^2\Pi$ electronic origin band transitions of l-C_5H and l-C_5D is presented. It has been possible to derive

Table 3.1 – $^2\Delta$ upper state parameters for C_5H and C_5D. (all values are in cm^{-1}).

	$\widetilde{A}^2\Delta - \widetilde{X}^2\Pi$	CRD				REMPI-TOF [105]	
		ν	$(\nu_D - \nu_H)^a$	B'/B''^b	A'	ν	$(\nu_D - \nu_H)^a$
C_5H	0_0^0	18772.1(3)		1.06 ± 0.04	-0.7±0.3		
	$\widetilde{A}^2\Delta_{3/2} - \widetilde{X}^2\Pi_{1/2}$	18785.5				18791	
	$\widetilde{A}^2\Delta_{5/2} - \widetilde{X}^2\Pi_{3/2}$	18760.4					
C_5D	0_0^0	18806.5	34.4	1.06[c]	(-1,0)[d]		
	$\widetilde{A}^2\Delta_{3/2} - \widetilde{X}^2\Pi_{1/2}$	18820.6	35.1			18824	33
	$\widetilde{A}^2\Delta_{5/2} - \widetilde{X}^2\Pi_{3/2}$	18794.7	34.4				

[a] The isotopic shift of the band position of C_5D with respect to C_5H.
[b] The B'/B'' ratio is dimensionless, where B'' are fixed to the values available in Refs. [103; 104].
[c] Fixed.
[d] The accurate value can not be determined.

accurate band positions and to determine the spin-orbit coupling constants in the upper states for both isotopologues. The broadening of the spectra is interpreted in terms of a short lifetime of (1.6 ± 0.3) ps for the $\widetilde{A}^2\Delta$ state which is likely associated with strong vibronic couplings.

Acknowledgments

This work was supported by the Netherlands Foundation for Fundamental Research of Matter. The work has been performed within the context of the Dutch Astrochemistry Network NWO program. Harold Linnartz thanks Stichting Physica. Mohammad Ali Haddad thanks the Iran Ministry of Science, Research and Technology for financial supports. Samples of C_2D_2 were generously made available by Prof. S. Schlemmer from University of Cologne.

CHAPTER 4

Structure determination of the nonlinear hydrocarbon chains C_9H_3 and $C_{11}H_3$ by deuterium labeling

A systematic deuterium labeling experiment is presented that aims at an unambiguous determination of the geometrical ground state structure of the C_9H_3 and $C_{11}H_3$ hydrocarbon chains. Cavity ring-down spectroscopy and special plasma expansions constituting C/H, C/D, and C/H/D are used to record optical transitions of both species and their (partially) deuterated equivalents in the 19000 cm^{-1} region. The number of observed bands, the quantitative determination of isotopic shifts, and supporting calculations show that the observed C_9H_3 and $C_{11}H_3$ spectra originate from $HC_4(CH)C_4H$ and $HC_4[C(C_2H)]C_4H$ species with $C_{2\nu}$ symmetry. This result illustrates the potential of deuterium labeling as a useful approach to characterize the molecular structure of nonlinear hydrocarbon chains.

4.1 Introduction

Unsaturated hydrocarbon chains of the form $C_nH_m^{(+/-)}$ (typically with $m \leq n$), both linear and nonlinear, have been topic of many experimental and theoretical studies. These reactive species are found as important intermediates in combustion and flames [123; 124], in plasma environments [125], and in dense interstellar clouds, where many hydrocarbons have been unambiguously identified [126–128]. Studies dedicated to the structural determination of these transient intermediates have made it possible to improve models to characterize combustion processes or to quantify reaction pathways of relevance to interstellar chemistry. In the past three decades, microwave and infrared studies have provided accurate molecular constants yielding structure determinations for a large number of unsaturated hydrocarbon chain species [129; 130].

More recently high resolution optical work in combination with high level *ab initio* results have extended these studies to electronic transitions [131; 132]. This is important, particularly for those systems, where microwave and infrared data are not available. However, for many nonlinear carbon chain radicals exhibiting small rotational constants or lifetime broadened transitions, rotational resolution cannot be obtained and consequently unambiguous structure determinations are not possible. In such cases isotopic labeling provides an additional tool to derive structural information.

In this contribution the ground state structures of two trihydrogenated carbon chain radicals, C_9H_3 and $C_{11}H_3$, are conclusively determined from gas phase optical spectra and deuterium (D) labeling. Their optical spectra have been previously reported [133; 134], but molecular structures were not unambiguously determined because of a lack of rotationally resolved transitions in the experimental spectra. C_7H_3, a smaller molecule with similar molecular form, was identified as a three-member ring chain with C_s symmetry [135], but density functional theory (DFT) calculations [136] predicted that the open chain isomers of $HC_4(CH)C_4H$ and $HC_4[C(C_2H)]C_4H$ with $C_{2\nu}$ symmetry (shown in Fig. 4.1) are the most likely carriers of experimental spectra previously recorded for C_9H_3 and $C_{11}H_3$, respectively. For C_9H_3 this is consistent with the outcome of a recent study [109] in which the *K*-stack structure could be resolved.

4.2 Experimental and theoretical methods

The C_9H_3 and $C_{11}H_3$ spectra are recorded by pulsed cavity ring-down spectroscopy through a supersonically expanding hydrocarbon plasma [137]. The plasma source employs a modified pinhole discharge nozzle which has been described in detail previously (see Ref. [109] for details). An acetylene/helium gas mixture is expanded with a backing pressure of ~ 7 bar into a high vacuum chamber that is pumped by a roots blower system with a total capacity of 1000 m^3/h. The typical chamber pressure during jet operation amounts to 0.03

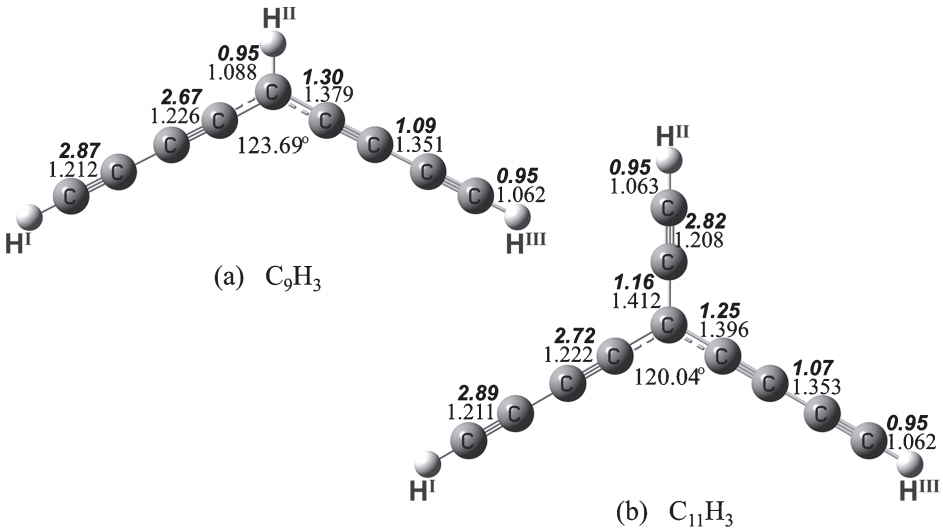

Figure 4.1 – The molecular structure of (a) C_9H_3 and (b) $C_{11}H_3$. The bond lengths (in Angstrom) and the angles of the bend $C_{2\nu}$ structures, calculated at the DFT-B3LYP/6-311G** level, are indicated by regular numbers. The calculated bond indices of the two radicals are indicated by bold numbers.

mbar. Three gas mixtures, 0.5% C_2H_2/He, 0.3% C_2D_2/He, and (0.2% C_2H_2 + 0.2% C_2D_2)/He, are used in the present experiment to create C/H, C/D, and C/H/D plasma jets, respectively. A high voltage pulse ($\sim$ 300 μs and -1000 V) is applied to the electrodes of the discharge nozzle coinciding with a gas pulse of 1 ms duration which is generated by a pulsed valve (General Valve, Series 9) mounted to the vacuum chamber. The plasma expansion perpendicularly crosses the optical axis of a 58 cm long optical cavity, $\sim$7 mm downstream.

This cavity consists of two plano-concave mirrors (Research Electro-Optics, reflectivity > 99.995% in the wavelength range 515 - 550 nm) that are mounted on high precision alignment tools. Cavity ring-down events are obtained by injecting a fraction of the laser pulse into the high-finesse optical cavity. Light leaking out of the cavity is detected by a photomultiplier tube and typical ring-down times amount to 60-80 μs. The setup is operated at 10 Hz, determined by the repetition rate of a tripled Nd:YAG laser (355 nm) that is used to pump a dye laser (Sirah, Cobra-Stretch, bandwidth $\sim$0.04 cm^{-1}). A trigger scheme allows optimizing the timing of the ring-down event with respect to the discharge pulse. The absolute laser frequency is calibrated with a precision better than 0.02 cm^{-1} using an I_2 absorption reference spectrum that is recorded simultaneously.

The analysis of the experimental data is supported by a set of additional DFT calculations. The structural optimization of stationary points and vibrational frequencies in the ground state are calculated by the DFT-B3LYP (Ref. [138]) method. Complete active space multi-configuration SCF calculations [139] with 7 electrons and 8 orbitals in the active space (CASSCF [129; 130]) are performed for the derived molecular structures to characterize the role

of the active molecular orbitals involved in the observed electronic spectra. For this, the 6-311G(*d,p*) basis set is used. All these calculations are performed using the GAUSSIAN 03 software package [140].

4.3 Results and analysis

4.3.1 Experimental spectra

The absorption spectra of C_9H_3 and $C_{11}H_3$ recorded through a C/H plasma are shown in Figs. 4.2(a) and 4.3(a). Based on previous studies involving mass-spectrometric detection [133; 134], these spectra can be unambiguously assigned to electronic transitions of C_9H_3 and $C_{11}H_3$. Here, similar absorption bands are observed in a C/D plasma (shown in Figs. 4.2(b) and 4.3(b)) at blue shifts of ∼70 cm^{-1}, corresponding to isotopically shifted C_9D_3 and $C_{11}D_3$. In a mixed C/H/D plasma all these bands are observed as well (though weaker), and in addition several new bands appear (shown in Figs. 4.2(c) and 4.3(c)). The latter exhibit similar band contours and comparable intensities, and are ascribed to partially deuterated (D) isotopologues.

4.3.2 Structure determination of C_9H_3

Rotational constants for C_9H_3 have been previously estimated as $A'' \approx 0.215$ cm^{-1}, and $B'' \approx C'' \approx 0.0159$ cm^{-1} from a spectral contour fit of an *a*-type transition, reflecting the nonlinear structure of this molecule [109]. For large molecules such as C_9H_3, the difference between rotational constants of different isotopologues is generally small. The DFT calculations confirm that the rotational constants of different isotopologues are very comparable (see Table 4.1), and within the uncertainties of the empirical contour fit from the experimental spectrum of C_9H_3. The experimentally derived rotational constants of C_9H_3 are therefore also used in the spectral simulations of the individual absorption bands of the different isotopologues in order to derive the band origin positions of the recorded optical transitions.

In total twelve bands attributed to six D-isotopologues of C_9H_3 are obtained from spectral simulations (Fig. 4.2(c)), which are assigned to two transition types (Table 4.2): The 0_0^0 electronic origin band transitions and vibronic transitions involving excitation of a low-frequency vibration ($\nu \sim 38$ cm^{-1}) in the upper electronic state. The intensity ratio of the six isotopologue bands is quantitatively determined to be ∼ 1:1:2:2:1:1 from measurement of a 50%/50% H/D mixture in the C/H/D plasma (Fig. 4.2). The number of observed D-isotopologues and their intensity ratio, subsequently allows for a conclusion on the symmetry of the molecule and the position of the three hydrogen atoms. This is explained below.

We label the three hydrogen positions in the geometric structure of C_nH_3 as H^I, H^{II}, and H^{III}, and use $H^IH^{II}H^{III}$ as an overall label. We discriminate three possible cases:

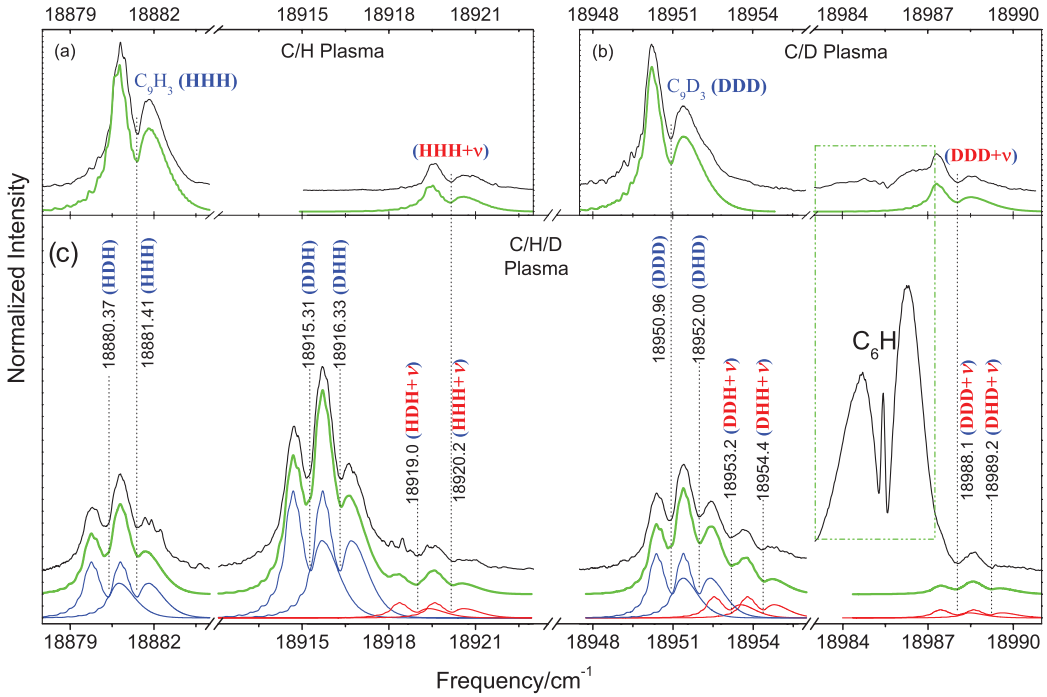

Figure 4.2 – Experimentally observed spectra (upper black lines) of C_9H_3 and its D-isotopologues recorded through: (a) C/H, (b) C/D, and (c) mixed C/H/D plasma. The simulated spectra are shown by bold green lines in each panel. In panel (c), the individual simulations of the observed *a*-type bands are shown: blue lines indicate the 0_0^0 transitions and red lines vibronic bands, respectively. The vertical dotted lines indicate the band origins of the 0_0^0 transitions for the D-substituted species (identified in blue) and the vibronic bands (identified in red). The absorption at ∼18985 cm^{-1} in panels (b) and (c) is due to the C_6H radical. (See Ref. [113]).

Table 4.1 – Calculated rotational constants and low-frequency bending vibrations (in cm^{-1}) for all D-isotopologues of C_9H_3 and $C_{11}H_3$ at the B3LYP/6-311G** level.

	$C_9(H^IH^{II}H^{III})$				$C_9(H^IH^{II}H^{III})$			
Isotopologues[a]	*A*	*B*	*C*	ν^b	*A*	*B*	*C*	ν^b
HDH	0.2101	0.0164	0.0152	42.26	0.0449	0.0171	0.0124	38.78
HHH[c]	0.2268	0.0164	0.0153	42.43	0.0475	0.0171	0.0126	38.86
DDH/HDD	0.2044	0.0159	0.0148	41.41	0.0443	0.0166	0.0121	38.02
DHH/HHD	0.2203	0.0159	0.0148	41.58	0.0468	0.0166	0.0123	38.09
DDD	0.1988	0.0155	0.0143	40.58	0.0437	0.0162	0.0118	37.27
DHD	0.2140	0.0155	0.0144	40.73	0.0462	0.0162	0.0120	37.33

[a] D-isotopologue formulas are indicated by the permutation $H^IH^{II}H^{III}$.
[b] Scaled by a factor of 0.968 (Ref. [141]).
[c] Values used for spectral simulations of all isotopologues.

1. The three hydrogen atoms are non-interchangeable, corresponding to three fundamental H/D isotopic shifts of Δ^I, Δ^{II} and Δ^{III}. In this

case, eight D-isotopologues should be observed: HHH, DHH, HDH, HHD, DDH,DHD, HDD, and DDD, with indicative isotopic shifts of ∼0, Δ^{I}, Δ^{II}, Δ^{III}, $\Delta^{I}+\Delta^{II}$, $\Delta^{I}+\Delta^{III}$, $\Delta^{II}+\Delta^{III}$,$\Delta^{I}+\Delta^{II}+\Delta^{III}$. In a plasma with equal amounts of H and D, these eight species will have approximately the same abundance, i.e., their absorbance should be comparable.

2. Two hydrogens are at symmetrical positions, e.g., H^{I} and H^{III} due to a plane of symmetry or a C_2 axis. The two unique hydrogen positions correspond to two fundamental H/D isotopic shifts of $\Delta^{I/III}$ and Δ^{II}. In this case, the isotopologues DHH and DDH are identical to HHD and HDD, respectively. Thus, six D-isotopologues should be observed: HHH, HDH, DHH/HHD, DDH/HDD, DHD,and DDD, with indicative isotopic shifts of ∼ 0, Δ^{II}, $\Delta^{I/III}$, $\Delta^{I/III}+\Delta^{II}$, $2\Delta^{I/III}$, $2\Delta^{I/III}+\Delta^{II}$, and a statistical intensity ratio of ∼1:1:2:2:1:1, respectively.

3. The three hydrogens are fully symmetrical within a $C_{3\nu}$ or D_{3h} molecular point group, i.e., there exists only one unique hydrogen position in the molecular structure. In this case, four D-isotopologues are expected: HHH, DHH, DDH, and DDD, with indicative isotopic shifts of $\sim 0, \Delta, 2\Delta, 3\Delta$, and a statistical intensity ratio of ∼ 1:3:3:1, respectively.

These arguments only hold when H- and D-substitutions at different molecular sites are energetically comparable, i.e., when the number of observed D-isotopologues of a trihydride and their statistical abundances in a reactive plasma are determined by molecular symmetry and unique (i.e., noninterchangeable) hydrogen positions in its geometric structure. Because of the high electronic temperature in a helium plasma, reactive intermediates are always formed very fast. In local thermodynamic equilibrium, therefore, it is assumed that the production probabilities of (partially) deuterated and hydrogenated hydrocarbon chain radicals are approximately the same.

A comparison with the experimental results, presented in Fig. 4.2, shows that neither the simplest case of a C_1 molecular point group (with eight expected D-isotopologues) nor a point group of the highest possible symmetry, C_{3v} or D_{3h} (with three equivalent H/D positions) apply. Instead the six different observed D-isotopologues must arise from two hydrogen atoms in symmetrical positions in C_9H_3 due to a plane of symmetry or a C_2 axis in its geometric structure. The observed intensity ratio is fully consistent with the statistically expected one.

In the following we define for C_9H_3 that H^{I} and H^{III} act as the two interchangeable H-atoms. From the observed isotopic shifts and intensity ratios, the spectral assignments of the six observed isotopologues (indicated by the permutation $H^{I}H^{II}H^{III}$) can be obtained (see Fig. 4.2(c) and Table 4.2). Values for the two fundamental H/D isotopic shifts are determined as +34.9 cm^{-1} ($\Delta^{I/III}$) and -1.0 cm^{-1} (Δ^{II}).

In our previous work [109], we predicted from the observation of a partially resolved rotational spectrum that the most likely symmetry of C_9H_3 is C_2 or

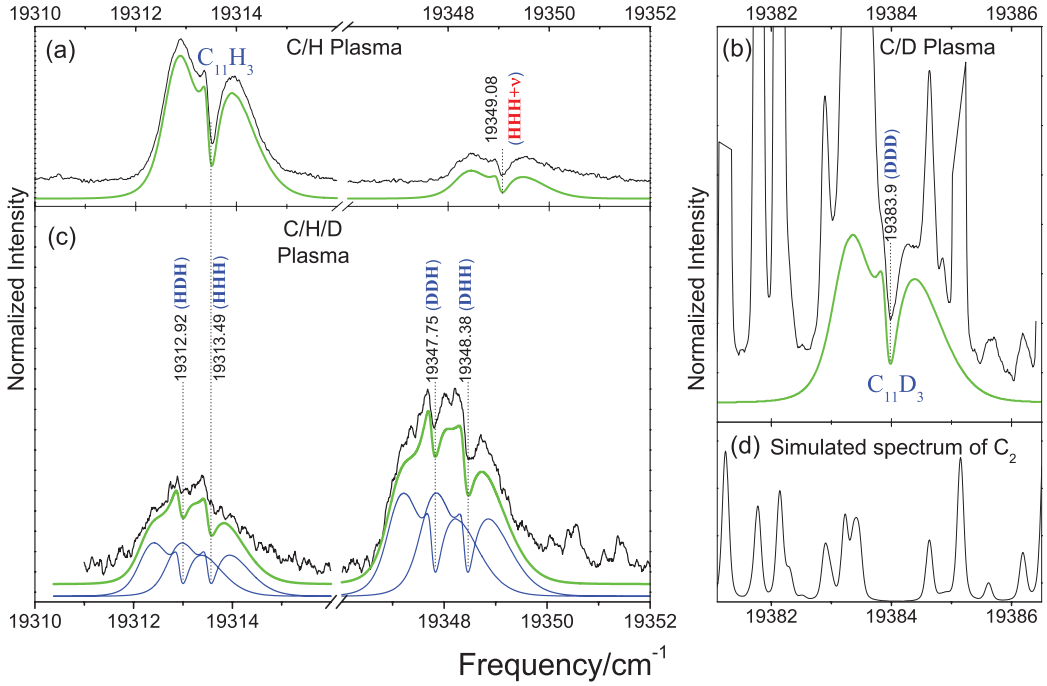

Figure 4.3 – Experimentally observed spectra (upper black lines) of $C_{11}H_3$ and its D-isotopologues recorded through (a) C/H, (b) C/D, and (c) C/H/D plasma. The simulated spectra are represented by bold green lines. In panel (c), the individual simulations of the observed *a*-type bands are shown by blue lines. The spectrum in panel (d) consists of simulated rotational lines of C_2 which overlap with the electronic origin band of $C_{11}D_3$.

$C_{2\nu}$, which is consistent with the D-labeling results found here. Obviously, the observation of the number and intensity ratio of different D-isotopologues is unambiguous, and more conclusive than the partially resolved rotational progression previously observed for a series of coinciding rotational transitions.

In Ref. [136], the molecular structures, rotational constants, and vertical electronic transition energy for 15 different C_9H_3 isomeric structures have been calculated by DFT. Eight structures have $C_{2\nu}$ symmetry. Convolving the electronic transition energy and indicative rotational constants derived from the experimental spectra, only the $HC_4(CH)C_4H$ with $C_{2\nu}$ symmetry (shown in Fig. 4.1(a)) exhibits both a 1^2A_2-X^2B_1 electronic transition (*a*-type) with comparable vertical excitation energy and a set of matching rotational constants. For this specific structure, extended calculations have been performed on the H/D shifts of the low-frequency vibration ($\Delta\nu$) at the B3LYP/6-311G** level. The results are summarized in Tables 4.1 and 4.2. As shown in Table 4.2, the calculated values agree well with the experimentally determined values. From this we conclude that the structure of the observed C_9H_3 is $H^{(I)}C_4(CH^{(II)})C_4H^{(III)}$.

4.3.3 Structure determination of $C_{11}H_3$

The 0_0^0 electronic origin band transition and the vibronic transition involving excitation of a low-frequency vibration ($\nu \sim 36$ cm^{-1}) in the upper electronic state of $C_{11}H_3$ are clearly observed in the C/H plasma following a similar pattern as for the C_9H_3 case (Fig. 4.3(a)). Both of the two bands comprise of unresolved P- and R-branch profiles, separated by a relatively weak Q-branch contour. The K-stack structure is not resolved. A rotational contour fit using an a-type transition in a nonlinear molecule is applied to the electronic origin band spectrum of $C_{11}H_3$, as shown in Fig. 4.4. This yields indicative values of the molecular constants: $A'' \approx 0.05$ cm^{-1}, $B'' \approx C'' \approx 0.015$ cm^{-1}, and $\Delta(A - (B + C)/2) \approx 0.01$ cm^{-1}. These values are substantially smaller than for C_9H_3. The experimentally derived $C_{11}H_3$ rotational constants are accurate enough to be used in the spectral simulations of the individual absorption bands of the different D-isotopologues.

As shown in the panels (b) and (c) of Fig. 4.3, only the electronic origin band transition of the D-isotopologues of $C_{11}H_3$ can be seen in C/D and C/H/D plasma. The electronic origin band of $C_{11}D_3$ is found to coincide with overlapping C_2 absorption lines. Origin band positions are derived from a contour fit, using the approximate rotational constants derived for $C_{11}H_3$, yielding the values as summarized in Table 4.2. The simulated spectra are included in Fig. 4.3 as well.

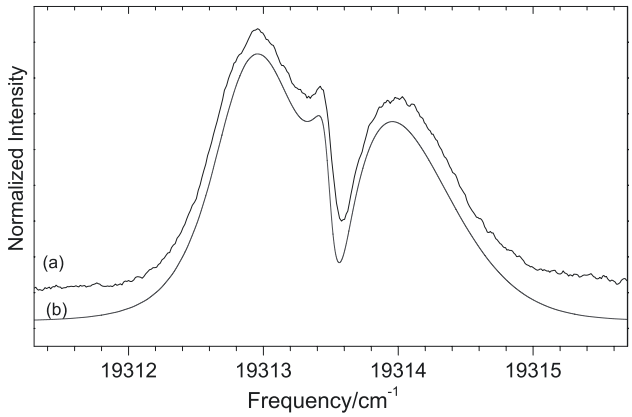

Figure 4.4 – The electronic origin band spectrum of $C_{11}H_3$. Trace (a): P- and R branch contour resolved experimental spectrum; (b): simulated spectrum by an a-type transition (with a Gaussian linewidth of ∼0.07 cm^{-1} and rotational temperature of ∼11 K) from an empirical contour fitting.

The number of isotopic bands, their relative intensities and the observed H/D isotopic shifts is consistent with a molecular $C_{11}H_3$ structure with two unique hydrogen positions, i.e., the carrier of the observed $C_{11}H_3$ spectrum has a C_2 or $C_{2\nu}$ symmetry as well. The corresponding values of the two fundamental H/D isotopic shifts are deduced as +34.9 cm^{-1} ($\Delta^{\mathrm{I/III}}$) and −0.6

cm^{-1} (Δ^{II}), respectively. These values are close to the C_9H_3 ones. The nearly identical value for $\Delta^{I/III}$ in C_9H_3 and $C_{11}H_3$ indicates a likely similarity between their geometric structures, namely, a similar substructure containing H^{I} and H^{III}. This means that $C_{11}H_3$ is as C_9H_3 but with a $C_2H^{(II)}$ group substituting the $H^{(II)}$ atom, i.e., $HC_4[C(C_2H)]C_4H$ (Fig. 4.1(b)). The rotational constants, the low-frequency vibration, and the vertical electronic transition energy of this structure predicted by DFT calculations (see Ref. [136], as well as Table 4.1) are in reasonable agreement with the experimentally derived values. CASSCF calculations show that the $1\,^2A_2 - X^2B_1$ electronic transition (a-type) of this structure involves very similar electronic configuration and excitation scheme as in C_9H_3 (see the panels (a) and (b) of Fig. 4.5). The similarity of the $HC_4C^*C_4H$ substructure and the involved electronic excitation should result in an approximately identical value of the H/D isotopic shift $\Delta^{I/III}$ between C_9H_3 and $C_{11}H_3$, which is confirmed by our experimental observations.

It should be noted that two of the other $C_{11}H_3$ isomeric structures listed in Ref. [136] (labeled as B6 and B11) also have a $C_{2\nu}$ symmetry and can be described by a set of rotational constants that is close to the values derived here. However, the low-frequency vibrations and the vertical electronic transition energies of these structures as predicted by DFT calculations (see Ref. [136]) deviate substantially from the experimentally derived values. Further, these two isomeric structures have no structural similarity with the determined $C_{2\nu}$ structure of C_9H_3, which is inconsistent with the observation of nearly identical values of the H/D isotopic shift $\Delta^{I/III}$ in C_9H_3 and $C_{11}H_3$. This leads to the conclusion that the isomeric structure of the observed $C_{11}H_3$ must be $H^{(I)}C_4[C(C_2H^{(II)})]C_4H^{(III)}$, as illustrated in Fig. 4.1(b).

4.4 Discussion

The structural similarities between different unsaturated hydrocarbons can be derived from their H/D isotopic shifts. The H/D isotopic shift in an electronic transition of a polyhydride originates from the change of zero point energy upon electronic excitation [142], which is related to the difference of the molecular structure in lower and upper state. In both C_9H_3 and $C_{11}H_3$, the prominent isotopic shift, $\Delta^{I/III}$, is exactly the same ($+34.9$ cm^{-1}), and this makes it likely that the electronic excitation arises from a mutual substructure $H^{(I)}C_4C^*C_4H^{(III)}$. The near-zero value of Δ^{II} indicates that upon electronic excitation there is almost no change in the H^{II}-containing substructures of the two molecules. This is confirmed by calculations on the Wiberg bond indices and the active molecular orbitals in C_9H_3 and $C_{11}H_3$. The calculations show that the distribution of the conjugated Π bonds in the $HC_4C^*C_4H$ substructure of the two molecules is almost the same (see Figs. 4.1 and 4.5).

The observed origin band positions for C_9H_3 and $C_{11}H_3$ are close and do not reflect the typical "particle in a one-dimensional box "behaviour, i.e., lower absorption energies for increasing conjugated chain lengths [131; 143]. Indeed,

Table 4.2 – The spectral assignment and isotopic shift (all values in cm^{-1}) of the observed isotopologues of C_9H_3 and $C_{11}H_3$

	Origin bands			Vibronic bands			
Isotopologues $C_n(H^IH^{II}H^{III})$	T_0	Δ^a		T_ν	ν^b	$\Delta\nu_{obs.}{}^a$	$\Delta\nu_{calc.}{}^{a,c}$
C_9(HDH)	18880.37(5)	-1.04(6)	Δ^{II}	18919.0(1)	38.6(1)	-0.2(1)	-0.17
C_9(HHH)	18881.41(2)	0		18920.21(3)	38.80(5)	0	0
C_9(DDH/HDD)	18915.31(5)	+33.90(6)		18953.2(1)	37.8(1)	1.0(1)	-1.02
C_9(DHH/HHD)	18916.33(5)	+34.92(6)	$\Delta^{I/III}$	18954.4(1)	38.1(1)	-0.7(1)	-0.86
C_9(DDD)	18950.96(2)	+69.55(3)		18988.05(5)	37.1(1)	-1.7(1)	-1.85
C_9(DHD)	18952.00(5)	+70.59(6)		18989.2(1)	37.2(1)	-1.6(1)	-1.70
C_{11}(HDH)	19312.92(5)	-0.6(1)	Δ^{II}				
C_{11}(HHH)	19313.49(3)	0		19349.08(3)	35.6(1)		
C_{11}(DDH/HDD)	19347.75(5)	+34.3(1)					
C_{11}(DHH/HHD)	19348.38(5)	+34.9(1)	$\Delta^{I/III}$				
C_{11}(DDD)	19383.9(1)[d]	+70.4(1)					
C_{11}(DHD)	-	-					

[a] Δ denotes the isotopic shift with respect to the main isotopologue C_n(HHH).
[b] Vibrational frequency in the upper electronic state: $\nu = T_\nu - T_0$.
[c] Calculated H/D isotopic shift for the lowest bending vibration at the B3LYP/6-311G** level. (See also Table 4.1).
[d] Blended with C_2 absorption lines. (See Fig. 4.3(b)).

the chain length along the conjugated Π bond does not really increase when adding two C-atoms along the $C_{2\nu}$ symmetry axis. In contrast, it is expected that the C_7H_3 radical, with a geometric structure previously determined as a three-membered ring bearing chain, should exhibit rather different H/D isotopic shifts compared to C_9H_3 and $C_{11}H_3$. Indeed, the reported H/D isotopic shift for the fully deuterated C_7D_3 is $\sim +50$ cm^{-1} [135].

The obtained H/D isotopic shifts can be compared to those of other linear hydrocarbon chains. The isotopic shifts $\Delta^{\mathrm{I/III}}$ ($\sim +34.9$ cm^{-1}) of C_9H_3 and $C_{11}H_3$ is very close to the H/D isotopic shifts of C_5H ($\sim +33.8$ cm^{-1} for C_5D) and HC_9H ($\sim +38.8$ cm^{-1} for HC_9D) [105; 144]. As shown in Fig. 4.5, the calculated molecular orbitals of the linear C_5H and HC_9H indicate that the conjugated Π bonds in the two linear chains are indeed very similar to those in C_9H_3 and $C_{11}H_3$. Figure 4.1 shows that the substructure $HC_4C^*C_4H$ in C_9H_3 and $C_{11}H_3$ has the form of two combined C_5H chains or a bent HC_9H structure, with a bent angle of $\sim$120° which is very close to the typical bond angle of aromatic rings. To understand these correlations also theoretically, extended CASSCF calculations have been performed on the C_9H_3 and HC_9H configurations. The result shows that the two pairs of active MOs in C_9H_3, ($2a_2$ and $11b_2$) and ($13a_1$ and $3b_1$), are correlated to the degenerate ($3\pi_g$) and ($4\pi_u$) orbitals in HC_9H, respectively. Specifically, the former two pairs are split from the latter two π orbitals when the nine-carbon containing chain changes from a linear to a bent conformation. These structural correlations also suggest that nonlinear open chain species have the potential to act as intermediates in

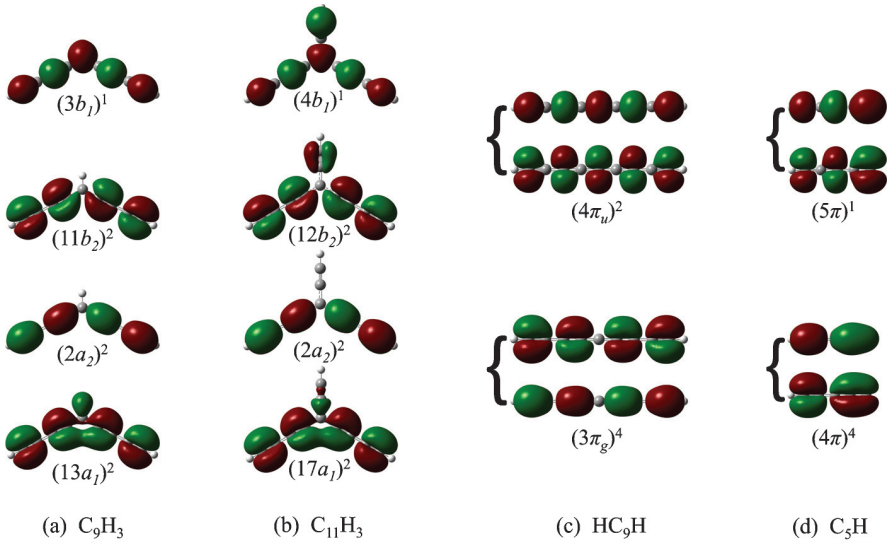

Figure 4.5 – Panels (a) and (b): calculated active molecular orbitals (MOs) in C_9H_3 and $C_{11}H_3$. Panels (c) and (d): calculated active π MOs in the conjugated Π bonds of C_5H and HC_9H. The experimental spectra shown in Figs. 4.2 and 4.3 arise from the $a_2 \rightarrow b_1$ electronic excitations from the ground state configurations shown in panels (a) and (b), respectively.

the formation of polycyclic aromatic rings in a reactive plasma or combustion flame.

4.5 Conclusion

In conclusion, the results presented here show that deuterium labeling is a useful approach to characterize the molecular structure of polyhydrogenated carbon chains. Specifically the structures of C_9H_3 and $C_{11}H_3$ molecules were determined from their optical spectra. In general, optical spectra of D-substituted species can provide molecular symmetry information of polyhydrides, as well as chemical bond correlations in the substructures containing D-labeled hydrogen. The described method may become more challenging for the D-labeling of a polyhydride with a larger number of hydrogen atoms, because the cumulative variety of isotopologues will likely result in overlapping isotopic bands. In such cases, the isotopic labeling in mass-selective detection schemes, such as REMPI-TOF and ion trap spectroscopy, may provide a useful alternative.

CHAPTER 5

Rotationally resolved $\widetilde{A}^3\Sigma_u^- - \widetilde{X}^3\Sigma_g^-$ electronic transition of HC_7D and DC_7D

Rotationally resolved $\widetilde{A}^3\Sigma_u^- - \widetilde{X}^3\Sigma_g^-$ gas phase absorption spectra of the partially and fully deuterated linear HC_7D and DC_7D radicals are presented. The carbon chain radicals are generated in a supersonically expanding planar plasma discharging a gas mixture of acetylene and D-enriched acetylene in helium and argon. Spectra are recorded in direct absorption using cavity ring-down spectroscopy. The spectral analysis yields accurate ground and excited state rotational parameters as well as origin band positions of 19880.18(2) cm^{-1} for HC_7D and 19943.18(2) cm^{-1} for DC_7D. Interferences in the observed spectra provide evidence for the triplet structure of the ground and excited states, while an indicative value of 0.3 ns is derived for the upper state lifetime, associated with non-radiative decay processes.

5.1 Introduction

Highly unsaturated carbon chain radicals have been identified in dark interstellar clouds following radio-astronomical observations [126; 127]. Centrosymmetric chains such as $NC_nN^{(+)}$ and $HC_nH^{(+)}$ are expected to exist in the interstellar medium as well but are radio-silent given their lack of a permanent dipole moment [56]. These chains are only detectable via low lying bending modes, typically in the sub-millimeter region, as demonstrated for C_3 [145] or via infrared spectra of vibrational bands [146; 147]. Optical transitions offer another alternative, particularly towards diffuse and translucent clouds, where electronic transitions of carbon chains have been associated with diffuse interstellar band features [44]. The electronic $\widetilde{A}^3\Sigma_u^- - \widetilde{X}^3\Sigma_g^-$ transitions of the odd-polyyne $HC_{2n+1}H$ series have been investigated experimentally. Their electronic absorption spectra have been recorded in 5 K neon matrices, providing origin band transitions as well as transitions to vibrationally excited states in the $\widetilde{A}^3\Sigma_u^-$ state [148]. Guided by these data gas, the phase spectra have been recorded for $HC_{2n+1}H$ (n=2-6), using different spectroscopic techniques such as two-color two-photon-ionization [149] and cavity ring-down spectroscopy [150]. The latter technique has resulted in rovibronically unresolved spectra of $HC_{2n+1}H$ species and their corresponding partially or fully deuterated isotopologues using a pinhole plasma expansion. In more recent work [108], partially resolved spectra for HC_7H have been reported, using a planar plasma source with a reduced Doppler broadening in combination with an improved laser bandwidth. The present study utilizes the same method and extends results to HC_7D and DC_7D. Band origin positions of these two isotopologues have been reported previously, but a rotational analysis is lacking so far.

5.2 Experimental

The gas-phase electronic spectra of linear HC_7D and DC_7D are recorded by pulsed cavity ring-down spectroscopy. The experimental set-up has been described in detail in Refs. [63; 108; 107], and is explained here only briefly. The partially and fully deuterated carbon chain radicals are generated by discharging a gas pulse of 1 ms duration (0.15% C_2D_2 or ∼0.35% C_2H_2 + 0.15% C_2D_2 in a 7:3 He:Ar mixture) in the throat of a slit nozzle. Adding argon to the expansion gas improves the carbon chain production efficiency. The gas is expanded with a backing pressure of about 10 bars through a long and narrow (3 cm ×300μm) slit that is positioned parallel to the laser beam and off-set by a few mm with respect to the optical axis of a high finesse cavity, consisting of two high reflectivity mirrors. Tunable light with a bandwidth of ∼ 0.035 cm^{-1} is generated by a tripled Nd:YAG laser (355 nm, 8 Hz) pumped dye laser (Sirah, Cobra-Stretch), operated in a second order grating configuration, and spatially filtered before it is focused into the optical cavity. Light leaking

out of the cavity is detected by a photo-multiplier tube. The laser frequency is accurately calibrated by simultaneously recording a 650°C tellurium vapor absorption spectrum and linearized using an etalon with a free spectral range of 0.7 cm^{-1}. This yields an absolute laser frequency accuracy of 0.02 cm^{-1}.

5.3 Results and discussion

5.3.1 HC_7D

Panel (b) of Fig. 5.1 shows the recorded electronic $\widetilde{A}^3\Sigma_u^- - \widetilde{X}^3\Sigma_g^-$ origin band transition of HC_7D. The observed band exhibits a partially resolved rotational structure that is spectrally polluted by overlapping narrow transitions due to other (smaller) hydrocarbon compounds. This is illustrated in panel (c) for expansion conditions not in favor of carbon chain formation – lower backing pressures and lower discharge current – from which the polluting peaks can be easily discriminated. The spacing between individual rotational transitions in P- and R-branchs of the asymmetric HC_7D molecule is not similar to the symmetric HC_7H (or DC_7D) species, as spin-statistics do not apply; i.e., the spacing between subsequent rotational transitions is approximately $2B$, rather than $4B$. An expanded view of the spectrum (panel (a) of Fig. 5.1) illustrates that many of the individual transitions indeed can be resolved.

For a $^3\Sigma$ electronic state, rotational levels are split into triplet fine structure levels F_1 for $N = J - 1$, F_2 for $N = J$ and F_3 for $N = J + 1$, due to spin-spin interaction of the unpaired electrons. The constant λ_ν signifies the spin-spin coupling constant for a particular vibrational state ν. In the case that $|\lambda_\nu| \ll 4BJ$, the energy eigenvalues of triplet fine structure levels of the same N are close to each other and N is a good quantum number for assigning rotational transitions. Under this assumption the rotational analysis of the spectrum can be performed by simulating an effective $^1\Sigma - ^1\Sigma$ transition, assuming that spin-rotation and spin-spin interaction are not affecting the overall pattern too much. Simulations are performed with PGopher software [79]. Since ground state constants have not been reported for HC_7D and DC_7D, the spectrum is simulated based on estimated values of B_0'' and B_0', assuming that B_e'/B_0' and B_e''/B_0'' ratios yield similar values as for HC_7H in Ref. [108]. In addition, the value of the rotational ground state constant of HC_7D, $B_e'' = 0.02706$ cm^{-1} has been calculated at B3lyp/6-311++G** level using GAUSSIAN 03 software [140]. Guided by the simulated spectrum, in total 24 P-branch and 5 R-branch transitions are identified in the $\widetilde{A}^3\Sigma_u^- - \widetilde{X}^3\Sigma_g^-$ origin band of HC_7D. These transitions fully reproduce during independent scans.

The measured frequencies are used in the final least-squares fit to derive the value of molecular parameters of HC_7D. For this, the band origin (T_{00}) and rotational constants (B'' and B') are fitted simultaneously. Inclusion of distortion constants, D'' and D' (fixed to the values derived for HC_6N in Ref. [151]) effectively improves the quality of the fit. The resulting parameters

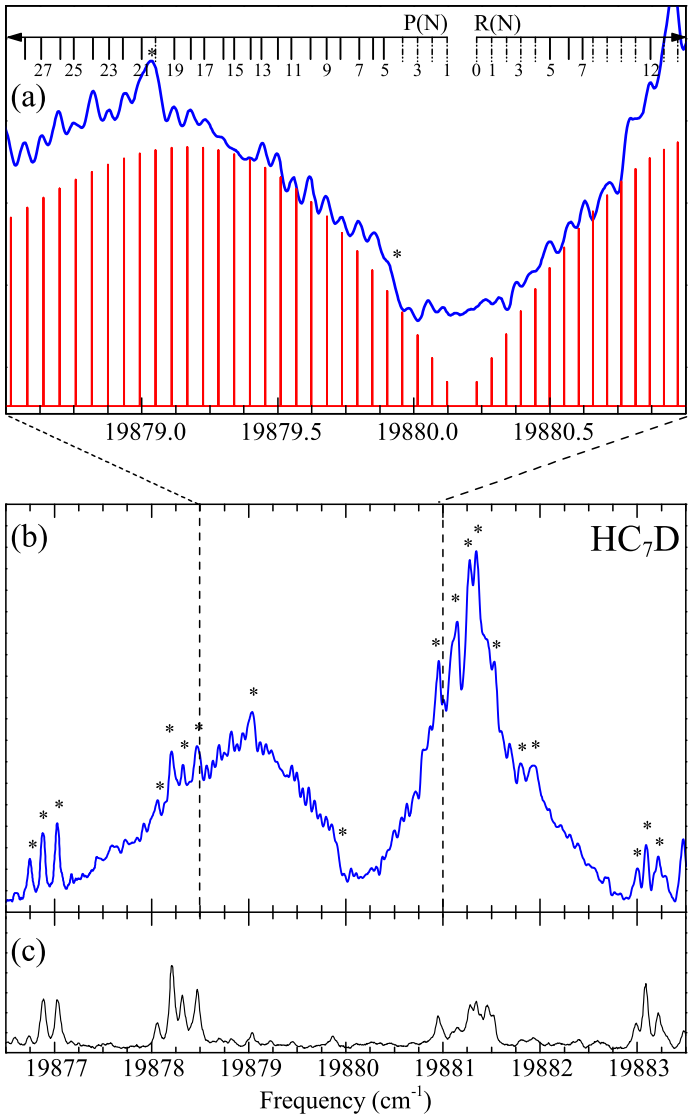

Figure 5.1 – (a) The expanded spectrum of the $\widetilde{A}^3\Sigma_u^- - \widetilde{X}^3\Sigma_g^-$ electronic transition of HC_7D (upper trace) in the band origin region compared with a simulated stick diagram using an effective ${}^1\Sigma - {}^1\Sigma$ Hamiltonian. The full spectrum is shown in panel (b). Peaks due to overlapping spectra originating from other species are marked by an asterisk and shown in panel (c) for expansion conditions not in favor of carbon chain formation.

are listed in Table 5.1. Fig. 5.1 shows the simulated stick diagram using these values. The simulation yields a rotational temperature of 26 K in the slit jet expansion. The resulting ground state rotational constant, $B_0'' = 0.027231$ cm^{-1}, is close to the calculated value of $B_e'' = 0.02706$ cm^{-1}. The origin band of the $\widetilde{A}^3\Sigma_u^- - \widetilde{X}^3\Sigma_g^-$ electronic transition of HC_7D at 19880.18(2) cm^{-1} is in agreement with the value reported in Ref. [150].

5.3.2 DC_7D

The $\widetilde{A}^3\Sigma_u^- - \widetilde{X}^3\Sigma_g^-$ origin band spectrum of DC_7D is shown in panel (a) of Fig. 5.2. As for HC_7D, the spectrum is blended by a number of overlapping narrow peaks that are reproduced for conditions of lower density and discharged current, not in favor of carbon chain formation, as shown in panel (b). The signal to noise ratio of the DC_7D spectrum is less than found for HC_7D, but some individual transitions can still be resolved. As stated before the effective spacing now amounts to about $4B$. The rotational analysis of the data is carried out following a similar procedure as described for HC_7D. In total 14 P-branch transitions and 7 R-branch transitions have been assigned. The resulting parameters from a least-squares fit are listed in Table 1. The value for the ground state rotational constant derived for DC_7D, $B_0'' = 0.026216$

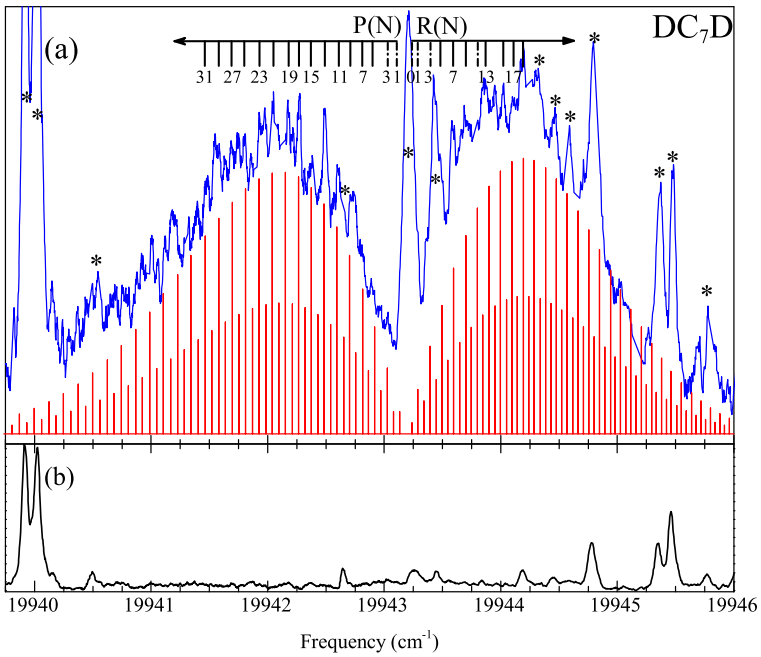

Figure 5.2 – (a) The observed rotationally resolved spectrum (blue) with simulated stick diagram (red) of the $\widetilde{A}^3\Sigma_u^- - \widetilde{X}^3\Sigma_g^-$ electronic transition of DC_7D. Peaks due to overlapping spectra originating from other species are marked by an asterisk and shown in panel (b) for expansion conditions not in favor of carbon chain formation.

Table 5.1 – Derived constants for the $\widetilde{A}^3\Sigma_u^- - \widetilde{X}^3\Sigma_g^-$ electronic origin bands of DC_7H and DC_7D, and a comparison with the iso-electronic species HC_6N, DC_6N and HC_7H. All values are in cm^{-1}.

	$\mathbf{HC_7D}$	$\mathbf{DC_7D}$	$\mathbf{HC_7H}$	$\mathbf{HC_6N}$	$\mathbf{DC_6N}$
T_{00} [a]	19880.177(2)[b]	19943.184(5)[b]	19817.895(4)[c]	19817.892(2)[e]	21208.60(5)[f]	21282.10(5)[f]
B_0''	0.027231(1)[b]	0.026216(2)[b]	0.028354(5)[c]	0.0283263(48)[e]	0.02806299(2)[f]	0.026982[f]
B_0'	0.027133(1)[b]	0.026112(9)[b]	0.028221(4)[c]	0.0282298(46)[e]	0.02792(5)[f]	0.02682(5)[f]
$D'' \times 10^8$	0.03435[d]	0.03435[d]	0.03435[d]	22.17(39)[e]	-	-
$D' \times 10^8$	0.03435[d]	0.03435[d]	0.03435[d]	28.12(36)[e]	-	-
B_0''/B_0'	1.0036	1.0039	1.0011	1.0034	1.0051	1.006

[a] The uncertainty in the band origin (T_{00}) represents the statistical error as obtained from the least squares fit. The absolute laser frequency can be determined with a precision of 0.02 cm^{-1}.
[b] This work.
[c] Derived from the remeasured spectrum in this work.
[d] Ref. [151].
[e] Ref. [108]. Effective constants only.
[f] Ref. [152].

cm^{-1}, is close to the calculated value of $B''_e = 0.02605$ cm^{-1}. Fig. 5.2 shows the simulated stick diagram of individual rotational transitions in P- and R-branch using the values listed in Table 1. Spin statistics are clearly involved now, making the transitions for even N twice stronger than those for odd N values. The origin band is found at 19943.18(2) cm^{-1}, very close to the value reported in Ref. [150]. From the observed spectrum we predict a rotational temperature of about 30 K. The ratios of B''_0/B'_0 for HC_7D and DC_7D amount to 1.0036 and 1.0039, respectively, and indicate that the overall chain length slightly increases upon electronic excitation. These values are comparable to the ratio found for HC_7H (1.0034), and are slightly smaller than found for DC_6N (1.0060) and HC_6N (1.0051) [108; 152]. In addition, the the spectrum of HC_7H is also re-measured with improved S/N level in the present work. With the remeasured spectrum, the molecular constants of HC_7H have been improved and the results are summarized in Table 5.1.

It is noticed that some weak additional features are observed in the experimental spectra of all the three species (HC_7H, HC_7D and DC_7D), particularly in the band origin regions where our spectra are not well resolved. This is a consequence of fine-structure effects, particularly prominent for transitions involving low rotational levels. For a $^3\Sigma$ electronic state, the spin-rotation constant, γ is usually very small compared to B and even for large N-values the resulting splitting of rotational levels will be difficult to resolve. The fine structure for the lowest J values is significantly correlated with the value of $\Delta\lambda = \lambda' - \lambda''$. Therefore, the typical observation is an interfering intensity pattern due to overlap of lower J rotational (small N) levels.

Such interference patters are clearly visible in Fig. 5.3, showing close-ups of the band origin region of HC_7D and DC_7D, as well as a remeasured spectrum of HC_7H. Here, the experimental resolution does not allow observing the fine structure even for the lowest J values, so determining the exact value of the spin-spin coupling constant is not possible. Assuming $\lambda'' \approx 0.36$ cm^{-1} (found for the iso-electronic HC_6N [151]), a tentative value of $\Delta\lambda \approx -0.17$ cm^{-1} is estimated from the consistency between simulated and observed spectra of the $\widetilde{A}^3\Sigma_u^- - \widetilde{X}^3\Sigma_g^-$ origin band spectra of HC_7H, HC_7D and DC_7D. The simulation is obtained by convolving a Lorentzian width of 0.02 cm^{-1}, corresponding to a non-radiative decay of ∼0.3 ns and a Gaussian width of 0.04 cm^{-1}, corresponding to the laser line width. This value of 0.3 ns for a non-radiative decay process differs from the indicative value of 0.1 ns reported by Ball et al. [150]. This longer lifetime better simulates the presently observed spectrum of somewhat higher quality. The resulting splittings and averaged overall spectra are indicated in Fig. 5.3 as well. Determining the actual values of λ'' and λ', however, requires a further improvement in experimental resolution.

Another possible explanation of the complex spectral structures in the band origin regions is the likely spectral overlapping with other weak vibronic hot bands of the same species. A recent infrared study [153] on the polyacetylenes $HC_{2n}H$ in a similar plasma expansion has shown that, although a low rotational temperature can be achieved, the mode-dependent vibrational temperatures of

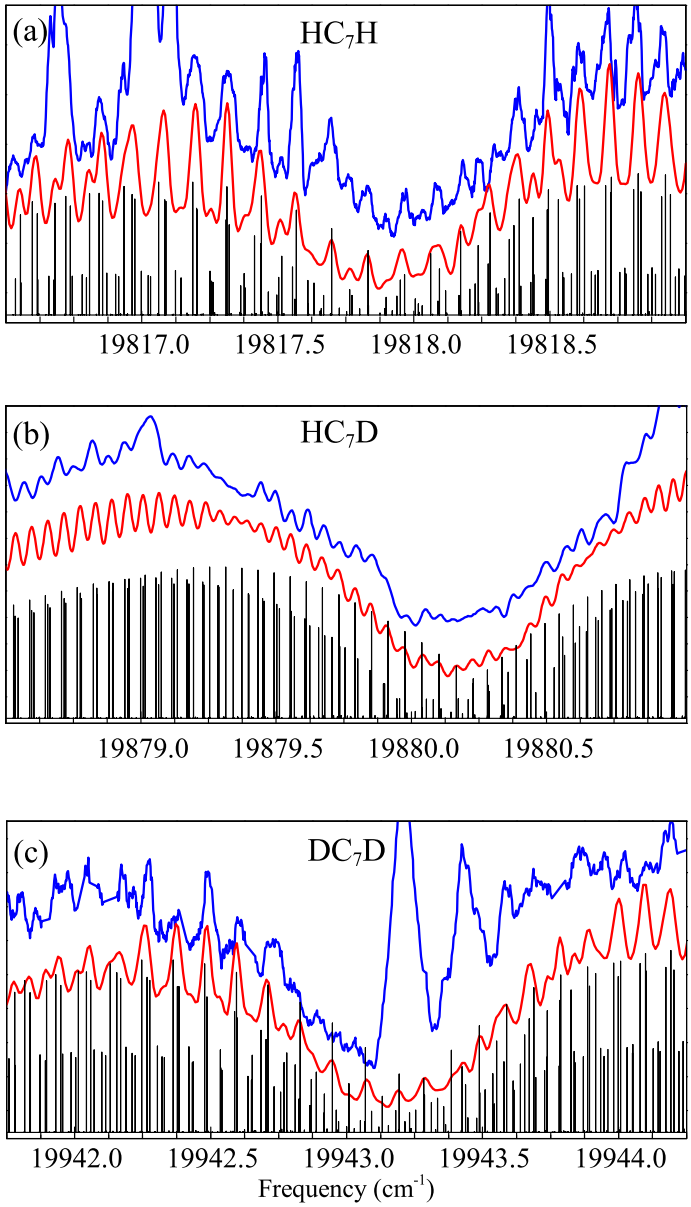

Figure 5.3 – Observed interfering intensity patterns (blue traces) at lower J rotational (small N) levels due to spin-spin splitting in ground and excited electronic states of HC_7H, HC_7D and DC_7D. The red traces show simulated spectra using a $^3\Sigma$-$^3\Sigma$ Hamiltonian with $\Delta\lambda \approx$ -0.17 cm^{-1} (for a Lorentzian line width of 0.02 cm^{-1} and a Gaussian line width of 0.04 cm^{-1}) and reproduce the observed interference patterns. The simulated stick diagrams are included.

HC_4H and HC_6H is found to be up to several hundred kelvin. However, without the knowledge of accurate ground-state spectroscopic parameters, the present experimental spectra do not allow to make a full analysis of these weak features.

Future high-resolution infrared measurements on the HC_7H ground state may improve the analysis of the present study.

5.4 Conclusion

The present spectroscopic study on HC_7D and DC_7D radicals marks the limit of what can be achieved in terms of resolving rotational manifolds of chains of carbon-based hydrocarbons of increasing length. Where the rotational structure of C_6H and C_6D radicals could be fully resolved in a setup with a generic pulsed cavity ring-down experiment combined with a slit-jet discharge expansion [107], for the present chains with 7 carbon atoms the rotational sequences become overlapped. This is in part due to the triplet electronic structure of ground and excited states, which particularly at low-N values tends to wash out the rotationally resolved manifolds. The presently observed spectra may be considered to be only incrementally improved with respect to those of a previous investigation [150]. However, the improvements are just sufficient to draw some conclusions for these molecules: rotational constants can be determined, the observed interferences in the spectra reveal indications of the spin structure in the $\widetilde{A}^3\Sigma_u^- - \widetilde{X}^3\Sigma_g^-$ electronic band system, while the simulations indicate that a possible non-radiationless decay of the excited state corresponds to a lifetime of 0.3 ns for HC_7D and DC_7D radicals.

CHAPTER 6

Rotationally resolved spectra of the 4051 Å comet band of C_3 for all six ^{12}C and ^{13}C isotopologues

Rotationally resolved absorption spectra of the $\widetilde{A}^1\Pi_u - \widetilde{X}^1\Sigma_g^+$ origin band of the tricarbon molecule (C_3) are reported for $^{12}C_3$ and its ^{13}C-substitued isotopologues. The 4051 Å electronic transition, also identified in cometary tails and in translucent interstellar clouds, has been measured using cavity ring-down spectroscopy and a supersonically expanding planar plasma. Previous spectroscopic studies of $^{12}C_3$ are extended and the electronic origin band is re-investigated including a perturbation analysis of the upper state. The rotational analysis of spectra originating from ^{13}C mono- and di-substituted C_3 yields accurate spectroscopic parameters for all six isotopologues, including ground state molecular constants for $^{13}C^{12}C^{13}C$ and $^{12}C^{13}C^{13}C$.

6.1 Introduction

The tricarbon molecule (C_3) is an important intermediate in many chemical processes involving hydrocarbons. As one of the simplest linear centrosymmetric poly-atomics with a low resistance to bending, C_3 serves as a benchmark molecule in quantum chemistry and molecular physics [154; 155]. The 4051 Å band of C_3 was first detected in cometary emission in 1881 [156] and later in the laboratory in 1942 [157]. In 1951 C_3 was unambiguously identified as the emitter of this band following a ^{13}C-substitution experiment [158]. Later, Gausset et al. [159; 160] assigned the spectrum as the $\widetilde{A}^1\Pi_u - \widetilde{X}^1\Sigma_g^+$ electronic origin band system based on a detailed rotational analysis of a number of vibronic bands. Due to the complexity of the spectrum, partly because of the existence of a low frequency bending mode, a large number of experimental and theoretical studies were needed to attain a comprehensive characterization of the $\widetilde{A}^1\Pi_u - \widetilde{X}^1\Sigma_g^+$ transition of C_3.

C_3 has also attracted long-term interest from astronomers because of its important role in the chemistry of the interstellar medium (ISM). This small molecule is potentially involved in the formation of more complex molecules such as carbon chains and carbonaceous circumstellar grains, and as a photofragment of polycyclic aromatic hydrocarbons (PAHs) [161; 162]. Different from most asymmetric carbon-chain species, C_3 cannot be detected in the interstellar medium by radio astronomy due to the lack of a permanent dipole moment. Detection of C_3 in circumstellar shells and in the dense ISM has been accomplished via ro-vibrational transitions in the mid- and far-infrared region [163; 13; 164; 145]. These detections prompted further high-resolution infrared laboratory studies [165–167] providing accurate molecular data for the electronic ground state.

The presence of C_3 in the diffuse ISM was first reported in 2001 [14], based on the detection of the 4051 Å band in the line of sight towards three reddened stars. Detection of C_3 in translucent clouds was then extended to several additional objects [168–171], all via the 4051 band. Recently, also a large set several vibronic bands of the $\widetilde{A}^1\Pi_u - \widetilde{X}^1\Sigma_g^+$ system have been observed in diffuse clouds towards three reddened stars [172]. Up to now C_3 is the largest carbon chain molecule unambiguously identified in the diffuse ISM.

Spectroscopic studies of the $\widetilde{A}^1\Pi_u - \widetilde{X}^1\Sigma_g^+$ system of C_3 have thus far focused on the main isotopologue, $^{12}C_3$ [159; 173–176]. Detailed laboratory investigations of the $\widetilde{A}^1\Pi_u - \widetilde{X}^1\Sigma_g^+$ $000 - 000$ band of $^{12}C_3$ have revealed a complex perturbation phenomenon in the origin band at 4051 Å. Several perturber lines in the $\widetilde{A}^1\Pi_u$ 000 state of $^{12}C_3$ were found in laboratory work by McCall et al. [173] and later explained in a perturbation model by Zhang et al. [174]. However, the recent observation of a high resolution spectrum towards HD 169454 indicates that this model still does not fully explain the astronomically observed line intensities in the origin band [172].

Only a few laboratory studies have been performed on ^{13}C-substituted C_3.

The first spectroscopic study was performed by Douglas in 1951, determining the position of six band heads of isotopologue transitions corresponding with the 4051 Å band [158]. In a subsequent study a tentative analysis of the rotationally resolved spectrum of pure $^{13}C_3$ was performed by Clusius and Douglas [177]. To our knowledge, no other spectroscopic work of the $\widetilde{A}^1\Pi_u - \widetilde{X}^1\Sigma_g^+$ electronic origin band system of $^{13}C_3$ has been reported. Other high-resolution studies of the fully ^{13}C substituted as well as mono-substituted $^{12}C^{12}C^{13}C$ and $^{12}C^{13}C^{12}C$ focused on vibrational transitions and have been performed in the mid-infrared region [178–180].

In this paper we present a systematic optical study of the 4051 Å band of all six isotopologues of C_3. The $\widetilde{A}^1\Pi_u - \widetilde{X}^1\Sigma_g^+$ $000-000$ band of $^{12}C_3$ is revisited, focusing on an experimental clarification of the rotational line intensities, and an extended Hamiltonian is presented to reproduce both transition frequencies and line intensities. High-resolution spectra of all five partially and fully ^{13}C substituted C_3 isotopologues are presented and analyzed, resulting in a set of molecular constants characterizing the $\widetilde{A}^1\Pi$ 000 upper electronic state. Moreover, for the ^{13}C di-substituted species also the ground state constants are presented for the first time.

6.2 Experimental

In the present work, jet-cooled C_3 radicals and ^{13}C-substituted isotopologues are produced in a supersonically expanding planar plasma by discharging a mixture of acetylene in helium and argon. Mixtures of 0.5% $^{12}C_2H_2$ and 0.2% $^{13}C_2H_2$ diluted in He/Ar $\sim 1:1$ gas are used to generate $^{12}C_3$ and $^{13}C_3$ radicals, respectively. To study the partially ^{13}C-substituted C_3 isotopologues, i.e., $^{13}C^{12}C^{12}C$, $^{13}C^{12}C^{13}C$, $^{12}C^{13}C^{12}C$ and $^{12}C^{13}C^{13}C$, two ($^{12}C_2H_2 + {}^{13}C_2H_2$)/He /Ar mixtures with a total acetylene concentration of $\sim$0.1%, and different $^{12}C : {}^{13}C$ isotope ratios of $\sim 2:1$ and $\sim 1:2$ are used. The gas mixture with a backing pressure of $\sim 5-9$ bar is supersonically expanded through a 30 mm $\times$ 300 μm slit discharge nozzle into a vacuum chamber, which is evacuated by a roots blower pump station (1000 m^3/h). A $\sim$300 μs negative high voltage pulse is applied to an expanding gas pulse, typically with $V/I \approx -500V/30$ mA. Further details of the experimental setup and the operation of the pulsed slit discharge are described in [107; 63].

The discharge nozzle is positioned in the vacuum chamber with its slit throat parallel to and $\sim$5 mm downstream from the optical axis of a high finesse cavity consisting of two high reflectivity mirrors (Layertec, reflectivity $\sim$99.91% at 405 nm). The optical cavity is used for cavity ring-down spectroscopy measurements. Tunable violet light at $\sim$405 nm is generated by frequency-doubling the near infrared output ($\sim$810 nm) of a Nd:YAG (532 nm) pumped pulsed dye laser (Sirah, Cobra-Stretch) in a DKDP crystal. Light leaking out of the cavity is detected by a photomultiplier tube to record the ring-down

decays. Typical ring-down times are $\sim 4-5$ μs. The experiment runs at a repetition rate of 8 Hz.

The non-linear scanning of the fundamental dye laser frequency is corrected by simultaneously recording the transmission fringes of two solid etalons (with free spectral ranges (FSR) ∼20.1 and 7.57 GHz, respectively). The absolute frequency of the experimental spectra is calibrated by the Ar I line [181] at 24656.8325 cm^{-1} recorded through the plasma. The frequencies of isolated rotational transitions in the spectra are determined from Gaussian fits, while the overlapping line envelopes, abundantly present in spectra of the mixed isotopologues, are deconvoluted to obtain the transition frequencies. A comparison of the ground state combination differences of four isotopologues ($^{12}C_3$, $^{13}C^{12}C^{12}C$, $^{12}C^{13}C^{12}C$ and $^{13}C_3$) available from previous mid-infrared data and our spectra, shows that the relative accuracy with which frequencies can be determined is better than 0.04 cm^{-1} for spectral lines.

From the measurements of the fringe profile of the high-finesse etalon (FSR ∼7.57 GHz), the bandwidth of the near infrared fundamental beam from the dye laser is estimated to be less than 0.03 cm^{-1}. The bandwidth of the violet light after frequency doubling is found to be ∼0.07 cm^{-1}, estimated from the width of the narrowest feature (FWHM) in the final experimental spectra. Since the laser bandwidth is larger than the Doppler width estimated at 0.03 cm^{-1} for C_3 for the used slit jet expansion conditions effects on the experimental intensity patterns are expected [173]. In brief, under such conditions, the resonant fraction within the laser bandwidth profile will exhibit a more rapid decay of the ring-down transient due to absorption, while the non-resonant fraction within the laser bandwidth profile will experience decays of an empty cavity without absorption. Overall, this phenomenon results in non-exponential decay transients of the ring-down signal. As a consequence the differences in decay transients cannot be straightforwardly interpreted in terms of optical depth, and the line intensities in the recorded CRDS spectra become (to some extent) unreliable. This effect is relatively small for weak absorptions but becomes pronounced in the case of strong absorptions [182]. Therefore, in the present work, the $\widetilde{A}^1\Pi_u - \widetilde{X}^1\Sigma_g^+$ origin band of $^{12}C_3$ has been recorded with two different sets of experimental conditions in order to interpret the line intensity pattern correctly: one was aimed at obtaining the best signal-to-noise ratio (S/N), and consequently the largest number of weak transitions; the other was aimed at obtaining the most reliable line intensities of the strong low-J transitions.

6.3 Results and Discussion

6.3.1 $^{12}C_3$

6.3.1.1 Rotational line intensities

The recorded absorption spectrum of $^{12}C_3$, shown in Fig. 6.1(a), has been recorded under plasma conditions as described in Ref. [107], i.e., ∼10 bar backing pressure and V/I ∼ -750 V/100 mA. The intensity pattern of this spectrum suffers significantly from the laser-bandwidth effect, similarly as in the spectra reported in Ref. [171]. An improved S/N in the present CRD experiment, though, makes it possible to observe more spectral features in the P-, Q- and R-branches. Many of the transitions in Fig. 6.1(a), which were assigned to perturbing states by Zhang et al. [174], show line intensities of almost equal magnitude compared to the regular (non-perturbed) transitions in the $\widetilde{A}^1\Pi_u - \widetilde{X}^1\Sigma_g^+$ system. Monitoring the ring-down decay signal during the spectral recordings, confirms that for most absorption lines in this region, the ring-down decays appear non-exponential [182].

As described above, the laser-bandwidth and non-exponential decay effects depend on the absorption depth and are considerably smaller for the weaker absorptions [182]. In order to achieve conditions guaranteeing reliable line intensities, it is necessary to control the C_3 radical density in the plasma, i.e., keeping the absorbance low, and therefore to reduce effects that lead to intensity anomalies. Similarly as in the study by McCall et al. [173], we recorded the spectra by confining the fit to the early part (34 μs) of each ring-down decay. This procedure, however, resulted in a comparable spectral pattern, but with a somewhat lower signal-to-noise ratio. Therefore we also varied the experimental settings for discharge power and precursor backing pressure. Fig. 6.1(b) shows the $^{12}C_3$ spectrum recorded for substantially different plasma conditions – V/I ∼ -400V/20 mA (estimated) and ∼7 bar backing pressure – approaching the threshold conditions for generating a stable plasma in our experiment. The spectrum has a different pattern from the one shown in Fig. 6.1(a). This method, through discharge control, seems be suitable for providing reliable estimates of the rotational line strengths. The resulting set of relative intensities for rotational line features, in part represented in the spectrum of Fig. 6.1(b), can be reliably compared with a recently observed absorption spectrum of C_3 in a diffuse translucent cloud towards HD 169454 [172]. The astronomically derived rotational temperature (∼21 K for low-J levels) is close to the actual rotational temperature in the supersonic jet in the present study.

The $^{12}C_3$ spectrum, shown in Fig. 6.1, comprises the main P, Q and R branches of the $\widetilde{A}^1\Pi_u - \widetilde{X}^1\Sigma_g^+$ $000-000$ band and isolated absorption features that are likely due to other transient hydrocarbons in the plasma. The latter are often found in plasma expansions, as several species are formed simultaneously [183; 108]. Some weak lines are due to ^{13}C mono-substituted C_3

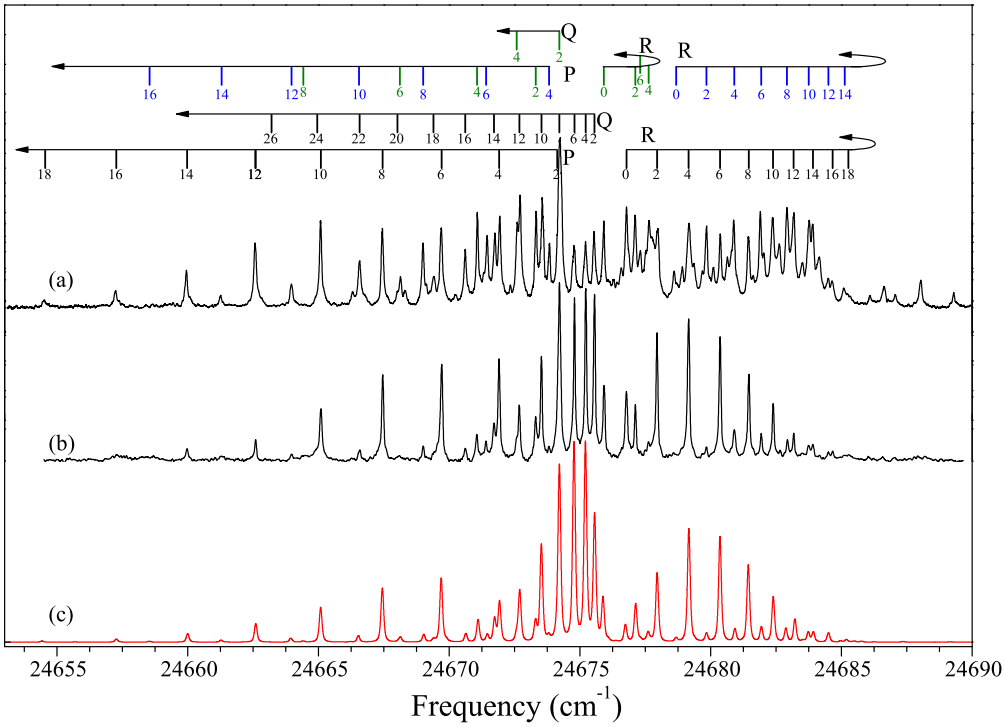

Figure 6.1 – Rotationally resolved spectra of the $\widetilde{A}^1\Pi_u - \widetilde{X}^1\Sigma_g^+$ electronic origin band of $^{12}C_3$. (a) Saturated spectrum recorded under high power discharge conditions preventing line saturation; (b) Spectrum recorded under controlled discharge conditions prohiting line saturation. (c) The red trace shows the simulated spectrum using the $^1\Pi_u - \widetilde{X}^1\Sigma_g^+$ Hamiltonian for a Lorentzian line width of 0.07 cm^{-1}, a Gaussian line width of ∼0.1 cm^{-1}, and with an estimated rotational of ∼35 K. Rotational transitions to perturber states $^3\Sigma_u^-$ and $P = 1$ states are indicated with blue and green lines, respectively.

isotopologues, observed in natural abundance, which is confirmed by the ^{13}C-substitution experiments that are discussed later.

6.3.1.2 The effective Hamiltonian for the $\widetilde{A}^1\Pi_u$ (000) state of $^{12}C_3$

Only transitions starting from *odd-J* levels in the ground state are observed for $^{12}C_3$, due to spin statistics. The line positions of the $\widetilde{A}^1\Pi_u - \widetilde{X}^1\Sigma_g^+$ 000 – 000 band of $^{12}C_3$ measured in this work are listed in Table 6.1. The transition frequencies agree well, i.e., within their experimental uncertainties with those previously reported by Tanabashi et al. and Zhang et al. [174; 175].

The $\widetilde{A}^1\Pi_u - \widetilde{X}^1\Sigma_g^+$ electronic origin band of $^{12}C_3$ was found to be perturbed by Gausset et al. [160]. A number of extra lines were observed in a high-resolution laboratory study by McCall et al. [173], and later these features were ascribed to two long-lived perturber states, based on a time-delayed laser-induced fluorescence study by Zhang et al. [174]. In Ref. [174], an effective

Table 6.1 – The frequencies and assignments of observed rotational lines in the $\widetilde{A}^1\Pi_u - \widetilde{X}^1\Sigma_g^+$ $000 - 000$ band and transitions to perturber states in the electronic spectrum of $^{12}C_3$, and residuals from the fit (see text).

		P-branch		**Q-branch**		**R-branch**	
J"	*Upper state*	*Obs.*	*o-c*	*Obs.*	*o-c*	*Obs.*	*o-c*
0	$\widetilde{A}^1\Pi_u$					24676.78	0.04
	$^3\Sigma_u^-$					24675.68	0.02
	$P = 1$					24678.92	0.04
2	$\widetilde{A}^1\Pi_u$	24674.13	-0.02	24675.56	-0.01	24677.95	-0.01
	$^3\Sigma_u^-$					24679.84	0.01
	$P = 1$	24673.31	0.01	24674.22	0.01	24677.12	-0.01
4	$\widetilde{A}^1\Pi_u$	24671.91	-0.02	24675.22	0.01	24679.16	-0.01
	$^3\Sigma_u^-$	24673.82	0.01			24680.9	-0.02
	$P = 1$	24671.06	-0.04	24672.58	0.00	24677.63	0.02
6	$\widetilde{A}^1\Pi_u$	24669.71	0.02	24674.79	0.01	24680.36	0.00
	$^3\Sigma_u^-$	24671.41	-0.05			24681.94	-0.01
	$P = 1$	24668.12	-0.02			24677.31	-0.01
8	$\widetilde{A}^1\Pi_u$	24667.46	0.01	24674.22	0.00	24681.46	0.02
	$^3\Sigma_u^-$	24669.01	-0.02			24682.91	0.03
	$P = 1$	24664.43	0.02				
10	$\widetilde{A}^1\Pi_u$	24665.09	0.01	24673.53	0.00	24682.39	0.00
	$^3\Sigma_u^-$	24666.55	0.02			24683.75	0.01
12	$\widetilde{A}^1\Pi_u$	24662.60	0.00	24672.68	-0.02	24683.18	-0.04
	$^3\Sigma_u^-$	24663.98	0.03			24684.51	0.00
14	$\widetilde{A}^1\Pi_u$	24659.98	-0.02	24671.72	-0.02	24683.92	0.01
	$^3\Sigma_u^-$	24661.30	0.02			24685.13	-0.05
16	$\widetilde{A}^1\Pi_u$	24657.27	0.01	24670.61	-0.02	24684.66*	0.18
	$^3\Sigma_u^-$	24658.54	0.01				
18	$\widetilde{A}^1\Pi_u$	24654.55*	0.15	24669.40	0.00	24685.27*	0.33
20	$\widetilde{A}^1\Pi_u$	24651.73*	0.30	24668.02	-0.02		
22	$\widetilde{A}^1\Pi_u$			24666.57	0.02		
24	$\widetilde{A}^1\Pi_u$			24664.95	0.02		
26	$\widetilde{A}^1\Pi_u$			24663.20	0.00		

* Transitions not included in the fit.

Hamiltonian was proposed for the upper $\widetilde{A}^1\Pi_u$ state including two perturbing states (a $^3\Sigma_u^-$ state, and a $P = 1$ vibronic state with regular P-type splittings) to reproduce all experimentally observed transition frequencies. Recent astronomical data and the new data presented here show a small mismatch with the calculated transition frequencies when using the Hamiltonian model given in Ref. [174]. Therefore, we introduce a similar Hamiltonian model as previously

Table 6.2 – Matrix for a perturbation analysis of the rotational level structure of the $\widetilde{A}^1\Pi_u$ state and its perturbing states for $^{12}C_3$.

	$\lvert\widetilde{A}^1\Pi_u, f/e\rangle$	$\lvert P=1, f/e\rangle$	$\lvert^3\Sigma_u^-, f/e\rangle$
$\langle\widetilde{A}^1\Pi_u, f/e\rvert$	$\mathbf{H}_\Pi$ [a]	a	$\zeta(\widehat{\mathbf{L}}\cdot\widehat{\mathbf{S}})$ [b]
$\langle P=1, f/e\rvert$		$\mathbf{H}_\Pi$ [a]	0
$\langle^3\Sigma_u^-, f/e\rvert$	Symmetric		$\mathbf{H}_\Sigma$ [c]

[a] The standard $\mathbf{H}_\Pi$ for $^1\Pi$ $P=1$ state is described by Eq. 6.1 in the text.
[b] This term is set to affect e levels only, and is to be understood in terms of single-electron operators [185].
[c] The standard $\mathbf{H}_\Sigma$ is expressed as $^3\Sigma_u^-$ [79]: $T_0 + B\mathbf{N}^2 + 2/3\lambda(3\mathbf{S}z^2 - \mathbf{S}^2) + \gamma(\mathbf{N}\cdot\mathbf{S})$

used but extended with matrix elements as given in Table 6.2. In this model, the Hamiltonian for the $\widetilde{A}^1\Pi_u$ state and $P=1$ perturber state is defined as given in the PGopher software [79]:

$$\mathbf{H}_\Pi = T_0 + (B \pm q/2)\widehat{\mathbf{N}}^2 - D\widehat{\mathbf{N}}^4 + H\widehat{\mathbf{N}}^6 \tag{6.1}$$

which results in the energy levels as:

$$\begin{aligned} E(J) = {} & T_0 + (B \pm q/2)[J(J+1) - K^2] - D[J(J+1) - K^2]^2 \\ & + H[J(J+1) - K^2]^3 \end{aligned} \tag{6.2}$$

where $K=1$ for the $\widetilde{A}^1\Pi_u$ and $P=1$ perturber state. The '+' and '–' before the parameter q, refer to the levels with e and f parity, respectively, opposite to the definition in Refs. [159], [174] and [175]. Moreover, it should be noted that the rotational term in Eq. (2) is expressed differently from the term used in Refs. [159; 174; 175], where

$$E(J) = T_0 + (B \pm q/2)J(J+1) - DJ^2(J+1)^2 + HJ^3(J+1)^3 \tag{6.3}$$

was used. The conversion factors between the molecular constants in Eq. (6.2) and (6.3) are available from Table 4 of Ref. [184].

We start our perturbation analysis using a similar Hamiltonian matrix as described in Ref. [174]. The Hamiltonian matrix as used in the PGopher software is given in Table 2. In the same way as in Ref. [174], we assume that the $P=1$ perturber state has a regular P-type splitting, described by a parameter q, while the spin-rotation interaction in the $^3\Sigma^-$ perturber state is neglected (γ fixed to 0). A least squares fit is made using PGopher software [79]

and the list in Table 6.1 as input with exclusion of the two Q(2) lines that cause large residuals. The fit results in a set of molecular parameters very similar to those given in Ref. [174], although the parameters for $K = 1$ states ($\widetilde{A}^1\Pi$ state and $P = 1$ perturber state) correspond to different definitions. To better describe the low-J levels in the upper $\widetilde{A}^1\Pi_u$ state, the effective Hamiltonian model is adapted as follows:

a) In Ref. [174], the spin-rotation interaction in the perturber $^3\Sigma^-$ state is neglected, and a significant spin-spin interaction ($\lambda_{ss} \sim -7$ cm^{-1}) results. Although the nature of this $^3\Sigma^-$ perturber state is still unclear, the large spin-spin interaction used here is difficult to explain, as it is more than four times larger than the spin-spin splitting in atomic carbon (1.5 cm^{-1}), and also largely differs from the values in the $\widetilde{a}^3\Pi$ and $\widetilde{b}^3\Pi$ states of C_3 [186], as well as that in the $\widetilde{b}^3\Sigma_g^-$ state of C_2. Based on these considerations, we decided to fix $\lambda_{ss} \sim -0.1$ cm^{-1} in our analysis, close to the previously reported values for triplet C_3 and C_2 [186; 187].

b) The spin-rotation interaction is considered to be significant, and is explicitly included in our fit. As discussed in Ref. [174], the $b^3\Sigma_u^-$ perturber may be a high vibronic level of the $\widetilde{a}^3\Pi$ or $\widetilde{b}^3\Pi$ state. In this case, as discussed in Ref. [188], the spin-splitting parameter γ depends on the magnitude of the Renner-Teller interaction relative to the spin-orbit interaction in the $^3\Pi$ state, with a value of $0 < \gamma < 2B$.

c) The e/f components in the $P = 1$ perturber state are treated separately, to account for possible additional perturbations not included in the Hamiltonian.

The perturbations in the $\widetilde{A}^1\Pi_u$ state of C_3 are more complex than described by the Hamiltonian model given in Table 6.2. Firstly, the origins of the $P = 1e$ and $P = 1f$ levels are found ∼0.65 cm^{-1} apart, likely because other dark states heterogeneously perturb the e and f components of the degenerated $\widetilde{A}^1\Pi_u$ and $P = 1$ states. The fluorescence lifetime measurements in Ref. [174] also show that there are at least three perturber states at the $J' = 1e$ level. Secondly, as discussed in Ref. [175], additional perturbations occurring for higher rotational levels at $J' \sim 20$ exhibit a different behavior in the e-component of the $\widetilde{A}^1\Pi_u$ state. The large deviations for the $J' = 17e$ and $19e$ levels in Table 6.1 indicate that the effective Hamiltonian in Table 6.2 cannot accurately reproduce the e level energies with $J' > 17$. Further, as shown in Table 6.3, the derived origin of the $\widetilde{A}^1\Pi_u$ state is still quite different from the value derived for high-J levels in Ref. [175]. Direct measurements of the dark perturber states as described in Ref. [26] and accurate measurements of the high-J' perturber lines are needed to perform a full deperturbation analysis of the upper $\widetilde{A}^1\Pi_u$ state of $^{12}C_3$.

Even though this Hamiltonian is only an approximation, it is well applicable to analyze astronomical spectra observed in cold diffuse translucent clouds, and to derive column densities of C_3 in individual rotational levels [172]. In the

Table 6.3 – Effective constants derived (in cm^{-1}) from a least-squares fit for the $\widetilde{A}^1\Pi_u(000) - \widetilde{X}^1\Sigma_g^+$ electronic origin band of $^{12}C_3$.

		This work[a]	Ref. [174]	Ref. [175]
$\widetilde{X}^1\Sigma_g^+$	B	0.4305883[b]		0.4305883(58)
	$D \times 10^6$	1.437 [b]		1.437(13)
	$H \times 10^{10}$	1.129 [b]		1.129(35)
$\widetilde{A}^1\Pi_u$	T_{00}	24675.489(14)	24675.632(80)[c]	24674.969(13)[d]
	B	0.412586(77)	0.41261(30)[c]	0.412632(23)[d]
	$D \times 10^6$	0.519 (fixed)	0.298 (fixed)	0.519(18)[d]
	$H \times 10^{11}$	5.35 (fixed)		5.35(43)[d]
	q	0.00023(16)	0.00125(59)[d]	0.0002906(16)[d]
$^3\Sigma_u^-$	T_{00}	24678.526(24)	24682.12(74)	
	B	0.42039(43)	0.4411(32)	
	$D \times 10^6$	1.0 (fixed)		
	λ	-0.1 (fixed)	-7.22	
	γ	0.6093(70)		
	ζ	0.661(29)	0.744(63)	
$P = 1e$	T_{00}	24675.783(29)	24675.68(14) [c]	
	B	0.3513(7)	0.3154(72)[c]	
	q		0.076(7)[d]	
	$a - e$	0.405(13)	0.436(60)	
$P = 1f$	T_{00}	24675.136(50)	-	
	B	0.3069(30)	-	
	q	-	-	
	$a - f$	0.461(32)	0.436(60)	
r.m.s		0.021	0.037	

[a] Numbers in the parenthesis are the one standard deviation of the fit.
[b] Ground state constants are taken from Ref. [175].
[c] Constants taken from Ref. [174]. These values are not converted (see text).
[d] Constants taken from Refs. [174] and [175] and converted (see text).

latter work, it was noticed that the intensities of the R(0) and P(2) lines are slightly overinterpreted. This is also visible from Fig. 6.1. There are two likely reasons for this. Firstly, as discussed above, additional perturbers which could be significant for the $J' = 1$ levels are not included. Secondly, the corresponding transition intensities, which depend on the state-mixing coefficients, are very sensitive to the parameters in the Hamiltonian model. The limited number of observed transitions to the $P = 1$ perturber state, prohibits a more accurate determination of these parameters.

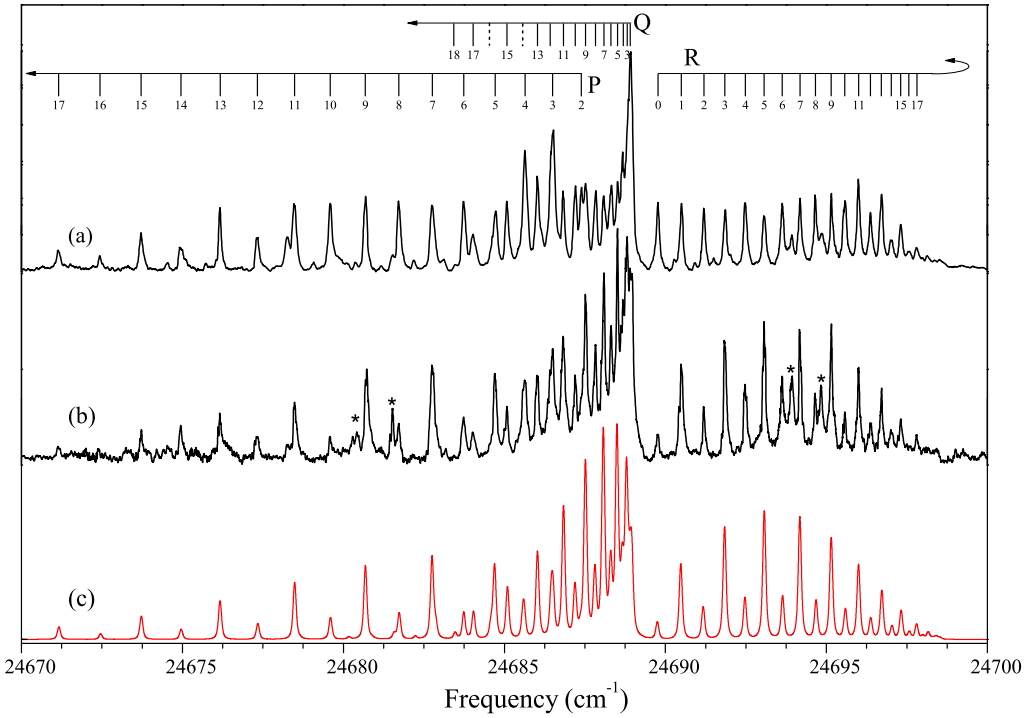

Figure 6.2 – Rotationally resolved spectra of the $\widetilde{A}^1\Pi_u - \widetilde{X}^1\Sigma_g^+$ electronic origin band of $^{13}C_3$. (a) Saturated spectrum recorded with ∼0.2% of $^{13}C_2H_2$ in the gas mixture; (b) Full line: Spectrum recorded with ∼0.03% of $^{13}C_2H_2$ in the gas mixture yielding reliable intensities. (c) The red trace shows the simulated spectrum for a $^1\Pi_u - \widetilde{X}^1\Sigma_g^+$ transition, with derived constants for $^{13}C_3$, a Lorentzian width of 0.07 cm^{-1}, a Gaussian width contribution of ∼0.1 cm^{-1}, with an estimated rotational temperature of $\sim 45K$. The lines marked with an asterisk are due to blending transitions of other small species like $^{13}C_3$ or ^{13}CH, etc.

6.3.2 $^{13}C_3$

Fig. 6.2 shows two recorded spectra of the $\widetilde{A}^1\Pi_u - \widetilde{X}^1\Sigma_g^+$ electronic origin band of $^{13}C_3$ near 4051 Å; in trace (a) a ∼0.2% $^{13}C_2H_2$ in He/Ar is used, in trace (b) a more diluted mixture with ∼0.03% $^{13}C_2H_2$ is used. While the two spectra exhibit a similar number of resolved transitions, trace (a) displays a better signal-to-noise ratio, whereas trace (b) exhibits more reliable line intensities as saturation effects can be excluded. Both spectra are used for line identification and for determining accurate transition frequencies, listed in Table 6.4, for rotational states up to $J' = 18$.

Different from the $^{12}C_3$ spectrum, in which only transitions from *even*-J'' are observed due to nuclear spin-statistics for $I(^{12}C)$=0, all J'' levels in the ground state of $^{13}C_3$ can be populated and the recorded spectra show transitions from both *even*– and *odd*-J'' levels. The nuclear spin of $I(^{13}C)$=1/2 determines a statistical weight of 1:3 for populations in *even*– and *odd*-J'' levels. This intensity alternation concerning two successive rotational lines is visible in

Fig. 6.2(b) although the intensity of some strong *odd-J* components is slightly affected by the laser-linewidth effect. In total 16 transitions in the P-branch, 14 transitions in the Q-branch and 18 transitions in the R-branch have been observed. The assignment and transition frequencies are listed in Table 6.4. The experimental values are further verified by comparing the ground state combination differences $R(J) - P(J+2)$ to those derived from previously reported accurate mid-infrared $^{13}C_3$ studies [179]. The maximum deviations do not exceed 0.04 cm^{-1} for J'' levels up to 17.

The emission data of the $\widetilde{A}^1\Pi_u - \widetilde{X}^1\Sigma_g^+$ electronic origin band of $^{13}C_3$ by Clusius and Douglas [177] add a large number of well-calibrated high-J lines to the data presented here for this band. Based on extrapolation of the molecular constants derived from the low-J levels in the CRD study, these well-resolved lines [177] are partially reassigned and subsequently included in a comprehensive analysis. It is found that the frequencies of the observed low-J transitions ($J'' < 17$) in Ref. [177] are consistent with the ones measured in the CRD spectrum when shifted ∼0.08 cm^{-1} to the blue. A consistent rotational assignment in the Q-branch is obtained upon changing the labeling of J to $J-1$ for each rotational line while the numbering of rotational lines in P- and R- branch is in agreement with our rotational assignment. The transition frequencies of the high J rotational lines presented in Ref. [177] are included (with reassignment where applicable) in Table 6.4 as well.

Table 6.4 – Transition frequencies of observed rotational lines in the $\widetilde{A}^1\Pi_u - \widetilde{X}^1\Sigma_g^+$ 000−band of $^{13}C_3$ and residuals from the fit. The frequencies of observed lines for $J > 17$ are taken from Ref. [177] and are used after shifting to the blue by 0.08 cm^{-1} and reassigning the transitions. All values are in (cm^{-1}).

J"	**P-branch**		**Q-branch**		**R-branch**	
	Obs.	*o-c*	*Obs.*	*o-c*	*Obs.*	*o-c*
0					24689.77	0.02
1					24690.49	0.01
2	24687.39	0.03	24688.91	0.02	24691.2	0.02
3	24686.5	0.00	24688.81	0.02	24691.85	0.01
4	24685.64	0.03	24688.69	0.04	24692.48	0.01
5	24684.71	0.02	24688.51	0.02	24693.07	0.00
6	24683.74	0.01	24688.31	0.02	24693.63	-0.01
7	24682.76	0.02	24688.09	0.02	24694.18	0.01
8	24681.72	-0.01	24687.83	0.02	24694.66	-0.02
9	24680.68	0.01	24687.52	0.01	24695.15	0.00
10	24679.59	0.00	24687.20	0.01	24695.57	-0.02
11	24678.48	0.00	24686.83	0.00	24696.00	-0.01
12	24677.33	-0.01	24686.42	-0.02	24696.37	-0.01

Continued on next page

Table 6.4 – continued from previous page

J"	**P-branch**		**Q-branch**		**R-branch**	
	Obs.	*o-c*	*Obs.*	*o-c*	*Obs.*	*o-c*
13	24676.17[b]	0.00	24686.03	0.01	24696.71	-0.02
14	24674.95	-0.01			24697.02	-0.03
15	24673.72	0.00	24685.08	-0.01	24697.31	-0.02
16	24672.44	-0.02			24697.56	-0.03
17	24671.15	-0.01	24684.03	-0.01	24697.81	-0.01
18			24683.43	-0.03		
19	24668.46[b]	-0.02	24682.84	-0.01		
20			24682.19	-0.03		
21	24665.66	-0.03	24681.55	-0.01		
22	24664.13[b]	-0.12	24680.87	-0.01		
23	24662.87[b]	0.08	24680.14	-0.02		
24	24661.23	-0.06	24679.41	-0.01		
25	24659.78	0.00	24678.61	-0.03		
26	24658.12[b]	-0.11	24677.81	-0.03		
27	24656.63	-0.03	24677.01	-0.01		
28	24655.05	-0.01	24676.17[b]	0.00		
29	24653.48	0.03	24675.28	-0.01		
30	24651.69[b]	-0.10	24674.37	-0.01		
31	24650.23[b]	0.10	24673.45	-0.01		
32	24648.39[b]	-0.04	24672.50	-0.01		
33	24646.69	-0.02	24671.53	0.00	24697.73	0.05
34			24670.52	-0.01		
35	24643.21	0.01	24669.51	0.00	24697.27	0.06
36	24641.46	0.04	24668.46[b]	0.00		
37	24639.62	0.01	24667.44	0.05	24696.68	0.03
38			24666.31	0.01		
39	24635.88	-0.05	24665.20	0.01	24696.02	0.02
40			24664.13[b]	0.07		
41	24632.18	0.01	24662.87[b]	-0.03	24695.25	-0.02
42			24661.74[b]	0.01		
43	24628.33	0.01	24660.55	0.01	24694.42	-0.04
44	24626.39[b]	0.02	24659.34	0.02		
45	24624.41	0.01	24658.12[b]	0.03	24693.57	-0.01
46			24656.77	-0.06		
47	24620.39	-0.02	24655.56	0.00	24692.56	-0.06

Continued on next page

Table 6.4 – continued from previous page

J"	**P-branch**		**Q-branch**		**R-branch**	
	Obs.	*o-c*	*Obs.*	*o-c*	*Obs.*	*o-c*
48			24654.25	-0.02		
49	24616.35	0.01	24652.97	0.00	24691.55	-0.04
50			24651.69[b]	0.05		
51	24612.21	0.01	24650.23[b]	-0.06	24690.47	-0.02
52			24648.92	-0.01		
53	24608.02	0.03	24647.51	-0.04		
54			24646.11	-0.04		
55			24644.71	-0.03		
57			24641.82	-0.04		
59			24638.87	-0.03		
61			24635.88[b]	0.00		
63			24632.75	-0.04		
65			24629.63	0.01		
67			24626.39[b]	0.02		
69			24623.10	0.05		

[b] Blended lines

The experimentally determined transition frequencies of the $^{13}C_3$ band are fitted in PGopher software [79] using a standard Hamiltonian for the $\widetilde{A}^1\Pi_u - \widetilde{X}^1\Sigma_g^+$ transition, where the rotational energy levels in the upper $\widetilde{A}^1\Pi$ state are represented by Eq. 6.1. The resulting molecular constants in the upper state fit are summarized in Table 6.6. The fit is carried out with the ground state constants B_0'', D'' and H'' fixed to the values reported in Ref. [179], and the band origin T_{00} and upper-state B_0', D', H' and q' set as variable parameters. Since the resolution of the photographed spectrum in Ref. [177] is $\sim$0.25 cm^{-1}, uncertainties in the transition frequencies are larger than in the present experiment. Therefore, the high rotational lines ($J'' > 17$) listed in Table 6.5 are used with lower statistical weight in the fit by a factor of 0.5 for unblended lines and 0.3 for blended lines. A simulated spectrum using the derived molecular constants in Table 6.6 is shown in Fig. 6.2(c) and compared to the experimental spectrum shown here.

A number of features are found in the experimental spectra (marked with an asterisk) in Fig. 6.2(b) which do not match assignments to $^{13}C_3$ transitions. These features are not observed in the $^{12}C_2H_2$/He/Ar plasma and thus must be due to some species containing ^{13}C. As strong perturber features are observed in the spectrum of $^{12}C_3$, we considered the possibility that these features are due to an analogous perturbation in the spectrum of $^{13}C_3$. However,

the deviations from the fit to a single unperturbed $^1\Pi_u - ^1\Sigma_g^+$ transition are found to be small, i.e., within their experimental uncertainties. Inspection of the observed deviations confirms that no significant perturbations for either e-parity or f-parity of high rotational levels (up to $J'' = 55$) occur in the upper $\widetilde{A}^1\Pi_u$ 000 state of $^{13}C_3$. As for the observed extra lines, no pairs are found to match to ground state combination differences $R(J) - P(J+2)$ of $^{13}C_3$. The assignment of the unidentified features to other C_3-isotopoluges (e.g. $^{12}C^{13}C^{13}C$), possibly due to a small ^{12}C impurity in the precursor gas, can be excluded since the strong Q-branches of the isotopologues are not seen in Fig. 6.2(b). Hence, the only logical explanation for the unidentified features at this stage is that these arise from (possibly ssivibrationally excited) small hydrocarbon radicals that are produced in the plasma, such as $^{13}C_2$ and ^{13}CH.

6.3.3 ^{13}C mono- and di-substituted C_3-isotopologues

The four partially ^{13}C-substituted $^{12}C^{13}C^{13}C$, $^{12}C^{13}C^{12}C$, $^{13}C^{12}C^{13}C$ and $^{13}C^{12}C^{12}C$ isotopologues of C_3 are systematically studied in the plasma expansion by discharging ($^{13}C_2H_2$ + $^{12}C_2H_2$)/He/Ar gas mixtures with a total acetylene concentration of ∼0.1%. It is important to realize that $^{12}C_3$ and $^{13}C_3$ are produced under such plasma conditions as well, therewith adding extra transitions, but these can be distinguished based on the detailed analysis presented in the previous two sections.

Fig. 6.3 shows two experimental spectra recorded with typical isotope ratios of ^{12}C:$^{13}C < 1$ and > 1. The spectra are very dense. Assignments of rotational lines to a specific isotopologue and the rotational analysis of the experimental spectrum are carried out using an effective Hamiltonian for a $^1\Pi_{(u)} - ^1\Sigma_{(g)}$ transition for each ^{13}C mono- and di-substituted isotopologues as follows:

a) The approximate band origins of the four isotopologues are estimated using the previously reported band head data. Considering that the $^1\Pi_u$ state of $^{12}C_3$ suffers from a strong perturbation, the isotopic shifts of the band heads with respect to $^{13}C_3$ are used instead. These have been reported in Ref. [158] to be ∼−11.0, -9.3, -3.9, -1.9 cm^{-1} for $^{13}C^{12}C^{12}C$, $^{13}C^{12}C^{13}C$, $^{12}C^{13}C^{12}C$ and $^{12}C^{13}C^{13}C$, respectively. Although not very precise, these values help to locate the band positions of the four isotopologues.

b) The rotational constants of the excited states of the four isotopologues are estimated by assuming that the B_0''/B_0' ratios for the $\widetilde{A}^1\Pi_u - \widetilde{X}^1\Sigma_g^+$ 000 − 000 band of all six C_3-isotopologues have comparable values, i.e. ∼1.043, as derived for both $^{12}C_3$ in Ref. [175] and $^{13}C_3$ in this work. Accurate values for ground state rotational constants for mono-substituted $^{13}C^{12}C^{12}C$ and $^{12}C^{13}C^{12}C$ are available from mid-infrared work [179; 180] and these parameters are used throughout our study. For the ^{13}C disubstituted $^{12}C^{13}C^{13}C$ and $^{13}C^{12}C^{13}C$ isotopologues, we assume cen-

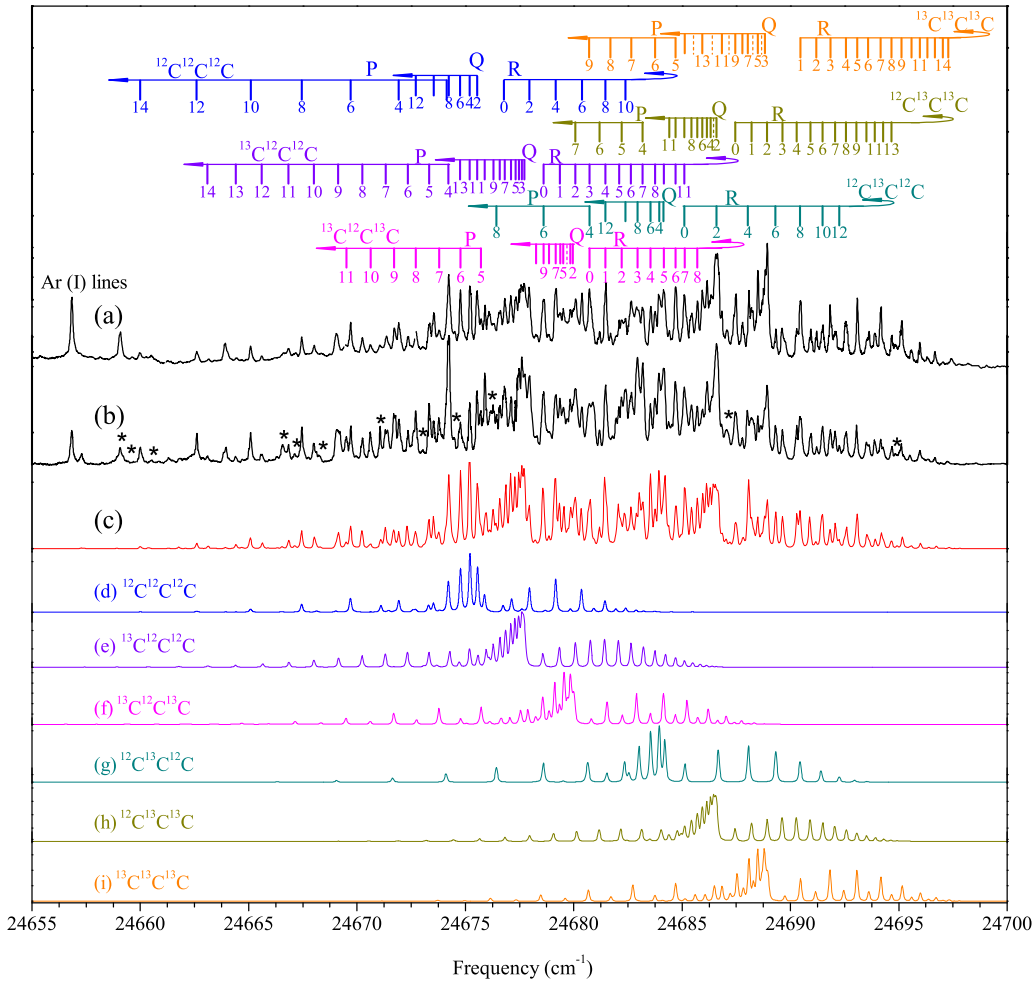

Figure 6.3 – The six blended spectra of the $\widetilde{A}^1\Pi_u - \widetilde{X}^1\Sigma_g^+ 000 - 000$ bands of the $^{12}C_3$ and ^{13}C-substituted C_3 radicals in a mixed ($^{13}C_2H_2 + {}^{12}C_2H_2$)/He/Ar plasma, with (a) the ratio of $^{12}C/^{13}C < 1$ and (b) of $^{12}C/^{13}C > 1$. The Ar(I) absorption line [181] has been used for absolute calibration of the recorded spectra. The red trace (c) shows a weighted sum of simulated spectra, based on simulated spectra for the individual isotopologues (shown in (d) to (i) traces), using a Lorentzian line width of 0.07 cm^{-1}, a Gaussian line width of 0.1 cm^{-1}, and a rotational temperature of ∼40 K. The P-, Q- and R-branches of the observed rotational lines for the isotopologues are indicated. The lines marked with an asterisk are due to blending transitions of other small species or unknown perturbation features.

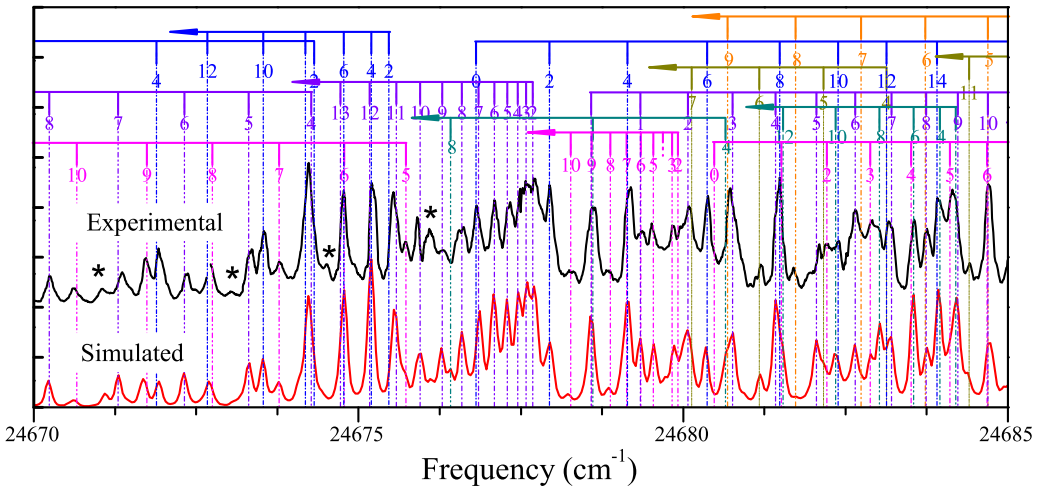

Figure 6.4 – A zoomed-in plot of Fig. 6.3. The black trace shows the observed spectrum through the mixed ($^{13}C_2H_2 + {}^{12}C_2H_2$)/He/Ar plasma, with ratio $^{12}C/^{13}C <$ 1 and the red trace shows the weighted sum of the simulated spectra (lower trace) using the estimated relative concentrations of all individual isotopologues. The P-, Q- and R-branch transitions are indicated using the calculated values. The lines marked with an asterisk are due to other small species or unknown perturbation features.

trifugal distortion constants for both lower and upper states similar to those of $^{13}C^{12}C^{12}C$ and $^{13}C^{13}C^{13}C$.

c) The intensity alternations for *even-* and *odd-J* transitions due to the statistical weight of exchangeable homo-nuclear atoms are used for the assignment of the spectra of ^{13}C mono- and di-substituted isotopologues. Specifically, two of the isotopologues, $^{12}C^{13}C^{12}C$ and $^{13}C^{12}C^{13}C$, are centro-symmetric linear molecules and their spectra will show intensity alternations. In the case of $^{12}C^{13}C^{12}C$ with two identical ^{12}C atoms with $I = 0$, only *even-J* transitions can be observed in the spectrum, while in the case of $^{13}C^{12}C^{13}C$ with two identical ^{13}C atoms with $I = 1/2$, an intensity alternation with a statistical weight of 1:3 for *even-* and *odd-J* transitions respectively, occurs.

In total, 35 transitions are assigned to $^{13}C^{12}C^{12}C$, 24 to $^{13}C^{12}C^{13}C$, 16 to $^{12}C^{13}C^{12}C$, and 27 to $^{12}C^{13}C^{13}C$. The transition frequencies are listed in Table 6.5. The rotational assignment for each transition is indicated in Fig. 6.3 for all isotopologues. A zoomed-in portion of the cumulative spectrum is shown in Fig. 6.4.

Table 6.5 – Transition frequencies of observed rotational lines in the $\widetilde{A}^1\Pi_u - \widetilde{X}^1\Sigma_g^+$ 000−band of ^{13}C mono- and di-substituted C_3-isotopologues. All values are in (cm^{-1}).

J"	**P-branch**		**Q-branch**		**R-branch**	
	Obs.	*o-c*	*Obs.*	*o-c*	*Obs.*	*o-c*
$^{13}C^{13}C^{12}C$:						
0					24687.46[b]	0.02
1					24688.21	0.01
2			24686.59[b]	0.04	24688.92	-0.01
3					24689.63	0.01
4	24683.18[b]	0.04	24686.31	0.00	24690.28	0.00
5	24682.21[b]	0.03	24686.15	0.01	24690.93	0.03
6	24681.19	0.01	24685.94[b]	-0.01	24691.48[b]	-0.02
7	24680.08[b]	-0.05	24685.70[b]	0.00	24692.06	0.01
8			24685.43[b]	0.01	24692.56[b]	-0.02
9			24685.11[b]	-0.01	24693.05[b]	0.01
10			24684.70[b]	-0.07	24693.50	-0.01
11			24684.41	0.02	24693.89	-0.04
12					24694.28	-0.02
13					24694.67[b]	0.03
$^{12}C^{13}C^{12}C$:						
0					24685.11[b]	-0.02
2			24684.14[b]	-0.04	24686.59[b]	-0.08
4	24680.70[b]	0.07	24683.94	-0.01	24688.04[b]	-0.03
6	24678.60[b]	0.01	24683.55[b]	0.01	24689.31	-0.02
8	24676.44	0.02	24682.94[b]	-0.07	24690.45[b]	0.02
10			24682.38[b]	0.04	24691.48[b]	0.06
12			24681.47[b]	-0.07	24692.26	0.00
$^{13}C^{12}C^{13}C$:						
0					24680.73[b]	-0.08
1					24681.47[b]	-0.04
2			24679.96	0.02	24682.21[b]	0.03
3			24679.85	0.00	24682.94[b]	0.06
4					24683.55	0.04
5	24675.72	-0.01	24679.52	-0.03	24684.15[b]	0.04
6	24674.77[b]	-0.01	24679.37[b]	0.02	24684.70	0.02

Continued on next page

Table 6.5 – continued from previous page

J"	**P-branch**		**Q-branch**		**R-branch**	
	Obs.	*o-c*	*Obs.*	*o-c*	*Obs.*	*o-c*
7	24673.79[b]	0.01	24679.17[b]	0.05	24685.12[b]	-0.1
8	24672.72	-0.03	24678.85	-0.01	24685.70[b]	-0.03
9	24671.71[b]	-0.02	24678.60[b]	0.03		
10	24670.62	-0.02	24678.27	0.04		
11	24669.50	-0.03				
^{12}C^{12}C^{13}C:						
0					24678.6[b]	0.02
1					24679.36[b]	0.03
2			24677.72	0.03	24680.08[b]	0.01
3			24677.6	0.02	24680.73[b]	-0.03
4	24674.22[b]	-0.04	24677.47	0.02	24681.47[b]	0.05
5	24673.33	0.03	24677.31	0.02	24682.09	0.04
6	24672.35	0.03	24677.10[b]	0.01	24682.64[b]	-0.01
7	24671.33	0.03	24676.81[b]	-0.04	24683.18[b]	-0.03
8	24670.25	0.01	24676.59	0.00	24683.75[b]	0.01
9	24669.13	-0.00	24676.29	0.00	24684.15[b]	-0.08
10	24668.01	0.01	24675.90	-0.05	24684.70[b]	0.01
11	24666.83	-0.02	24675.54[b]	-0.04	24685.11[b]	0.01
12	24665.60	-0.04	24675.20[b]	0.03		
13	24664.40	-0.01	24674.76[b]	0.04		
14	24663.10	-0.01				

[b]: Blended lines

Least-squares fits are performed based on the experimental transition frequencies for each of the isotopologues, where the frequencies of blended lines are included with a lower statistical weight in the fits. Similar as for $^{13}C_3$, a standard $^1\Pi_u - ^1\Sigma_g^+$ Hamiltonian is used for all the four partially substituted isotopologues. For the mono-substituted $^{13}C^{12}C^{12}C$ and $^{12}C^{13}C^{12}C$, the band origins T_{00} and upper-state constants B_0' and D' are set as variable parameters while the ground state constants B_0'', D'' are fixed to the values available from previous mid-infrared work [179; 180]. Considering that only a limited number of low-J transitions are observed in our spectra, this does not allow for determining Λ-type doubling constants q' and centrifugal distortion constants D'; values for D' and q' are therefore kept fixed in the fits in which D' has been estimated from the D''/D' ratio of $^{12}C_3$ [175] and q' is fixed at 0.

For the disubstituted $^{13}C^{12}C^{13}C$ and $^{12}C^{13}C^{13}C$, for which no ground state constants are available, the centrifugal distortion constants are fixed to those of $^{13}C^{13}C^{13}C$ and $^{13}C^{12}C^{12}C$. The ground state and upper state rotational constants B'' and B' and the band origins T_{00} follow from the fit.

The resulting spectroscopic constants are summarized in Table 6.6. A simulated sum spectrum, Fig. 6.3(c) and simulated individual spectra for each isotopologue (Fig. 6.3 (d)-(i)) using the parameters given in Table 6.6, are shown and compared to the experimental spectrum. The simulated spectra shown in Fig. 6.3 (and Fig. 6.4) take into account the statistical abundance and estimated concentration of each C_3 isotopologue produced in the plasma. A few weak features are observed, marked by asterisks in Figs. 6.3 and 6.4 that could not be assigned to any C_3-isotopologues and are likely due to other small hydrocarbon radicals.

For the four centro-symmetric C_3 isotopologues ($^{12}C^{12}C^{12}C$, $^{12}C^{13}C^{12}C$, $^{13}C^{12}C^{13}C$ and $^{13}C^{13}C^{13}C$) the derived rotational constants can be used to estimate the values of the effective CC bond lengths, assuming that for such a geometry the two bonds are identical for each configuration. Such procedure yields consistent values of effective bond lengths for all the four isotopologues: 1.277(2) Å in the $\widetilde{X}^1\Sigma_g^+$ (000) state, and 1.303(3) Å in the $\widetilde{A}^1\Pi_u$ (000) state. The two values are also found to reasonably reproduce the rotational constants (B_0'', B_0') of the other two isotopologues ($^{12}C^{12}C^{13}C$ and $^{12}C^{13}C^{13}C$) as listed in Table 6, with deviations less than 0.1%. The present data do not allow to derive more accurate values. A direct comparison of the experimental values with theoretical equilibrium values is challenging, given the highly flat character of the potential surface in the ground state [154] and the double-minimum asymmetric stretching potential surface in the $\widetilde{A}^1\Pi_u$ state [154; 189]. In parallel, the multiple and severe perturbations in the $\widetilde{A}^1\Pi_u$ state of $^{12}C_3$ should also be taken into account. Therefore, more and more precise measurements are needed to derive highly accurate molecular geometries from this type of data.

6.4 Conclusion

In the present study high resolution spectra are presented for the $\widetilde{A}^1\Pi_u - \widetilde{X}^1\Sigma_g^+$ $000 - 000$ band of all six ^{12}C and ^{13}C containing isotopologues of the C_3 molecule. Pure spectra have been recorded for $^{12}C_3$ and $^{13}C_3$ and partially overlapping spectra of the mixed isotopologues have been unraveled. Molecular constants for the $\widetilde{A}^1\Pi_u$ excited state have been determined. For $^{13}C^{12}C^{13}C$ and $^{12}C^{13}C^{13}C$ also the ground state constants have been determined for the first time.

The perturbation in $^{12}C_3$ has been analyzed thoroughly in Ref. [174] and [175]. In the present work we have adapted the effective Hamiltonian model describing the $\widetilde{A}^1\Pi_u - \widetilde{X}^1\Sigma_g^+$ $000 - 000$ band of $^{12}C_3$, specifically to interpret recent astronomical observations of interstellar C_3 [172] Despite the fact that our model does not work well for high-J transitions, it can be used to reproduce

Table 6.6 – Spectroscopic parameters for the ^{13}C-substituted isotopologues of C_3.[a]

		$^{12}C^{12}C^{13}C$	$^{13}C^{12}C^{13}C$	$^{12}C^{13}C^{12}C$	$^{12}C^{13}C^{13}C$	$^{13}C^{13}C^{13}C$
$\widetilde{A}^1\Pi$	T_{00}	24677.7849(53)[a]	24680.0460(63)[a]	24684.3048(93)[a]	24686.6433(69)[a]	24688.9812(46)[a]
	B'	0.39718(52)	0.38179(71)	0.4123(10)	0.39734(65)	0.3808954(20)
	$D' \times 10^6$	0.504[b]	0.440[b]	0.470[b]	0.504[b]	0.394(8)
	$H' \times 10^{11}$	–	–	–	–	5.090(17)
	$q' \times 10^4$	–	–	–	–	2.525(41)
$\widetilde{X}^1\Sigma^+$	B''	0.413743[c]	0.39832(86)	0.430276[d]	0.4143(12)	0.397024[c]
	$D'' \times 10^6$	1.398[b]	1.220[d]	1.30[c]	1.398[f]	1.220[b]
	$H'' \times 10^{10}$					1.05[b]
	B''/B'	1.042	1.043	1.043	1.042	1.043

[a] Numbers in the parenthesis represent one standard deviation of the fit. For The band origin (T_{00}), the absolute frequency can be determined with a precision of 0.04 cm^{-1} in the present work.
[b] Estimated from the ratio of D''/D' in $^{12}C_3$
[c] Values taken from Ref. [179] and fixed.
[d] Values taken from Ref. [180] and fixed.
[e] Estimated from $^{13}C^{13}C^{13}C$.
[f] Estimated from $^{12}C^{12}C^{13}C$.

line positions and intensities of low-J transitions of $^{12}C_3$ reasonably well, with inclusion of Q(2) lines. In contrast to $^{12}C_3$, no perturbation is found for $^{13}C_3$ in the $\widetilde{A}^1\Pi_u$ 000 state even up to very high J-levels, including data of Clusius and Douglas [177]. This results in accurate effective constants in the $\widetilde{A}^1\Pi_u$ state of $^{13}C_3$. Also for the $\widetilde{A}^1\Pi_u$ state of ^{13}C-mono and di-substituted isotopologues no clear evidence for perturbations are found.

C_3 is the largest carbon chain species identified so far in the diffuse interstellar medium. The astronomical detection of a ^{13}C-substituted isotopologue (and resulting isotope ratio) therefore may be useful as a diagnostic tool to monitor the physical and chemical processes taking place in the diffuse interstellar medium, similarly to previous studies on CH^+ and CN [190–192]. The corresponding overlap with the main isotopologue, and the relative intensities reflect the natural abundances. An unambiguous identification will become only possible for observations with sufficient resolution to distinguish the individual species. We have compared the simulated spectra of two ^{13}C mono-substituted isotopologues, i.e., the spectra shown in Figs. 6.3(e) and 6.3(g), to the astronomical spectra towards HD 169454 as presented in Ref. [172] and this does not provide convincing evidence for a positive identification of $^{13}C^{12}C^{12}C$ and $^{12}C^{13}C^{12}C$. Higher resolution will be needed to realize this.

Acknowledgments

We are indebted to Prof. Thomas Giesen (Cologne/Kassel) for generously providing us with spectroscopic constants of several C_3 isotopologues, prior to publication. We furthermore acknowledge financial support by FOM and NOVA. This work has been performed as part of ongoing research within the Dutch Astrochemistry Network.

CHAPTER 7

The $^2\Pi - \widetilde{X}^2\Pi$ electronic spectra of long carbon-chain $^{(13)}C_{2n}H/D$ molecules for $(n = 4 - 6)$

Unresolved $^2\Pi - \widetilde{X}^2\Pi$ electronic origin band transitions have been measured for the even numbered linear carbon chain radicals $^{(13)}C_{2n}H/D$ with $n = 4-6$. Spectra of the fully ^{13}C substituted $^{13}C_8H/D$ and $^{13}C_{10}H/D$ isotopologues are presented for the first time. $^{12}C_{10}H/D$ and $^{12}C_{12}H/D$ spectra are presented with improved S/N to realize a systematic study of the band profiles. Despite the fact that individual rotational transitions cannot be resolved, it is possible to derive effective values for the upper state lifetime. The obtained natural lifetime line broadening parameters of 0.8 ± 0.1 cm^{-1} for $n = 4$, 4.0 ± 0.5 cm^{-1} for $n = 5$, and 4.8 ± 0.5 cm^{-1} for $n = 6$ indicate that internal conversion processes occur in these carbon chain molecules for $n > 3$.

7.1 Introduction

Highly unsaturated hydrocarbons of the form C_nH have proven important intermediates in the chemistry of the interstellar medium (ISM). Their large dipole moment makes them ideally suited to search for in dark clouds by radio astronomy and positive identifications have been reported for C_3H [118], C_4H [193], C_5H [100], C_6H [194], C_7H [98] and C_8H [195; 196; 97]. Also the chemically related anionic species, C_4H^- [197], C_6H^- [198] and C_8H^- [196; 199] have been detected in space. In the laboratory spectra of substantially longer chains have been studied. Using Fourier-transform microwave spectroscopy accurate rotational ground state constants have been derived for chains as long as $C_{14}H$ [200–202]. Also in the optical domain strong electronic spectra of even $C_{2n}H$ and odd $C_{2n+1}H$ chains have been reported, using a variety of different spectroscopic techniques, both matrix based [203] and in the gas phase, such as cavity ring-down spectroscopy (CRDS), resonance-enhanced multi-photon ionization (REMPI-TOF) and incoherent broad band cavity enhanced spectroscopy (IBBCEAS). See for example Refs. [59; 204]. A fully resolved rotational spectrum has been reported for the two spin-orbit components of the $^2\Pi - \widetilde{X}^2\Pi$ electronic origin band system of C_6H and C_6D [113] that was reinterpreted recently in terms of an extensive Renner-Teller analysis [107]. In contrast, no rotationally resolved spectra have been recorded for the $^2\Pi - \widetilde{X}^2\Pi$ electronic origin band transition of C_8H (C_8D) and $C_{10}H$ ($C_{10}D$) [205]. Even in a cw-CRDS experiment [206] with a laser bandwidth far below the expected rotational spacing between adjacent C_8H rotational lines, only unresolved P- and R-branch envelopes were found and a lifetime of ∼7 ps was derived for the $^2\Pi_{3/2}$ upper electronic state to explain this observation. Also, in contrast to C_6H, only the contour of one P- and R-branch system could be observed for C_8H. This is likely because of spectral overlap of the $\Pi_{3/2} - \widetilde{X}^2\Pi_{3/2}$ and $\Pi_{1/2} - \widetilde{X}^2\Pi_{1/2}$ spin-orbit bands (i.e., $|A'' - A'| \sim 0$) in combination with a low population density in the $\widetilde{X}^2\Pi_{1/2}$ upper spin-orbit state. For $C_{10}H$ ($C_{10}D$) and $C_{12}H$ ($C_{12}D$) even no separate P- and R-branches were found. Instead, the bands published so far [207; 91] exhibit rather broad and largely unstructured profiles.

Spectroscopic studies of the $^2\Pi - \widetilde{X}^2\Pi$ system of $C_{2n}H$ radicals have thus far focused on the main and their D-substituted isotopologues; no work on the ^{13}C fully substituted analogues has been reported. In this contribution we present for the first time the $^2\Pi - \widetilde{X}^2\Pi$ electronic origin band gas-phase spectra of $^{13}C_8H$, $^{13}C_8D$, $^{13}C_{10}H$ and $^{13}C_{10}D$. Moreover, systematic studies of spectra recorded for different rotational temperatures, allow us to determine excited state lifetimes for the $C_{2n}H$ long chain molecules and their isotopologues in this series for $n = 4 - 6$.

7.2 Experimental

Pulsed cavity ring-down (CRD) spectroscopy is used to record direct absorption spectra of the $C_{2n}H$ chains through a supersonically expanding hydrocarbon plasma. High pressure mixtures (∼10 bar) of 0.5% $^{12}C_2H_2$, 0.2% $^{12}C_2D_2$ and 0.2% $^{13}C_2H_2$ diluted in He/Ar ∼1 : 1 gas are discharged in the throat of a modified pinhole nozzle [109; 183] to generate $^{(12/13)}C_{2n}H/C_{2n}D$ radicals, in a circular expansion. A regular vacuum (0.05 mbar during plasma operation) is maintained by a roots blower pump (1000 m^3/h). A ∼300 μs negative high voltage pulse is applied to the (500 μs long) expanding gas pulse, typically with V/I ≈ -1kV/100 mA. The distance of the pinhole nozzle orifice to the optical cavity axis can be varied during jet operation from a few millimeters up to several millimeters which allows to record spectra at different rotational temperatures.

Tunable light at around ∼625, ∼714 and ∼800 nm is generated by a pulsed dye laser (Sirah, Cobra Stretch) with Rhodamine 101, Pyridine 2 and Styryl 11, respectively, pumped by a frequency-doubled Nd:YAG laser (532 nm). The pulsed dye laser system is operated at an 8 Hz repetition rate with a pulse width of ∼6 ns and a bandwidth narrower than 0.05 cm^{-1}. The best achievable resolution – also taking into account residual Doppler broadening in the pinhole expansion – yields an upper limit ∼0.12 cm^{-1}, i.e., far more than a typical $2B$ value for the chains studied here.

A cavity ring-down event is initiated by injecting laser light into a high-finesse optical cavity, consisting of two highly reflective plano-concave mirrors, positioned 58 cm apart, that are mounted on high precision alignment tools and located on opposite sides of a high vacuum chamber. The light leaking out of the cavity is detected by a photomultiplier tube to record the ring-down decays. Non-linear scanning of the laser frequency is corrected by simultaneously recording the transmission fringes of two solid etalons (with free spectral ranges (FSR) ∼20.1 and 7.57 GHz). In the case of $^{(12/13)}C_8H/D$ (around 625 nm) an absolute laser frequency calibration is achieved by simultaneously recording an iodine reference spectrum with a precision better than 0.02 cm^{-1}. The $C_{10}H$ and $C_{12}H$ chains absorb around 714 and 800 nm, where iodine only weakly absorbs. Here, an absolute calibration is derived from resolved ro-vibrational C_2 transitions that are recorded simultaneously and that originate from the Philips and Swan band systems [208; 209].

7.3 Results

7.3.1 C_8H, C_8D, $^{13}C_8H$, and $^{13}C_8D$

In Fig. 7.1 overview spectra are shown for the $^2\Pi - \widetilde{X}\,^2\Pi$ electronic transitions of C_8H (upper trace), $^{13}C_8H$ (middle trace) and C_8D (lower trace). The $^{13}C_8H$ band, which has not been reported before, is located at 15975.1 cm^{-1}, ∼2 cm^{-1} blue shifted with respect to the band found for C_8H. The spectra comprise of

unresolved P- and R-branches, originating from the lower $\Pi_{3/2} - \widetilde{X}^2\Pi_{3/2}$ and the higher $\Pi_{1/2} - \widetilde{X}^2\Pi_{1/2}$ spin-orbit transitions. The C_8H and C_8D spectra are found at very similar positions as reported in Ref. [205], i.e., overlapping within experimental uncertainties. Also other previously observed features, such as a weak component a few cm^{-1} towards higher energy, are reproduced. This is shown in detail in the insets (b) to (d) in Fig. 7.1.

The $^{13}C_8H$ spectrum shows several similarities with the C_8H and C_8D spectra. A weaker feature near $\sim$15993 cm^{-1} (Fig. 7.1(c)) is the equivalent of the bands shown in (b) and (d); this absorption peak has a similar shift with respect to the main spectrum as found for these two bands. However, the band at $\sim$16006 cm^{-1}, shown in Fig. 7.1(a) has no direct equivalent in the ^{12}C-spectra. Fig. 7.1(a) shows that this feature has a profile that is very similar to the origin band spectra of C_8H, C_8D, and $^{13}C_8H$. The spectrum is $\sim$2 cm^{-1} blue shifted w.r.t. C_8D, i.e., similar to the value found for C_8H and $^{13}C_8H$. Therefore, its appearance is fully consistent with an assignment to $^{13}C_8D$, although this is not a priori expected from the used precursor species. As a $^{13}C_2H_2$/He/Ar mixture is used, an assignment to $^{13}C_8D$ only can be explained with a remaining pollution in the gas bottle with deuterated acetylene used in an earlier experiment, or by a D-enrichment in the $^{13}C_2H_2$ precursor gas. This has been checked by Fourier transform infrared spectroscopy of the used precursor gas sample, confirming that indeed the sample contains a few percent (i.e., more than natural abundance) of $^{12}C_2D_2$. The origin of the weaker bands positioned at $\sim$15991 cm^{-1}(for C_8H) and $\sim$16020 cm^{-1} (for C_8D) has been discussed in Ref. [205]. As stated before, it is likely that the strong band system around 15973.5 cm^{-1} comprises both the $^2\Pi_{3/2} - \widetilde{X}^2\Pi_{3/2}$ and $^2\Pi_{1/2} - \widetilde{X}^2\Pi_{1/2}$ bands, with the latter one much less populated for the low temperatures in the jet expansion. This leaves the weaker bands as to originate from a low energetic vibrational mode.

Several spectra have been recorded by changing the distance between nozzle orifice and optical axis of the cavity. This allows to vary the rotational temperature in a range from $\sim$5 to $\sim$40 K. The resulting spectra, are analyzed by contour fitting using a standard Hamiltonian for a $^2\Pi - \widetilde{X}^2\Pi$ transition by PGopher software [79]. Separate fits are performed for C_8H, C_8D and for $^{13}C_8H$ to derive the optimum values of parameters and minimal fit residuals. The ground state parameters B'' and A'' of C_8H are fixed to available microwave data [200; 202] and the excited state constant B', band origin T_{00} as well as Lorentzian line widths Γ and temperature T_{rot} are varied to reproduce the spectral profiles.

For C_8D and $^{13}C_8H$, for which accurate ground state parameters are not available from microwave data, the rotational constants are fixed to calculated values, while the value of A'' is kept the same as for C_8H. We performed a calculation at the B3LYP/3-21G* level using the GAUSSIAN 98 Software [140], yielding values of $B''_e = 0.019617$ cm^{-1} (for C_8H), $B''_e = 0.018961$ cm^{-1} (for C_8D) and $B''_e = 0.018153$ cm^{-1} (for $^{13}C_8H$). The calculated value of B''_e for

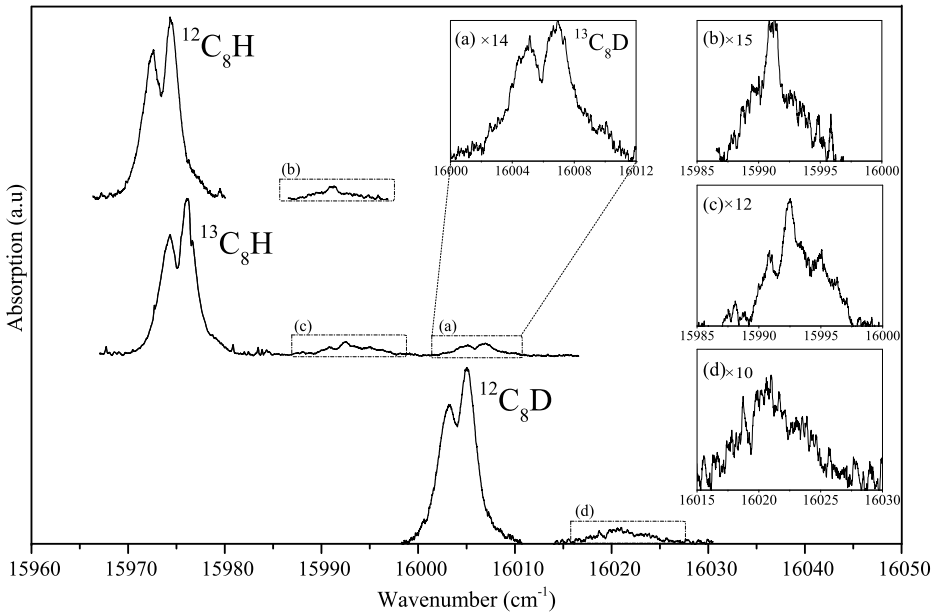

Figure 7.1 – The $^2\Pi - \widetilde{X}^2\Pi$ electronic origin band transition of C_8H (upper trace), $^{13}C_8H$ (middle trace) and C_8D (lower trace) observed by cavity ring down spectroscopy in a pulsed pinhole jet plasma. The weak origin band of the $^2\Pi - \widetilde{X}^2\Pi$ electronic transition of $^{13}C_8D$ is shown in panel (a) and an unstructured component of a sequence transition of the lowest frequency bending mode is shown in panels (b), (c) and (d) for C_8H, $^{13}C_8H$ and C_8D, respectively.

C_8H deviates less than 1% from the measured value of $B_0'' = 0.019589$ cm^{-1} in Ref. [200; 202]. In view of these accurate predictions and because it is not possible to constrain both ground and excited state rotational constants from the unresolved spectra, the B_0'' values for C_8D and $^{13}C_8H$ were fixed to the B_e'' values. With this assumption it is possible to extract the upper state parameters B' and T_{00} as well as Lorentzian line widths Γ from a fitting routine. In all fits special care has been taken to check the correlation factor between the floating parameters, to guarantee that the derived parameters reflect unique and uncorrelated values. Further details of these fits are discussed below.

Firstly, some assumptions were made on the spin-orbit structure of ground and excited states. It is known that the $^2\Pi_{1/2} - \widetilde{X}^2\Pi_{1/2}$ transition is hidden under the strong $^2\Pi_{3/2} - \widetilde{X}^2\Pi_{3/2}$ transition [205], which is much stronger – for low temperatures – in all even-numbered $C_{2n}H$ chains studied here, as these exhibit an inverted spin-orbit structure, i.e., with $\widetilde{X}^2\Pi_{3/2}$ as the lower level. In view of the rather large value of the spin-orbit splitting $A'' = -19.34$ cm^{-1} for C_8H, the $^2\Pi_{1/2} - \widetilde{X}^2\Pi_{1/2}$ component starts to contribute a significant intensity to the spectrum only for internal temperatures of $T_{rot} \gtrsim 30$ K (assuming thermal equilibrium between spin-orbit and rotational excitations). For the lower T_{rot} values therefore mainly the lower spin orbit component contributes to the spectral appearance.

Several spectra were recorded in the pinhole plasma expansion for ∼15 mm downstream at ∼7 − 9 K, displayed in Fig. 7.2 (a,b,c) for which the population of the $X^2\Pi_{1/2}$ spin-orbit state of C_8H is less than 2%. In analyzing the spectral information the focus was on these cold spectra, where use can be made of a standard Hamiltonian restricted to the $^2\Pi_{3/2} - \widetilde{X}^2\Pi_{3/2}$ transition with neglect of the $^2\Pi_{1/2} - \widetilde{X}^2\Pi_{1/2}$ spin-orbit component. Fig. 7.2 shows contour fits performed for the $n = 4$ isotopologues. The fitting results of the cold (∼7 − 9 K) spectra of C_8H, C_8D and $^{13}C_8H$, as shown in the panels (a), (c) and (e) of Fig. 7.2 are considered to be most reliable in view of the absence of contributions by the weaker spin-orbit component. The resulting parameters, as summarized in Table 7.1, are based on these cold spectra. A comprehensive fitting routine in which four variables - B', T_{00}, Γ and T_{rot} - are simultaneously fitted yields effective values for the Lorentzian line broadening parameters: $\Gamma = 0.79 \pm 0.10$ cm^{-1} (C_8H), $\Gamma = 0.84 \pm 0.10$ cm^{-1} (C_8D) and $\Gamma = 0.79 \pm 0.15$ cm^{-1} ($^{13}C_8H$). The covariance matrix of these fits yields a low correlation between the variables; in particular the result for the broadening parameter Γ is well-constrained and unaffected by correlations for these spectra of good signal-to-noise ratio with a clearly resolved splitting between the R- and a P-branch. The spread in the Γ-values as obtained from multiple recordings is small, thus leading to small uncertainty margins on the final result. The uncertainties given in Table 7.1 are related to cold spectra only, and are relatively small as temperature dependent interferences - i.e., contributions from the second spin-orbit component for $T > 30$ K can be neglected.

The life time broadening parameter is consistent for all three isotopologues studied in detail and amounts to $\Gamma = 0.8 \pm 0.1$ cm^{-1} for the $n = 4$ tier of

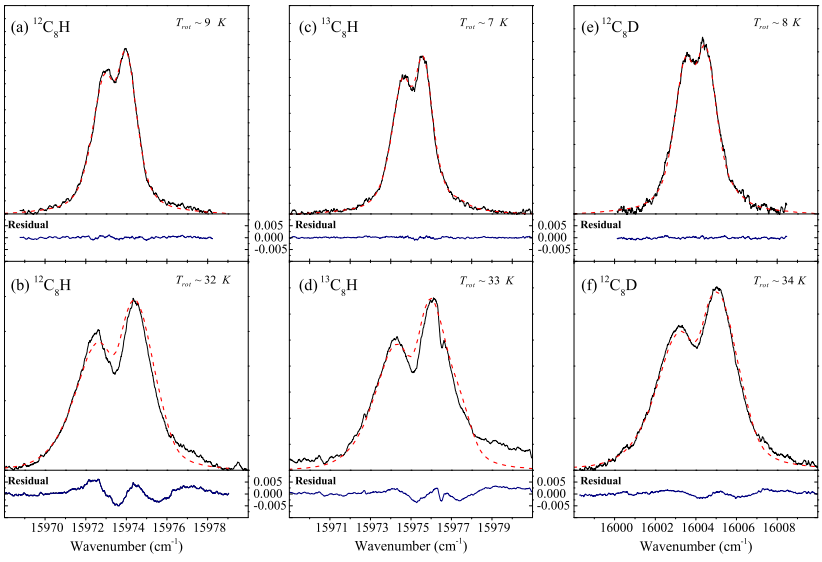

Figure 7.2 – Low and high temperature spectra for the three band systems shown in Fig. 7.1. The result of the contour plot fits is incorporated in red, using the constants listed in Table 7.1.

molecules. This value correspond to a lifetime of ∼7 ps for the upper $^2\Pi_{3/2}$ electronic state, in agreement with the value derived in Ref. [206].

As for the warmer spectra, with typical temperatures of 30 K and displayed in Fig. 7.2 (d,e,f), the intensity contribution of the $^2\Pi_{1/2} - \widetilde{X}^2\Pi_{1/2}$ spin-orbit component must be accounted for, leading to a number of difficulties. These spectra show substantial deviations from the simulations. In Refs. [206; 210], it was noticed that the rotationally resolved $\widetilde{A}^1A_2 - \widetilde{X}^1A_1$ band system of l-C_3H_2 overlaps with the C_8H band. However, even in our ∼30 K spectra, the absorption features of l-C_3H_2 are found to be very weak, and careful inspection of the spectrum shows that the low intensity l-C_3H_2 features are sharp. Therefore they cannot explain the residuals in the higher-temperature spectra. A possible alternative explanation for the residual in the fits of warmer spectra is that the contribution of the upper spin-oribt transition becomes visible. A simplification in the fitting routine is introduced by adopting the values for the molecular parameters B' and Γ as obtained from the cold spectra. In this case the modeling involves a value for the excited state spin-orbit constant A' as an extra parameter in the fitting routine. As a further approximation, we therefore performed fits for the warmer spectra with a fixed value of $A' = -20.5$ cm^{-1}, to comply with an estimate of $|A'' - A'| \leqslant 1.5$ cm^{-1} as deduced in Ref. [205]. Fig. 7.2 (d,e,f) shows the results of simulations for the warmer spectra, in which the rotational temperature T_{rot} was optimized by fitting. These simulations validate the bound $|A'' - A'| \leqslant 1.5$ cm^{-1} and the value of T_{00} coinciding with that found for the colder spectra.

It is of importance that the spectra of the $n = 4$-tier of molecules (C_8H, C_8D, and $^{13}C_8H$) provide an experimental correlation between the setting of the distance between the pinhole nozzle orifice and the optical cavity axis and the internal temperature T_{rot} of the molecular species detected downstream. With the assumption that the internal temperature relaxation of the molecular species is not strongly molecule specific, this provides a handle on preparing the larger chain molecules of the $n = 5$ and $n = 6$ tiers at certain temperatures.

7.3.2 $C_{10}H$, $C_{10}D$, $^{13}C_{10}H$ and $^{13}C_{10}D$

Spectral recordings of the $^2\Pi - \widetilde{X}^2\Pi$ electronic origin band transitions of $C_{10}H$ and $C_{10}D$ are shown in Fig. 7.3. The present S/N ratio is better than that of the previously published spectra [205]. Also shown in Fig. 7.3 is the $^2\Pi - \widetilde{X}^2\Pi$ band of $^{13}C_{10}H$, which is obtained from a ^{13}C enriched sample of precursor gas. The absorption peak near 14020 cm^{-1} has no equivalent in the ^{12}C-spectra and is shown in the inset. It is blue shifted $\leqslant$1.0 cm^{-1} w.r.t. $C_{10}D$, i.e., a value similar to the difference found for $C_{10}H$ and $^{13}C_{10}H$. Therefore, the explanation of this feature is fully consistent with an assignment to $^{13}C_{10}D$ and originates from the same pollution of precursor gas that was discussed above. Its resulting spectrum is not of sufficient quality to perform a contour fitting delivering significant results. The spectra of these larger chains of the

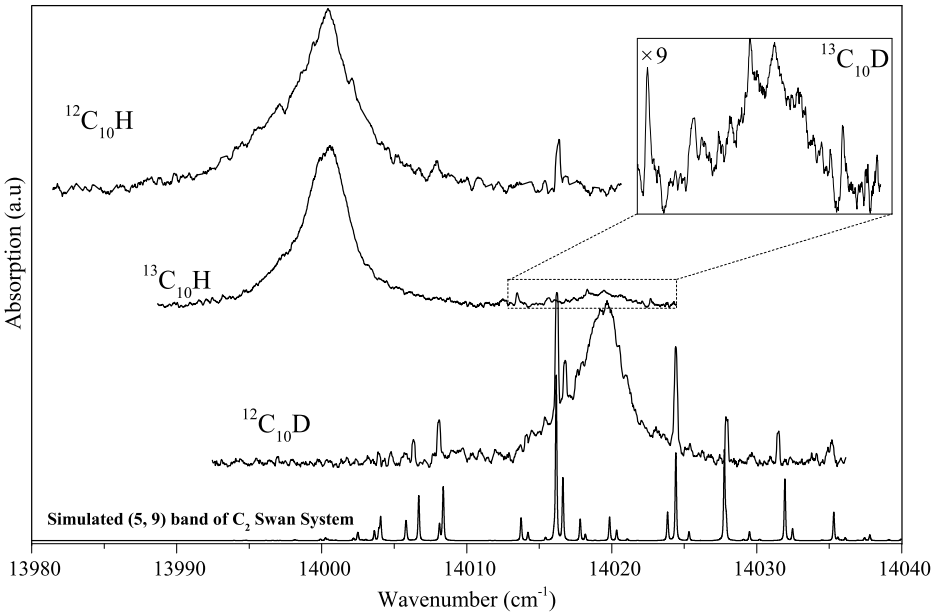

Figure 7.3 – The $^2\Pi - \widetilde{X}^2\Pi$ electronic origin band transition of $C_{10}H$ (upper trace), $^{13}C_{10}H$ (middle trace) and $C_{10}D$ (lower trace) observed by cavity ring down spectroscopy in a pulsed pinhole jet plasma. The $C_{10}H$ and $C_{10}D$ spectra are partially blended with sharp absorption lines of C_2 as can be concluded from the simulated spectrum of the $(5, 9)$ band of the C_2 Swan system.

$n = 5$ tier are not expected to be rotationally resolved – the $2B$ (≈ 0.03 cm^{-1}) separation is smaller than the achievable resolution – and moreover, the spectra may be lifetime broadened as in the case of C_8H.

Several sharp features show up in the $C_{10}H$ and $C_{10}D$ spectra that are not found in a $^{13}C_2H_2$/Ar/He plasma and therefore must be due to ^{12}C-containing species. Indeed, the simulated spectrum for the $(5, 9)$ ro-vibronic band of the $^{12}C_2$ Swan system [208] – shown in Fig. 7.3 – fully reproduces the observed transitions and is used for calibrating the spectra. For the contour fitting procedures to be carried out these sharp features were erased from the spectra.

The recorded $C_{10}H$, $C_{10}D$ and $^{13}C_{10}H$ spectra do not exhibit distinctive P- and R-branches and appear as a single unresolved bump structure. This makes the analysis of the spectra even more difficult than in the case of C_8H. A major difficulty encountered is that a simultaneous multi-parameter fitting analysis optimizing the parameters B', T_{00}, Γ and T_{rot} is no longer possible, not even for the coldest spectra.

The strategy chosen to analyze these spectra is to include as much as available a priori knowledge and focus a fitting routine to extract information on the natural life time broadening of the upper electronic state. For the main $C_{10}H$ isotopologue the ground state rotational constant $B_0'' = 0.010054$ is taken from available microwave data [200]. For the remainder, the rotational constants of B'' and B' are set to calculated or reliably estimated values. For the $C_{10}D$

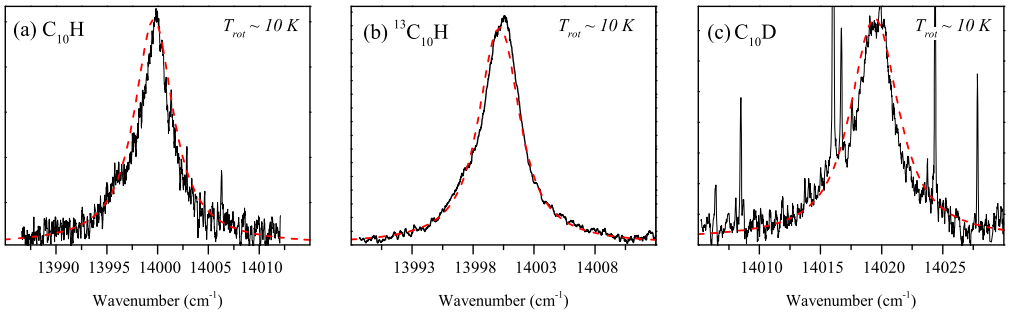

Figure 7.4 – The cold spectra for the three band systems shown in Fig. 7.3. The result of the contour plot fits for T_{rot} = 10 K is incorporated in red, using the constants listed in Table. 7.1.

and $^{13}C_{10}H$ isotopologues, where no microwave data are available, the ground state rotational constants are fixed to calculated values of $B''_e = 0.009819$ cm^{-1} and $B''_e = 0.009328$ cm^{-1}, respectively. The ratio of B''/B', derived from rotationally resolved spectra of C_6H and C_6D in Ref. [107], is consistent with the corresponding value found for HC_6H^+ and DC_6D^+ reported in Ref. [211]. Hence, the B'' values for $C_{10}H$, $C_{10}D$ and $^{13}C_{10}H$ are estimated from the ratio of $B''/B' = 1.007$ reported for their iso-electronic $HC_{10}H^+$ and $DC_{10}D^+$ species [211]. We assumed that the ratio of B''/B' for $^{13}C_{10}H$ is the same as for $C_{10}H$. No accurate information on the spin-orbit constants A'' and A' is available for neither of the isotopologues. However, as explained in the above section, this is not required for analyzing the coldest spectra, where the contribution of the weaker $^2\Pi_{1/2} - \widetilde{X}^2\Pi_{1/2}$ spin-orbit component can be safely neglected. In that case the band origin T_{00} represents the splitting between the $\Omega = 3/2$ components in ground and excited electronic states. Based on this list of assumptions the coldest accessible spectra are analyzed by contour fitting, aiming to derive the values of the Lorentzian line widths Γ and the band origins T_{00} for the molecules in the $n = 5$ tier.

Fig. 7.4 shows the observed and simulated cold spectra for $C_{10}H$, $C_{10}D$ and $^{13}C_{10}H$ using the estimated values as listed in Table 7.1. The best contour fits are realized for Lorentzian line widths of $\Gamma = 4.7 \pm 0.5$ cm^{-1} for $C_{10}H$, $\Gamma = 4.3 \pm 0.5$ cm^{-1} for $C_{10}D$, and $\Gamma = 3.5 \pm 0.3$ cm^{-1} for $^{13}C_{10}H$. These fits were performed for a temperature setting of 10 K, as was established from the nozzle-optical axis setting in the previous C_8H experiment. Again, it should be noted that the analysis is based on calculated values for B'' and B', and the neglect of population of the $^2\Pi_{1/2}$ component. It was verified that the simulated spectra are not sensitive for the exact temperature setting and reproduced the experimental features for settings in the window $T_{rot} = 5 - 15$ K. The resulting values, on average $\Gamma = 4.0$ cm^{-1}, correspond to a lifetime of about ~1.3 ps for the upper $^2\Pi_{3/2}$ electronic state, is shorter than found for C_8H. Very good agreement is found between the observed spectra and the fitted contours.

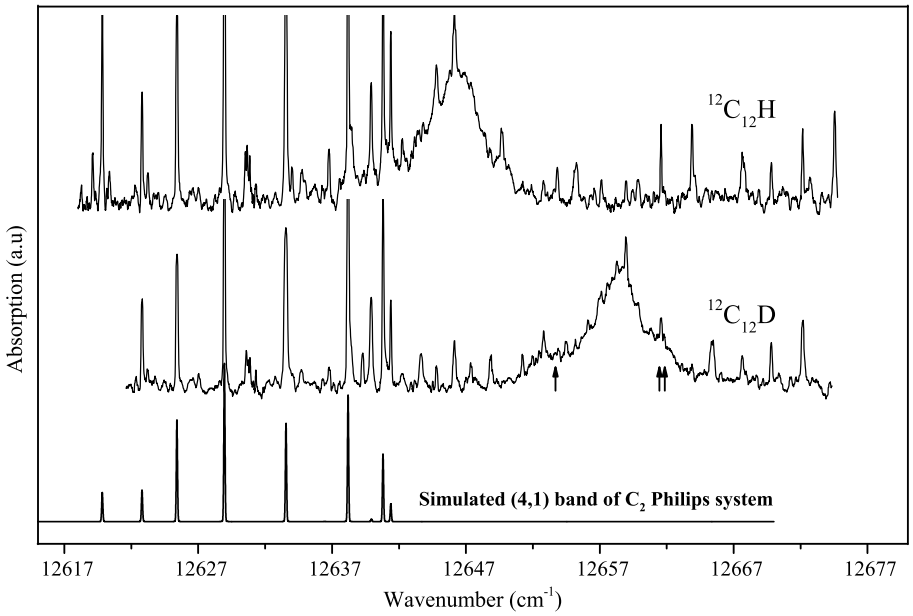

Figure 7.5 – The $^2\Pi - \widetilde{X}^2\Pi$ electronic origin band transition of $C_{12}H$ (upper trace) and $C_{12}D$ (lower trace) observed by cavity ring down spectroscopy in a pulsed pinhole jet plasma. The origin of the side-bands to the main peak in the $C_{12}D$ spectrum, marked by arrows, is unknown (see text). Polluting transitions are due to $(4, 1)$ band transitions of the C_2 Philips system as simulated in red.

7.3.3 $C_{12}H$, $C_{12}D$

Spectral recordings of the gas-phase $^2\Pi - \widetilde{X}^2\Pi$ electronic origin band transitions of $C_{12}H$ and $C_{12}D$ are shown in Fig. 7.5. The spectra exhibit a better S/N than available from the previous studies [91; 207]. Also for these carbon chain molecules in the $n = 6$ tier, for which adjacent rotational lines are expected to be split by only 0.01 cm^{-1}, rotational structures cannot be resolved due to the combination of limited laser bandwidth and the Doppler broadening in the pinhole jet expansion, while also lifetime broadening is expected to be at play. For these reasons the spectra appear as unstructured single bump features.

The $C_{12}H$ to $C_{12}D$ isotopic shift amounts to $\sim$12 cm^{-1}, which is less than the $\sim$20 cm^{-1} and $\sim$30 cm^{-1} shifts found for $C_{10}H$ and C_8H, respectively. We tried to record a spectrum for the $^{13}C_{12}H$ species applying similar settings as used for $^{13}C_8H/D$ and $^{13}C_{10}H/D$, but did not succeed. Again spectral overlap exists with transitions that originate from small radicals. In this specific case the features arise from the $(4, 1)$ band of the C_2 Philips system as shown in the lower trace of Fig. 7.5. Fig. 7.6 shows the observed cold spectra for $C_{12}H$ and $C_{12}D$. As in the previous sections, contour fitting has been applied for several cold spectra using a standard $^2\Pi_{3/2} - {}^2\Pi_{3/2}$ Hamiltonian. The recorded $C_{12}H$ and $C_{12}D$ spectra are analyzed following similar procedures as laid out for $C_{10}H$ and $C_{10}D$.

The rotational constant B'' of $C_{12}H$ in its $\widetilde{X}^2\Pi$ ground electronic state is known from microwave spectroscopy [200], while for $C_{12}D$ a value of $B''_e = 0.005558$ cm^{-1} has been determined from our *ab initio* calculations. Different from the case of $C_{10}H$ discussed above, the B''/B' for the iso-electronic $HC_{12}H^+$ is not available. However, based on the discussion in Ref. [211] that the B''/B' ratio decreases with chains length increasing, the B''/B'~1.002 for $HC_{12}H^+$ can be extrapolated from the available data for shorter $HC_{2n}H^+$ species [211]. Here, this ratio is used to estimated the excited state constants B' for $C_{12}H$ and $C_{12}D$.

Contour fits are performed to the experimental spectra by fixing the B'' and B' rotational constants to calculated and estimated values, while T_{00} as well as Lorentzian line widths Γ are varied to reproduce the spectra. Again it is assumed that the effect of spin-orbit interaction can be neglected for the cold spectra with population in the inverted $\widetilde{X}^2\Pi_{3/2}$ ground state only. Optimized contours for $C_{12}H$ and $C_{12}D$ are obtained for the values listed in Table 7.1. Lorentzian line widths of $\Gamma = 4.7 \pm 0.7$ cm^{-1} for $C_{12}H$ and $\Gamma = 4.8 \pm 0.5$ cm^{-1} for $C_{12}H$ are determined and found to be uncorrelated with other fit parameters. Thus an upper $^2\Pi_{3/2}$ state lifetime of ~1.1 ps results for the species in the $n = 6$ tier.

In the warmer spectra of $C_{12}D$, at internal temperatures of $T_{rot} \sim 30$ K estimated from the nozzle-to-optical axis setting, two shoulders appear as side-band features - indicated with single and double arrows in Fig. 7.5. These features do not appear in the spectra of $C_{12}H$, and are also not visible in the spectra recorded at lower temperatures of $T_{rot} < 10$ K, so they do not affect the contour fitting analysis and the lifetime determinations. As there seems to be a temperature dependency involved, explanations of these features may range from a hot band or a higher population of the upper spin-orbit component.

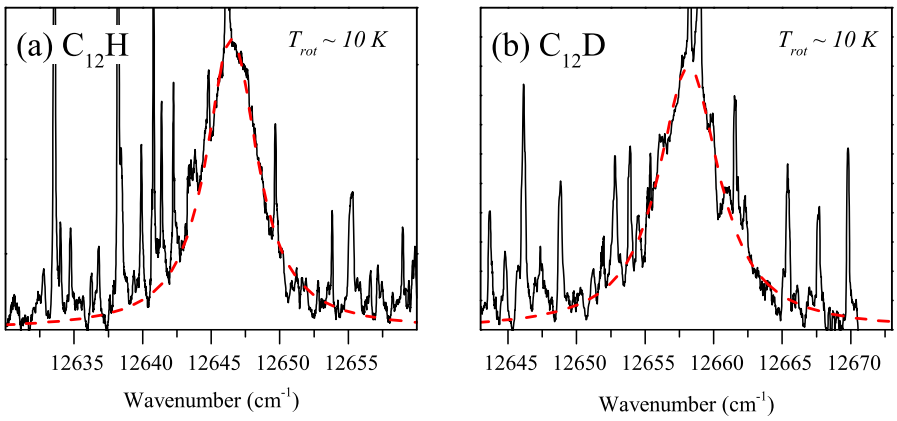

Figure 7.6 – The cold spectra for the two bands shown in Fig. 7.5. The result of the contour plot fits for $T_{rot} = 10$ K is incorporated in red, using the constants listed in Table. 7.1.

Table 7.1 – Effective constants derived (in cm^{-1}) from contour fit analyses of the $^2\Pi - \widetilde{X}^2\Pi$ electronic origin band spectra of C_8H, $C_{10}H$, $C_{12}H$ and their D- and ^{13}C fully substituted isotopologues. The digits in the parentheses represent the standard deviation of averaged values. Values derived from the fit of the cold spectra and only from $^2\Pi_{3/2} - \widetilde{X}^2\Pi_{3/2}$ transition (see the text).

	$\widetilde{X}^2\Pi$ Ground state	$^2\Pi_{3/2}$ Excited state			
	B''	B'	$T_{00}(\Omega{=}3/2)$	$T_{00} - T_{00(\,^{12}C_nH)}$	Γ
C_8H	0.019589[a]	0.01938(2)	15973.5(2)	0	0.79 ± 0.10
$^{13}C_8H$	0.018153[b]	0.01790(4)	15975.1(6)	~2	0.79 ± 0.15
C_8D	0.018961[b]	0.01878(5)	16004.0(5)	~30	0.84 ± 0.10
$C_{10}H$	0.010054[a]	0.009984[c]	14000.0(9)	0	4.7 ± 0.5
$^{13}C_{10}H$	0.009328[b]	0.009263[c]	14000.2(6)	~1	3.5 ± 0.3
$C_{10}D$	0.009819[b]	0.009751[c]	14019.4(5)	~20	4.3 ± 0.5
$C_{12}H$	0.005830[a]	0.005818[c]	12646.4(5)	0	4.7 ± 0.7
$C_{12}D$	0.005558[b]	0.005547[c]	12658.5(7)	~12	4.8 ± 0.5

[a] From Ref. [200; 202].
[b] Calculated values - Fixed.
[c] Calculated from an estimated ratio of B''/B'- Fixed.

A possible alternative explanation for these shoulders is that they are related to other species simultaneously generated in the plasma. At this stage this observation cannot be explained.

7.4 Discussion and Conclusions

It may seem counterintuitive to extract a value for the life time broadening from a rotationally unresolved contour, where the exact value for the excited state rotational constant is lacking and the rotational temperature is not accurately known. However, for all the individual analyses it was verified that the extracted values of the life time broadening were not sensitively dependent on the estimated or calculated values for the rotational constants. In Fig. 7.7 additional material is shown to graphically illustrate the determination of the line broadening parameters Γ in each of the contour-fitted spectra of C_8H, $C_{10}H$ and $C_{12}H$. The contour fits are recalculated for varying Γ parameters in a range around the optimum values as listed in Table 7.1. This procedure is in fact repeated (not shown) for spectra recorded at different temperature settings, therewith producing reliable and consistent values for the line broadening. For all $C_{2n}H$ carbon chains investigated in the present study, with $n = 4, 5$ and 6, all upper $^2\Pi$ states undergo lifetime broadening.

The interesting outcome of the present experimental study on the spectra of long $^{12/13}C_{2n}H/D$ carbon chain molecules, therefore is that even for the unresolved spectra an effective lifetime broadening can be deduced, by fixing the spectroscopy in the fit making quite straight forward assumptions. The Γ values are derived for 'ideal spectra', i.e., low temperature spectra where the influence of interfering patterns can be largely neglected. The resulting lifetime values for $C_{10}H$ and $C_{12}H$ are larger than found for C_8H and the latter value is again larger than concluded from fully rotationally spectra of C_6H where actually no proof for lifetime broadening was found. These observations are independent of isotopic composition, and can in principle be ascribed to either predissociation or internal non-radiative decay. In view of the low excitation energies of the excited states and the dissociation products of such linear carbon chains carrying higher internal energies the short life times of the carbon chain species investigated must be due to intramolecular energy conversion/redistribution processes, likely governed by resonant or non-resonant perturbations, possibly even complex state mixing. In the energy region of the excited $^2\Pi$ state the total vibronic state density of such long chains containing more than nine atoms is expected to be sufficiently large. In comparison the odd-numbered $C_{2n+1}H$ carbon chain species behave differently; the smaller C_5H species is already lifetime broadened [183] with an upper state lifetime of 1.6 ± 0.3 ps.

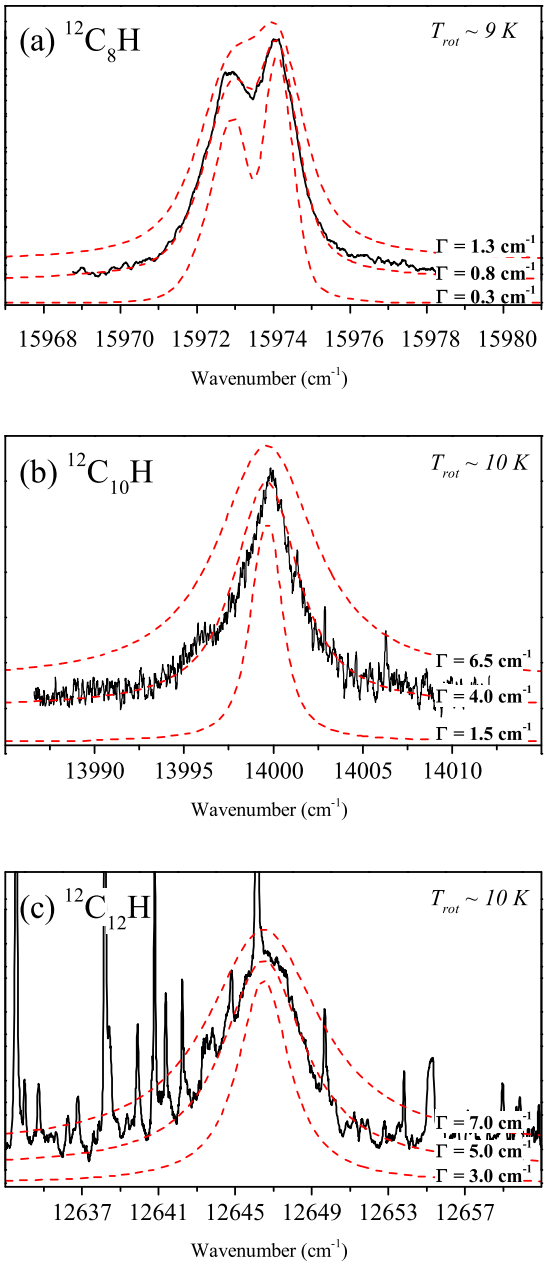

Figure 7.7 – Recorded spectrum of the $^2\Pi - \widetilde{X}^2\Pi$ electronic origin band transition of C_8H (panel a), $C_{10}H$ (panel b) and $C_{12}D$ (panel c). Simulated spectra for different Lorentzian line width values are shown in each panel.

7.5 Acknowledgments

We acknowledge financial support by FOM, NOVA and the 'Stichting Physica'. This work has been performed as part of ongoing research within the Dutch Astrochemistry Network.

Bibliography

[1] *http://www.astro.uni-koeln.de/cdms/molecules* (2013).

[2] J. Cami, J. Bernard-Salas, E. Peeters, and S. Malek, Science **329**, 1180 (2010).

[3] S. Milam, C. Savage, M. Brewster, L. Ziurys, and S. Wyckoff, Astrophys. J. **634**, 1126 (2005).

[4] W. Langer and A. Penzias, Astrophys. J. **408**, 539 (1993).

[5] C. Kahane, J. Cernicharo, J. Gomez-Gonzalez, and M. Guélin, Astron. Astrophys. **256**, 235 (1992).

[6] D. Jewitt, H. Matthews, T. Owen, and R. Meier, Science **278**, 90 (1997).

[7] P. Swings and L. Rosenfeld, Astrophys. J. **86**, 483 (1937).

[8] A. McKellar, Publ. Astron. Soc. Pac. **52**, 312 (1940).

[9] W. Adams, Astrophys. J. **93**, 11 (1941).

[10] A. Douglas and G. Herzberg, Astrophys. J. **94**, 381 (1941).

[11] G. Herzberg, *Molecular spectra and molecular structure. Vol. 1: Spectra of diatomic molecules* (New York: Van Nostrand Reinhold, 1950).

[12] S. Souza and B. Lutz, Astrophys. J. **216**, L49 (1977).

[13] K. Hinkle, J. Keady, and P. Bernath, Science **241**, 1319 (1988).

[14] J. Maier, N. Lakin, G. Walker, and D. Bohlender, Astrophys. J. **553**, 267 (2001).

[15] T. Henning and F. Salama, Science **282**, 2204 (1998).

[16] A. Tielens, Annu. Rev. Astron. Astrophys. **46**, 289 (2008).

[17] Y. J. Pendleton and L. J. Allamandola, Astrophys. J. Suppl. S. **138**, 75 (2002).

[18] P. Ehrenfreund and J. Cami, Cold Spring Harb. Perspect Biol. **2**, 002527 (2010).

[19] M. L. Heger, Lick Obs. Bull. **10**, 141 (1922).

[20] P. Merrill, Publ. Astron. Soc. Pac. **46**, 206 (1934).

[21] P. Merrill, Astrophys. J. **83**, 126 (1936).

[22] P. Merrill and O. Wilson, Astrophys. J. **87**, 9 (1938).

[23] T. Snow and B. McCall, Annu. Rev. Astron. Astrophys. **44**, 367 (2006).

[24] T. Geballe, F. Najarro, D. Figer, B. Schlegelmilch, and D. de La Fuente, Nature **479**, 200 (2011).

[25] H. Russell, Mon. Not. R. Astron. Soc. **95**, 610 (1935).

[26] T. Snow, Spectrochim. Acta. A. **57**, 615 (2001).

[27] P. Sarre, J. Miles, T. Kerr, R. Hibbins, S. Fossey, and W. Somerville,

Mon. Not. R. Astron. Soc. **277**, L41 (1995).

[28] P. Ehrenfreund, B. Foing, L. d'Hendecourt, P. Jenniskens, and F. Desert, Astron. Astrophys. **299**, 213 (1995).

[29] J. Krełowski and M. Schmidt, Astrophys. J. **477**, 209 (1997).

[30] T. Kerr, R. Hibbins, J. Miles, S. Fossey, W. Somerville, and P. Sarre, Mon. Not. R. Astron. Soc. **283**, L105 (1996).

[31] A. Webster, Mon. Not. R. Astron. Soc. **265**, 421 (1993).

[32] P. Le Coupanec, D. Rouan, and A. Leger, Astron. Astrophys. **338**, 217 (1998).

[33] P. Hinnen and W. Ubachs, Chem. Phys. Lett. **254**, 32 (1996).

[34] P. Sorokin, J. Glownia, and W. Ubachs, Farad. Discuss. **109**, 137 (1998).

[35] J. Dorschner, Nature **231**, 124 (1971).

[36] E. Ensberg and K. Jefferts, Astrophys. J. **195**, L89 (1975).

[37] A. Webster, Mon. Not. R. Astron. Soc. **255**, 41 (1992).

[38] B. Foing and P. Ehrenfreund, Astron. Astrophys. **317**, L59 (1997).

[39] H. W. Kroto, J. R. Heath, S. C. O'Brien, R. F. Curl, and R. E. Smalley, Nature **318**, 162 (1985).

[40] S. Leach, M. Vervloet, A. Després, E. Bréheret, J. P. Hare, T. John Dennis, H. W. Kroto, R. Taylor, and D. R. Walton, Chem. Phys. **160**, 451 (1992).

[41] J. Fulara, M. Jakobi, and J. Maier, Chem. Phys. Lett. **211**, 227 (1993).

[42] A. Léger and L. d'Hendecourt, Astron. Astrophys. **146**, 81 (1985).

[43] L. Allamandola, A. Tielens, and J. Barker, Astrophys. J. **290**, L25 (1985).

[44] J. Maier, G. Walker, and D. Bohlender, Astrophys. J. **602**, 286 (2004).

[45] G. Herbig, Annu. Rev. Astron. Astrophys. **33**, 19 (1995).

[46] A. Douglas, Nature **269**, 130 (1977).

[47] G. Van der Zwet and L. Allamandola, Astron. Astrophys. **146**, 76 (1985).

[48] L. d'Hendecourt and M. Jourdain de Muizon, Astron. Astrophys. **223**, L5 (1989).

[49] F. Salama and L. Allamandola, in *Proceedings of the International Astronomical Union, Astrochemistry of Cosmic Phenomena* (Springer, 1992), pp. 25–26.

[50] D. Romanini, L. Biennier, F. Salama, A. Kachanov, L. Allamandola, and F. Stoeckel, Chem. Phys. Lett. **303**, 165 (1999).

[51] F. Salama and L. Allamandola, Nature **358**, 42 (1992).

[52] W. Duley, Astrophys. J. Lett. **643**, L21 (2006).

[53] P. Ehrenfreund, L. d'Hendecourt, L. Verstraete, A. Léger, W. Schmidt, and D. Defourneau, Astron. Astrophys. **259**, 257 (1992).

[54] L. Allamandola, *Laboratory studies of DIB carriers* (Springer, 1995).

[55] G. Mitchell and W. Huntress, Nature **278**, 722 (1979).

[56] E. Jochnowitz and J. Maier, Mol. Phys. **106**, 2093 (2008).

[57] M. Tulej, D. Kirkwood, M. Pachkov, and J. Maier, Astrophys. J. Lett. **506**, L69 (1998).

[58] B. McCall, J. Thorburn, L. Hobbs, T. Oka, and D. York, Astrophys. J. Lett. **559**, L49 (2001).

[59] C. Rice and J. Maier, J. Phys. Chem. A **117**, 5559 (2013).

[60] J. Maier, G. Walker, D. Bohlender, F. Mazzotti, R. Raghunandan, J. Fulara, I. Garkusha, and A. Nagy, Astrophys. J. **726**, 41 (2011).

[61] T. Oka and B. McCall, Science **331**, 293 (2011).

[62] Z. Guennoun and J. P. Maier, *Electronic spectroscopy of transient molecules* (Wiley Online Library, 2011).

[63] T. Motylewski and H. Linnartz, Rev. Sci. Instrum. **70**, 1305 (1999).

[64] A. O'Keefe and D. A. Deacon, Rev. Sci. Instrum. **59**, 2544 (1988).

[65] D. Romanini, A. Kachanov, N. Sadeghi, and F. Stoeckel, Chem. Phys. Lett. **264**, 316 (1997).

[66] B. Paldus, C. Harb, T. Spence, B. Wilke, J. Xie, J. Harris, and R. Zare, J. Appl. Phys. **83**, 3991 (1998).

[67] R. Engeln, G. Berden, R. Peeters, and G. Meijer, Rev. Sci. Instrum. **69**, 3763 (1998).

[68] R. Engeln, G. von Helden, G. Berden, and G. Meijer, Chem. Phys. Lett. **262**, 105 (1996).

[69] R. Engeln, G. Berden, E. van den Berg, and G. Meijer, J. Chem. Phys. **107**, 4458 (1997).

[70] A. C. Pipino, J. W. Hudgens, and R. E. Huie, Chem. Phys. Lett. **280**, 104 (1997).

[71] A. Pipino, J. Hudgens, and R. Huie, Rev. Sci. Instrum. **68**, 2978 (1997).

[72] R. Engeln and G. Meijer, Rev. Sci. Instrum. **67**, 2708 (1996).

[73] G. Berden, R. Peeters, and G. Meijer, Int. Rev. Phys. Chem. **19**, 565 (2000).

[74] K. W. Busch and M. A. Busch, eds., *Cavity-ringdown spectroscopy: an ultratrace-absorption measurement technique*, vol. 720 of *ACS Symp. Ser.* (Amer Chemical Society, 1999).

[75] G. Berden and R. Engeln, *Cavity ring-down spectroscopy* (Wiley Online Library, 2009).

[76] J. Scherer, J. Paul, A. O'Keefe, and R. Saykally, Chem. Rev. **97**, 25 (1997).

[77] M. Wheeler, S. Newman, A. Orr-Ewing, and M. Ashfold, J. Chem. Soc., Faraday Trans. **94**, 337 (1998).

[78] D. Ityaksov, Ph.D. thesis, VU University Amsterdam (2009).

[79] *PGOPHER, a Program for Simulating Rotational Structure, C. M. Western, University of Bristol, http://pgopher.chm.bris.ac.uk.*

[80] I. Nenner, *Molecules and Grains in Space: 50th International Meeting of Physical Chemistry, Mont Sainte-Odile, France, September 1993*, vol. 312 (Amer. Inst. of Physics, 1994).

[81] C. Demuynck, J. Mol. Spectrosc. **168**, 215 (1994).

[82] E. Hirota, Chem. Rev. **92**, 141 (1992).

[83] P. Bernath, Annu. Rev. Phys. Chem. **41**, 91 (1990).

[84] D. Levy, Annu. Rev. Phys. Chem. **31**, 197 (1980).

[85] P. Engelking, Rev. Sci. Instrum. **57**, 2274 (1986).

[86] K. Veeken and J. Reuss, Appl. Phys. B **38**, 117 (1985).

[87] O. Hagena, Surf. Sci. **106**, 101 (1981).

[88] H. Linnartz, Physica Scripta **69**, 37 (2004).

[89] K. Comer and S. Foster, Chem. Phys. Lett. **202**, 216 (1993).

[90] D. Verdes, H. Linnartz, J. P. Maier, P. Botschwina, R. Oswald, P. Rosmus, and P. J. Knowles, J. Chem. Phys. **111**, 8400 (1999).

[91] T. Motylewski, H. Linnartz, O. Vaizert, J. Maier, G. Galazutdinov, F. Musaev, J. Krełowski, G. Walker, and D. Bohlender, Astrophys. J. **531**, 312 (2000).

[92] L. Biennier, F. Salama, L. J. Allamandola, and J. J. Scherer, J. Chem. Phys. **118**, 7863 (2003).

[93] L. Biennier, A. Benidar, and F. Salama, Chem. Phys. **326**, 445 (2006).

[94] J. Remy, L. Biennier, and F. Salama, Plasma Sci. Technol. **12**, 295 (2003).

[95] D. Zhao, M. A. Haddad, H. Linnartz, and W. Ubachs, J. Chem. Phys. **135**, 074201 (2011).

[96] D. Halmer, G. von Basum, P. Hering, and M. Murtz, Rev. Sci. Instrum. **75**, 2187 (2004).

[97] M. Bell, P. Feldman, J. Watson, M. McCarthy, M. Travers, C. Gottlieb, and P. Thaddeus, Astrophys. J. **518**, 740 (1999).

[98] M. Guélin, J. Cernicharo, M. Travers, M. McCarthy, C. Gottlieb, P. Thaddeus, M. Ohishi, S. Saito, and S. Yamamoto, Astron. Astrophys. **317**, L1 (1997).

[99] J. Cernicharo, M. Guelin, and C. Walmsley, Astron. Astrophys. **172**, L5 (1987).

[100] J. Cernicharo, C. Kahane, J. Gomez-Gonzalez, and M. Guelin, Astron. Astrophys. **164**, L1 (1986).

[101] T. Crawford, J. Stanton, J. Saeh, and H. Schaefer, J. Am. Chem. Soc. **121**, 1902 (1999).

[102] F. Pauzat, Y. Ellinger, and A. D. McLean, Astrophys. J. **369**, L13 (1991).

[103] C. Gottlieb, E. Gottlieb, and P. Thaddeus, Astron. Astrophys. **164**, L5 (1986).

[104] T. Hirota, H. Ozawa, Y. Sekimoto, and S. Yamamoto, J. Mol. Spectrosc. **174**, 196 (1995).

[105] H. Ding, T. Pino, F. Guthe, and J. Maier, J. Chem. Phys. **117**, 8362 (2002).

[106] J. Haubrich, M. Muhlhauser, and S. Peyerimhoff, J. Phys. Chem. A **106**, 8201 (2002).

[107] D. Zhao, M. A. Haddad, H. Linnartz, and W. Ubachs, J. Chem. Phys. **135**, 044307 (2011).

[108] N. Wehres, D. Zhao, W. Ubachs, and H. Linnartz, Chem. Phys. Lett. **497**, 30 (2010).

[109] D. Zhao, N. Wehres, H. Linnartz, and W. Ubachs, Chem. Phys. Lett. **501**, 232 (2011).

[110] G. Herzberg, *Molecular Spectra and Molecular Structure I. Spectra of Diatomic Molecules,* (D. Van Nostrand, New York, 1950).

[111] P. Birza, T. Motylewski, D. Khoroshev, A. Chirokolava, H. Linnartz, and J. Maier, Chemical Physics **283**, 119 (2002).

[112] D. Pfluger, T. Motylewski, H. Linnartz, W. Sinclair, and J. Maier, Chem. Phys. Lett. **329**, 29 (2000).

[113] H. Linnartz, T. Motylewski, O. Vaizert, J. Maier, A. Apponi, M. McCarthy, C. A. Gottlieb, and P. Thaddeus, J. Mol. Spectrosc. **197**, 1 (1999).

[114] H. Ding, T. Pino, F. Guthe, and J. Maier, J. Chem. Phys. **115**, 6913 (2001).

[115] M. Zachwieja, J. Mol. Spectrosc. **170**, 285 (1995).

[116] Z. Bembenek, R. Kepa, A. Para, M. Rytel, M. Zachwieja, J. D. Janjic, and E. Marx, J. Mol. Spectrosc. **139**, 1 (1990).

[117] G. Herzberg and J. Johns, Astrophys. J. **158**, 399 (1969).

[118] P. Thaddeus, C. Gottlieb, A. Hjalmarson, L. Johansson, W. Irvine, P. Friberg, and R. Linke, Astrophys. J. **294**, L49 (1985).

[119] M. Peric, M. Mladenovic, K. Tomic, and C. Marian, J. Chem. Phys. **118**, 4444 (2003).

[120] F. Mazzotti, R. Raghunandan, A. Esmail, M. Tulej, and J. Maier, J. Chem. Phys. **134**, 164303 (2011).

[121] S. Sheehan, B. Parsons, J. Zhou, E. Garand, T. Yen, D. Moore, and D. Neumark, J. Chem. Phys. **128**, 034301 (2008).

[122] R. Chaudhuri, S. Majumder, and K. Freed, J. Chem. Phys. **112**, 9301 (2000).

[123] K. Homann, Angew. Chem., Int. Ed. **37**, 2434 (1998).

[124] H. Richter and J. Howard, Prog. Energy Combust. Sci. **26**, 565 (2000).

[125] T. Fujii and M. Kareev, J. Appl. Phys. **89**, 2543 (2001).

[126] P. Thaddeus, M. McCarthy, M. Travers, C. Gottlieb, and W. Chen, Farad. Discuss. **109**, 121 (1998).

[127] H. Müller, F. Schlöder, J. Stutzki, and G. Winnewisser, J. Mol. Struct.

742, 215 (2005).

[128] V. Wakelam, I. Smith, E. Herbst, J. Troe, W. Geppert, H. Linnartz, K. Ösberg, E. Roué, M. Agundez, P. Pernot, et al., Space. Sci. Rev. **156**, 13 (2010).

[129] M. McCarthy and P. Thaddeus, Chem. Soc. Rev. **30**, 177 (2001).

[130] A. van Orden and R. Saykally, Chem. Rev. **98**, 2313 (1998).

[131] R. Nagarajan and J. P. Maier, Int. Rev. Phys. Chem. **29**, 521 (2010).

[132] E. Jochnowitz and J. Maier, Annu. Rev. Phys. Chem. **59**, 519 (2008).

[133] T. Schmidt, A. Boguslavskiy, T. Pino, H. Ding, and J. Maier, Int. J. Mass Spectrom. **228**, 647 (2003).

[134] T. Schmidt, H. Ding, A. Boguslavskiy, T. Pino, and J. Maier, J. Phys. Chem. A **107**, 6550 (2003).

[135] H. Ding, T. Pino, F. Güthe, and J. Maier, J. Am. Chem. Soc. **125**, 14626 (2003).

[136] C. Zhang, J. Chem. Phys. **121**, 8212 (2004).

[137] H. Linnartz, ed., *Cavity Ring-Down Spectroscopy-Techniques and Applications* (Wiley-Blackwell, Chichester, United Kingdom, 2009), chap. 6.

[138] A. D. Becke, J. Chem. Phys. **98**, 5648 (1993).

[139] F. Bernardi, A. Bottoni, J. McDouall, M. Robb, and H. Schlegel, Faraday Symp. Chem. Soc. **19**, 137 (1984).

[140] M. Frisch and et al., *GAUSSIAN 03, Revision C.02, Gaussian, Inc., Pittsburgh, PA, 2003.*

[141] M. Andersson and P. Uvdal, J. Phys. Chem. A **109**, 2937 (2005).

[142] G. Herzberg, *Molecular Spectra and Molecular Structure III. Electronic Spectra and Electronic Structure of Polyatomic Molecules* (D. Van Nostrand, New York, 1966).

[143] J. Maier, Chem. Soc. Rev. **26**, 21 (1997).

[144] C. Ball, M. McCarthy, and P. Thaddeus, Astrophys. J. **523**, L89 (1999).

[145] T. Giesen, A. Van Orden, J. Cruzan, R. Provencal, R. Saykally, R. Gendriesch, F. Lewen, and G. Winnewisser, Astrophys. J. **551**, L181 (2001).

[146] P. Neubauer-Guenther, T. Giesen, U. Berndt, G. Fuchs, and G. Winnewisser, Spectrochim. Acta. A. **59**, 431 (2003).

[147] J. Fonfría, J. Cernicharo, M. Richter, and L. Lacy, Astrophys. J. **728**, 43 (2011).

[148] J. Fulara, P. Freivogel, D. Forney, and J. Maier, J. Chem. Phys. **103**, 8805 (1995).

[149] H. Ding, T. Schmidt, T. Pino, A. Boguslavskiy, F. Guthe, and J. Maier, J. Chem. Phys. **119**, 814 (2003).

[150] C. Ball, M. McCarthy, and P. Thaddeus, J. Chem. Phys. **112**, 10149

(2000).

[151] V. Gordon, M. McCarthy, A. Apponi, and P. Thaddeus, Astrophys. J. **540**, 286 (2000).

[152] O. Vaizert, T. Motylewski, M. Wyss, E. Riaplov, H. Linnartz, and J. Maier, J. Chem. Phys. **114**, 7918 (2001).

[153] D. Zhao, K. Doney, and H. Linnartz, J. Mol. Spectrosc. (In press).

[154] M. Mladenović, S. Schmatz, and P. Botschwina, J. Chem. Phys. **101**, 5891 (1994).

[155] K. Ahmed, G. Balint-Kurti, and C. M. Western, J. Chem. Phys. **121**, 10041 (2004).

[156] W. Huggins, Proc. R. Soc. London, Ser. **33**, 1 (1881).

[157] G. Herzberg, Astrophys. J. **96**, 314 (1942).

[158] A. Douglas, Astrophys. J. **114**, 466 (1951).

[159] L. Gausset, G. Herzberg, A. Lagerqvist, and B. Rosen, Discuss. Faraday Soc. **35**, 113 (1963).

[160] L. Gausset, G. Herzberg, A. Lagerqvist, and B. Rosen, Astrophys. J. **142**, 45 (1965).

[161] A. Tielens, *The physics and chemistry of the interstellar medium* (Cambridge University Press, 2005).

[162] R. Kaiser, Chem. Rev. **102**, 1309 (2002).

[163] J. Cernicharo, J. Goicoechea, and E. Caux, Astrophys. J. **534**, L199 (2000).

[164] B. Mookerjea, T. Giesen, J. Stutzki, J. Cernicharo, J. Goicoechea, M. De luca, T. Bell, H. Gupta, M. Gerin, C. Persson, et al., Astron. Astrophys. **521**, L13 (2010).

[165] K. Matsumura, H. Kanamori, K. Kawaguchi, and E. Hirota, J. Chem. Phys. **89**, 3491 (1988).

[166] K. Kawaguchi, K. Matsumura, H. Kanamori, and E. Hirota, J. Chem. Phys. **91**, 1953 (1989).

[167] C. Schmuttenmaer, R. Cohen, N. Pugliano, A. Cooksy, K. Busarow, R. Saykally, et al., Science **249**, 897 (1990).

[168] E. Roueff, P. Felenbok, J. Black, and C. Gry, Astron. Astrophys. **384**, 629 (2002).

[169] G. Galazutdinov, A. Petlewski, F. Musaev, C. Moutou, G. Curto, and J. Krełowski, Astron. Astrophys. **395**, 969 (2002).

[170] M. Ádámkovics, G. Blake, and B. McCall, Astrophys. J. **595**, 235 (2003).

[171] T. Oka, J. Thorburn, B. McCall, S. Friedman, L. Hobbs, P. Sonnentrucker, D. Welty, and D. York, Astrophys. J. **582**, 823 (2003).

[172] M. Schmidt, J. Krełowski, G. Galazutdinov, D. Zhao, M. A. Haddad, H. Linnartz, and W. Ubachs, Submitted (2013).

[173] B. McCall, R. Casaes, M. Ádámkovics, and R. Saykally, Chem. Phys.

Lett. **374**, 583 (2003).

[174] G. Zhang, K. Chen, A. J. Merer, Y. Hsu, W. Chen, S. Shaji, and Y. Liao, J. Chem. Phys. **122**, 244308 (2005).

[175] A. Tanabashi, T. Hirao, T. Amano, and P. Bernath, Astrophys. J. **624**, 1116 (2005).

[176] Y. Sych, P. Bornhauser, G. Knopp, Y. Liu, T. Gerber, R. Marquardt, and P. Radi, J. Chem. Phys. **139**, 154203 (2013).

[177] K. Clusius and A. Douglas, Can. J. Phys. **32**, 319 (1954).

[178] W. Weltner and D. McLeod, J. Chem. Phys. **40**, 1305 (1964).

[179] N. Moazzenahmadi and A. McKellar, J. Chem. Phys. **98**, 7757 (1993).

[180] J. Krieg, V. Lutter, C. Endres, I. Keppeler, P. Jensen, M. Harding, J. Vázquez, S. Schlemmer, T. Giesen, and S. Thorwirth, J. Phys. Chem. A **117**, 3332 (2013).

[181] A. Kramida, Y. Ralchenko, J. Reader, and N. A. Team., NIST Atomic Spectra Database (ver. 5.1) [Online], Available:`http://physics.nist.gov/asd`, National Institute of Standards and Technology, Gaithersburg, MD (2013).

[182] R. Jongma, M. Boogaarts, I. Holleman, and G. Meijer, Rev. Sci. Instrum. **66**, 2821 (1995).

[183] M. A. Haddad, D. Zhao, H. Linnartz, and W. Ubachs, Chin. J. Chem. Phys. **25**, 129 (2012).

[184] A. de Nijs, E. Salumbides, K. Eikema, W. Ubachs, and H. Bethlem, Phys. Rev. A. **84**, 052509 (2011).

[185] H. Lefebvre-Brion and R. W. Field, *The Spectra and Dynamics of Diatomic Molecules* (Elsevier, Amsterdam, 2004).

[186] D. Tokaryk and S. Civiš, J. Chem. Phys. **103**, 3928 (1995).

[187] L. Veseth, Can. J. Phys. **53**, 299 (1975).

[188] J. Hougen, J. Chem. Phys. **36**, 1874 (1962).

[189] M. Izuha and K. Yamanouchi, J. Chem. Phys. **109**, 1998 (1810).

[190] S. Casassus, O. Stahl, and T. Wilson, Astron. Astrophys. **441**, 181 (2005).

[191] C. Savage, A. Apponi, L. Ziurys, and S. Wyckoff, Astrophys. J. **578**, 211 (2002).

[192] O. Stahl, S. Casassus, and T. Wilson, Astron. Astrophys. **477**, 865 (2008).

[193] M. Guélin, S. Green, and P. Thaddeus, Astrophys. J. **224**, L27 (1978).

[194] H. Suzuki, M. Ohishi, N. Kaifu, S. I. Ishikawa, and T. Kasuga, Publ. Astron. Soc. Jpn **38**, 911 (1986).

[195] J. Cernicharo and M. Guélin, Astron. Astrophys. **309**, L27 (1996).

[196] S. Brünken, H. Gupta, C. Gottlieb, M. McCarthy, and P. Thaddeus, Astrophys. J. Lett. **664**, L43 (2007).

[197] J. Cernicharo, M. Guélin, M. Agúndez, K. Kawaguchi, M. McCarthy, and P. Thaddeus, Astron. Astrophys. **467**, L37 (2007).

[198] M. McCarthy, C. Gottlieb, H. Gupta, and P. Thaddeus, Astrophys. J. Lett. **652**, L141 (2006).

[199] K. Kawaguchi, R. Fujimori, S. Aimi, S. Takano, E. Okabayashi, H. Gupta, S. Brunken, C. Gottlieb, M. McCarthy, and P. Thaddeus, Publ. Astron. Soc. Jpn. **59**, L47 (2007).

[200] C. Gottlieb, M. McCarthy, M. Travers, J. Grabow, and P. Thaddeus, J. Chem. Phys. **109**, 5433 (1998).

[201] M. McCarthy, W. Chen, A. Apponi, C. Gottlieb, and P. Thaddeus, Astrophys. J. **520**, 158 (1999).

[202] M. McCarthy, M. Travers, A. Kovacs, C. Gottlieb, and P. Thaddeus, Astrophys. J. Suppl. S. **113**, 105 (1997).

[203] P. Freivogel, J. Fulara, M. Jakobi, D. Forney, and J. Maier, J. Chem. Phys. **103**, 54 (1995).

[204] A. Walsh, D. Zhao, W. Ubachs, and H. Linnartz, J. Phys. Chem. A **117**, 9363 (2013).

[205] H. Linnartz, T. Motylewski, and J. Maier, J. Chem. Phys. **109**, 3819 (1998).

[206] P. Birza, D. Khoroshev, A. Chirokolava, T. Motylewski, and J. P. Maier, Chem. Phys. Lett. **382**, 245 (2003).

[207] T. Motylewski, Thesis, University of Basel (2001).

[208] S. Yeung, M. Chan, N. Wang, and A. Cheung, Chem. Phys. Lett. **557**, 31 (2013).

[209] M. Chan, Chem. Phys. Lett. **390**, 340 (2004).

[210] P. Birza, A. Chirokolava, M. Araki, P. Kolek, and J. Maier, J. Mol. Spectrosc. **229**, 276 (2005).

[211] P. Cias, O. Vaizert, A. Denisov, J. Mes, H. Linnartz, and J. Maier, J. Phys. Chem. A **106**, 9890 (2002).

List of Publications

This following publications are reproduced as chapter in this thesis:

- *Spin-orbit splitting and lifetime broadening in the $\widetilde{A}^2\Delta$ state of l-C_5H.*
  M. A. Haddad, D. Zhao, H. Linnartz and W. Ubachs.
  Chin. J. Chem. Phys. **25**, 129 (2012). **(Chapter 3)**

- *Structure determination of the non-linear hydrocarbon chains C_9H_3 and $C_{11}H_3$ by deuterium labeling.*
  D. Zhao, M. A. Haddad, H. Linnartz and W. Ubachs.
  J. Chem. Phys. **135**, 074201 (2011). **(Chapter 4)**

- *Rotationally resolved $\widetilde{A}^3\Sigma_u^- - \widetilde{X}^3\Sigma_g^-$ electronic transition of HC_7D and DC_7D.*
  M. A. Haddad, D. Zhao, H. Linnartz and W. Ubachs.
  (In preparation). **(Chapter 5)**

- *Rotationally resolved spectra of the 4051 Å comet band of C_3 for all six ^{12}C and ^{13}C isotopologues.*
  M. A. Haddad, D. Zhao, H. Linnartz and W. Ubachs.
  In Press J. Mol. Spectr. (2014); (DOI:10.1016/j.jms.2014.01.010). **(Chapter 6)**

- *The $^2\Pi - \widetilde{X}^2\Pi$ electronic spectra of long carbon-chain $^{(13)}C_{2n}H/D$ molecules for ($n = 4 - 6$).*
  M. A. Haddad, D. Zhao, H. Linnartz and W. Ubachs.
  Submitted (2014). **(Chapter 7)**

The author also contributed to the following publications:

- *C_6H and C_6D: electronic spectra and Renner-Teller analysis*
  D. Zhao, M.A. Haddad, H. Linnartz, W. Ubachs.
  J. Chem. Phys. **135**, 044307 (2011).

- *The 4051 Å comet band of $^{13}C_3$*
  M. A. Haddad, D. Zhao, H. Linnartz and W. Ubachs.
  The Diffuse Interstellar bands, IAU Symposium 297 proceedings (2013).

- *Detection of vibronic bands of C_3 in a translucent cloud towards HD 169454*
  M.R. Schmidt, J. Krelowski, G.A. Galazutdinov, D. Zhao, M.A. Haddad, W. Ubachs, H. Linnartz.
  Submitted (2013).

- *Observation of the $\nu = 8 - \nu = 0$ vibrational overtone in cold trapped HD^+.* J.C.J. Koelemeij, D.W.E. Noom, D. de Jong, M.A. Haddad, W. Ubachs. Appl. Phys. B **107**, 1075 (2012).

Samenvatting

"Cavity Ring-Down spectroscopie van moleculaire koolstofketens"

Optische overgangen in moleculaire koolstofketens worden met verschillende methodes bestudeerd. Veelal worden hoge resolutie spectroscopische studies voorafgegaan door studies waarbij op massa geselecteerde moleculen worden ingevangen in een vaste-stof matrix. Na deze molecuul-specifieke identificatie van de absoprtiebanden kunnen de gasfase spectra in hoge resolutie gemeten worden via een aantal technieken waaronder "cavity ring-down spectroscopie", multifoton ionisatie, lasergeïnduceerde fluorescentie, fotofragmentatie en "photodetachment" spectroscopie. De resulterende gasfase spectra kunnen vergeleken worden met astronomische waarnemingen. Een van de achterliggende doelen van dergelijke studies is om de dragers van de zogenaamde "Diffuse Interstellaire Banden" te identificeren. Een tweede doel van dergelijke hoge resolutie studies is om geometrische en elektronische structuren van koolstofhoudende moleculen te karakteriseren.

In dit proefschrift worden laserspectroscopische studies aan koolstofhoudende moleculen en koolwaterstof moleculen beschreven. Reactieve radicalen van wisselende samenstelling worden geproduceerd in een expanderend plasma. Bij alle metingen wordt de gevoelige detectietechniek van "cavity ring-down spectroscopie" gebruikt. Substitutie met deuterium en koolstof-13 isotopen wordt benut om structuren op te helderen. Systematische spectroscopische metingen bij rotationele temperaturen van slechts enkele Kelvin geven inzicht in de moleculaire constanten van grond en elektronisch aangeslagen toestanden van de moleculen, en daarmee van de moleculaire structuur. Het proefschrift is als volgt opgebouwd:

Na een gedetailleerde beschrijving van een aantal experimentele technieken in Hoofdstuk 2, worden in Hoofdstuk 3 metingen aan de optische spectra van de (0,0) band van het $\widetilde{A}^2\Delta - \widetilde{X}^2\Pi$ elektronische absorptiesysteem van de lineaire C_5H en C_5D radicalen beschreven. Resultaten zijn een bepaling van de spin-baan wisselwerking in de aangeslagen toestand en een bepaling van de korte levensduur (1.6 picoseconde) van dezelfde aangeslagen toestand.

In Hoofdstuk 4 wordt getoond hoe subsitutie met deuteriumisotopen gebruikt kan worden om de geometrische structuur van niet-lineaire koolwaterstofmoleculen te bepalen. Deze methode is toegepast bij metingen aan absorptiespectra van C_9H_3 en $C_{11}H_3$ radicalen. Als resultaat volgt dat de banden horen bij twee moleculen die voldoen aan een $C_{2\nu}$ moleculaire symmetrie en daarom de ruimtelijke structuur hebben die wordt weergegeven met $HC_4(CH)C_4H$ en $HC_4[C(C_2H)]C_4H$.

In hoofdstuk 5 worden gasfase spectra van het $\widetilde{A}^3\Sigma_u^- - \widetilde{X}^3\Sigma_g^-$ absorptiesys-

teem in de HC_7D en DC_7D moleculen; de spectra tonen slechts gedeeltelijk de oplossing van de rotationele structuur, wat identificatie van de lijnen bemoeilijkt. Niettemin konden de moleculaire parameters van grond en aangeslagen toestanden met enige nauwkeurigheid bepaald worden.

In Hoofdstuk 6 wordt het $\widetilde{A}^1\Pi_u - \widetilde{X}^1\Sigma_g^+$ $000-000$ absorptiesysteem van het C_3 molecuul bestudeerd. De blauwe absorptiebanden, ook bekend als de 4051 komeetbanden, zijn reeds vele malen bestudeerd en in de literatuur gerapporteerd. Nieuw is dat alle zes mogelijke varianten met $^{12}C/^{13}C$ isotoopsubstitutie gemeten zijn, en moleculaire constanten voor alle zes zijn bepaald. Specifiek voor het $^{12}C_3$ molecuul is een storing in de aangeslagen toestand bestudeerd.

In hoofdstuk 7 worden voor het eerst de $^2\Pi - \widetilde{X}^2\Pi$ (0,0) vibratieloze banden van een aantal lange koolwaterstofketens met volledige ^{13}C en deuterium isotoopsubstitutie bestudeerd ($^{13}C_8H$, $^{13}C_8D$, $^{13}C_{10}H$ en $^{13}C_{10}D$). Hoewel de bandprofielen niet rotationeel zijn opgelost, wat deels te wijten is aan een te hoge bandbreedte van de laser, zowel als aan de Dopplerbreedte in de plasma-expansie, zijn niettemin waarden bepaald voor de levensduren van de aangeslagen toestanden.

Acknowledgements

I express my sincere thanks to those who have given me support and encouragement during the four years of my PhD. undoubtedly, completing a PhD is a challenging task that one cannot do alone without proper support and guidance of many individuals.

First and foremost, I would like to express my sincere gratitude to my supervisors, Wim Ubachs and Harold Linnartz who gave me the opportunity to begin my PhD study in the Department of Physics and Astronomy at VU University and guided and supported me throughout my work. Besides of many scientific lessons they taught me, I admire their hospitality, humility, personality, philanthropy towards others and there perseverance, and persistence in scientific environments. Although the working under their supervision was demanding, it was always accompanied by a great guidance to find the solutions for difficult problems that I encountered. Wim always provided constant encouragement when it was needed and was always available to answer my questions with great patient. Wim, I am forever indebted you!. Harold, your ability to approach a problem by systematic thinking in order to achieve high-quality work deeply inspired me. I am very pleased and honored to work with you. Thanks for everything!. I hope that we could continue working together in future.

My gratitude to my co-promoter, Dongfeng Zhao who helped me and acted as my daily supervisor. Dongfeng, thanks for all your supports and helps while working on the experimental setup, finding effective and fast solution for technical difficulties, participating in useful scientific discussion and re-writing our papers. Dear Dongfeng, I learned a lot from you. I should also thank Nadine Wehres for the useful discussions about the astronomical aspects of project when I started this work.

Moreover, I would like to be grateful to all members of reading committee for the revision of the manuscript and providing me with important remarks and suggestions.

I would especially like to thank our kind secretory of the department, Marja Herronen who is always very helpful for solving our bureaucracy issues.

My special thanks goes to our LaserLab technicians, Rob Kortekaas and Jacques Bouma who always come up with fast and creative solutions to our technical problems in the lab. Jacques thank you so much for everything. Rob, your effort to maintain well organized lab is admirable. I really appreciate your kindness to help me in solving technical problems that I encountered during my work.

My thanks and good wishes to other members of LaserLab and Department of Physics, both past and present, who maintained the nice working

atmosphere in our group where I had pleasure to work: Adonis Flores, Adrian de Nijs, Aernout van der Poel, Bhargava Ram Gareth Dickenson, Bob Rengelink, Conseng Meng, Daniel Noom, Dmitry Ityaksov, Dominik Kandula, Edcel Salumbides, Florence Ramirez, Hari Prasad Mishra, Hector Alvaro Galue, Itan Barmes, Jeroen Koelemeij, Jonas Morgenweg, Joseph Borbely, Julija Bagdonaite, Jurriaan Biesheuvel, Kjeld S.E. Eikema, Koen van Kruining, Laura Dreisseen, Laura Lipciuc, Madhu Trivikram Talluri, Maria Ofelia Vieitez, Marina Quintero, Mario Dapra, Martijn Stoffels Frank Cozijn, Maurice Janssen, Mingli Niu, Niels Ligterink, Paul Jansen, Remy Notermans, Rick Bethlem, Robert Altmann, Rob van Rooij, Stefan Witte, Steven Knoop, Tjeerd Pinkert, Toncho Ivanov, Wim Vassen, Xavier Bacalla, Ziyu Gu and finally my Iranian colleges, Mohammad M. Rafiee Fanood and Mahsa Vahabi for great coffee breaks and memorial friendly dialogues.

I would also like to thank Hayriye Acer who always tried to keep my office clean.

On behalf my wife and my daughter, I would like to say big thank to my Iranian friends: Abolfazl Avan, Amir Avan, Emad Mir-mohammadi, Freydoon Farkhnia, Hamid-reza Fallah, Hamid Abbasi, Hami Yousefdehi, Hodjat Soleimani-e-Malekan, Houman Ziaee, Jafar Tanha, Mahdi Sargolzaei, Mahmoud Botshekan, Majid Jaghouri, Masoud Mazloum, Mehran Aflakparast, Mohammad-Amin Moradi, Mohammad Jazaeri, Mohammad Mirnejhad, Mohammad Shafahi, Mohammad Hosein Reza-zadeh, Nasser Ayat, Rammin Sarrami Foroushani, Reza Khajoei, Saeed Eslami, Seyed Amin Tabatabei, Seyyed Esmail Mousavi, Zaman Ganji and their family members as well as all who I forgot to mention their names here who live in Amsterdam and other cities of Netherlands. They were a great support for me and my family to forget the far distance from Iran and our family.

I would like to thanks all my teachers, in particular my respected physics teacher at high school, Mr. Jafarzadeh from who learnt me so much and had an important role in motivating me to study physics. I am also thankful to all my teachers at University of Mazandaran and Yazd University in Iran who encouraged me to continue my study towards higher educational level.

I would express my gratitude to Mr. Mohammad-Reza Hariri and the manager of Hariri Science Foundation (Mrs. S. Abbaspour) at Babol (Mazandaran, Iran) to give me a platform to have enjoyable conversations in general physics with elementary and guidance school's students for the first time. It was a valuable lesson for me that *"If you want to learn, try to teach. You know the science when you could explain it with simple words"*.

Without the invaluable support from all members of my family, I would never be able to finish this thesis. I would like to extend my sincerest thanks and appreciation to my mother and father. Many thanks for their prayers for my success and love during these years. They always gave and never asked in return. I am also thankful to my sisters for their kindness and confidence they showed on me which always boost my confidence. I would like to extend my warmest thanks to the new remember of our family, my brother in-law for his

kind words and attentions. I am grateful to my wife's brother and sisters as well as their family members for their helps and encouragements during the last years.

Last but not least, I would like to express my deepest gratitude towards my considerate wife who supported me and helped me overcoming the difficulties without complying. She understood my goals and stayed next to me during the tough periods in last years. I am thankful for all her eternal support, infallible love, patience and dedications and faith in me. I should not forget my daughter, Hana, to thank, who always keep me hoping along the way with her smiles and kisses.

I could not have completed my research without the support of all these wonderful people!